Laser-Driven Ion Acceleration From Carbon Nano-Targets With Ti:Sa Laser Systems

Jianhui Bin

München 2015

Laser-Driven Ion Acceleration From Carbon Nano-Targets With Ti:Sa Laser Systems

Jianhui Bin

Dissertation

angefertigt am

Max-Planck-Institut für Quantenoptik

an der Fakultät für Physik

der Ludwig–Maximilians–Universität München

vorgelegt von

Jianhui Bin

aus Hunan, China

München, den 09.04.2015

Erstgutachter: Prof. Dr. Jörg Schreiber

Zweitgutachter: Prof. Dr. Matt Zepf

Tag der mündlichen Prüfung: 19.06.2015

Zusammenfassung

In den letzten Jahrzehnten hat die Erzeugung von Laserimpulsen mit relativistischen Intensitäten eine hohe Aufmerksamkeit seit auf sich gezogen. Im Jahr 2000 haben bereits mehrere Gruppen von Forschern gezeigt, dass Protonen mit bis zu 58 MeV kinetischer Energie mit geringer transversaler Emittanz in Pikosekunden-Zeitskalen aus Festkörpern mit einigen μm Dicke beschleunigt werden können. Diese einzigartigen Eigenschaften Laser-beschleunigter Ionenstrahlen sind hervorragend für eine Vielzahl neuartiger Anwendungen geeignet. Gleichzeitig kompliziert die große Winkel- und Energiestreuung klassische Anwendungen, die auf konventionellen Beschleunigern beruhen.

Die Verwendung von Nano-Targets als Laser-Ionenquelle bietet eine Reihe von Vorteilen gegenüber μm dicken Folien. Die hier vorgestellte Doktorarbeit hat sich zum Ziel gesetzt Lasergetriebene Ionenbeschleunigung mit Kohlenstoff-Nano-Targets zu demonstrieren und deren Nutzbarkeit für biologische Studien zu evaluieren. Zwei neuartige Nano-Targets werden vorgestellt: Nm dünne Diamantartige Kohlenstoff (DLC) Folien und Schaumtargets aus Kohlenstoff Nanoröhrchen (CNF). Beide wurden im technologischen Labor der Ludwig-Maximilians Universität München hergestellt. Mit DLC Folien konnten hoch kollimierte Ionenstrahlen mit extrem geringer Divergenz von $2°$, eine Größenordnung kleiner im Vergleich zu μm dicken Folien, gezeigt werden. Zweidimensionale Particle in Cell Simulationen deuten auf einen starken Einfluss der Elektronendichteverteilung auf die Divergenz des generierten Protonenstrahls hin. Diese Interpretation wird durch ein analytisches Modell unterstützt. In der gleichen Studie wurden die höchsten Protonen Energien mit moderaten Laserintensitäten von nur $5{\times}10^{18}$ W/cm^2 gemessen. Parallele Messungen von reflektierter und transmittierter Laserenergie wurden erstmalig genutzt, um die absorbierte Energie zu messen. Diese Messungen zeigten eine starke Korrelation von der absorbierten Energie (nicht der Intensität allein) und den höchsten Protonenenergien. Auch diese These wird durch ein analytisches Modell gestützt. Die Ionenenergie konnte des Weiteren durch eine im Vergleich zu μm dicken Folien deutlich geringere Pulsdauer optimiert werden. Dieses Verhalten wird der geringeren transversalen Elektronen Streuung zugeschrieben, die durch die Reduzierung der Target-Dicke von μm auf nm entsteht.

Diese bemerkenswerten vorteilhaften Charakteristiken der Protonenpulse konnten am Advanced Titanium:sapphire LASer (ATLAS) des Max Planck Institutes für Quantenoptik erstmals für die Bestrahlung lebender Zellen verwendet werden. Die Besonderheit dieser Messung bestand in der erzielten Einzellschußdosis von bis zu 7 Gray in einer Protonen-Pulsdauer von einer Nanosekunde.

Für die Weiterentwicklung lasergetriebener Ionenquellen, insbesondere in Hinblick auf höhere Energien, wurden Folgeexperimente am Astra Gemini Laser in England durchgeführt. Zum ersten Mal konnten gezielt relativistische Nichtlinearitäten in μm dicke CNF Targets zum Vorteil der Ionenbeschleunigung ausgenutzt werden. Mit kombinierten CNF-DLC-Targets wurden Kohlenstoff-Ionen durch zirkular polarisierte Laserpulse auf signifikant (3fach) höhere Energien beschleunigt. Die Energieverteilung der Ionen spiegelte dabei den starken Einfluss des Strahlungsdrucks auf die gesamte Beschleunigung wider. Linear polarisierte Laserpulse resultierten in rund 2,4fach höheren Protonenenergien, was sich als Folge der deutlich erhöhten Elektronentemperatur im Target interpretieren lässt. Dreidimensionale PIC Simulationen offenbaren, dass die verbesserte Leistung der Doppelschicht Targets (DLC+CNF) der relativistischen Selbstfokussierung in einem nahkritischen Plasma zugeschrieben werden kann. Interessanterweise kann die Natur der relativistischen Nichtlinearitäten, die die Hauptrolle in der Laser Wakefield Beschleunigung von Elektronen spielt, zur Verbesserung von Laser getriebenen Ionenbeschleunigung angewendet werden.

Abstract

Over the past few decades, the generation of high energetic ion beams by relativistic intense laser pulses has attracted great attentions. Starting from the pioneering endeavors around 2000, several groups have demonstrated muliti-MeV (up to 58 MeV for proton by then) ion beams along with low transverse emittance and ps-scale pulse duration emitted from solid targets. Owing to those superior characteristics, laser driven ion beam is ideally suitable for many applications. However, the laser driven ion beam typically exhibits a large angular spread as well as a broad energy spectrum which for many applications is disadvantageous.

The utilization of nano-targets as ion source provides a number of advantages over μm thick foils. The presented PhD work was intended to investigate laser driven ion acceleration from carbon nano-targets and demonstrate the potential feasibility for biological studies. Two novel nano-targets are employed: nm thin diamond-like-carbon (DLC) foil and carbon nanotubes foam (CNF). Both are self-produced in the technological laboratory at Ludwig-Maximilians-Universität München. Well-collimated proton beams with extremely small divergence (half angle) of 2° are observed from DLC foils, one order of magnitude lower as compared to μm thick targets. Two-dimensional particle-in-cell simulations indicate a strong influence from the electron density distribution on the divergence of protons. This interpretation is supported by an analytical model. In the same studies, the highest maximum proton energy was observed with a moderate laser intensity as low as 5×10^{18}W/cm^2. Parallel measurements of laser transmission and reflection are used to determine laser absorption in the nano-plasma, showing a strong correlation to the maximum proton energy. This observation indicates significance of absorbed laser energy rather than incident laser intensity and is supported by an analytical model. The ion energy also depends on pulse duration, a reduced optimum pulse duration is found as compared to μm thick targets. This behavior is attributed to a reduction of transverse electron spread due to the reduction of thickness from μm to nanometer. These remarkable proton bunch characteristics enabled irradiating living cells with a single shot dose of up to 7 Gray in one nanosecond, utilizing the Advanced Titanium: sapphire LASer (ATLAS)

system at Max-Planck-Institut of Quantum Optics (MPQ). The experiments represent the first feasibility demonstration of a very compact laser driven nanosecond proton source for radiobiological studies by using a table-top laser system and advanced nano-targets.

For the purpose of providing better ion sources for practical application, particularly in terms of energy increase, subsequent experiments were performed with the Astra Gemini laser system in the UK. The experiments demonstrate for the first time that ion acceleration can be enhanced by exploiting relativistic nonlinearities enabled by micrometer-thick CNF targets. When the CNF is attached to a nm-thick DLC foil, a significant increase of maximum carbon energy (up to threefold) is observed with circularly polarized laser pulses. A preferable enhancement of the carbon energy is observed with non-exponential spectral shape, indicating a strong contribution of the radiation pressure to the overall acceleration. In contrast, the linear polarization give rise to a more prominent proton acceleration. Proton energies could be increased by a factor of 2.4, inline with a stronger accelerating potential due to higher electron temperatures. Three-dimensional (3D) particle-in-cell (PIC) simulations reveal that the improved performance of the double-layer targets (CNF+DLC) can be attributed to relativistic self-focusing in near-critical density plasma. Interestingly, the nature of relativistic non-linearities, that plays a major role in laser-wakefield-acceleration of electrons, can also apply to the benefit of laser driven ion acceleration.

Contents

List of Figures

List of Tables

Chapter 1

Introduction

1.1 History and current status of laser driven ion acceleration

Back in the 1970s, soon after the first realization of the laser [1], laser induced inertial confinement fusion (ICF) has been officially proposed by Nuckolls *et al* [2]. One fundamental point in such a scenario is to determine laser energy loss during transportation. For instance, laser energy will be absorbed and turned into hot electrons, which causes preheating of compressed core plasma and thus strongly hinders efficient target compression. Along with hot electrons, fast ions were found to be emitted from the coronal plasma due to charge-separation fields [3, 4], taking a substantial portion of the absorbed laser energy. This for-fusion detrimental development could be considered as the beginning of the history of laser driven ion acceleration. With relatively low laser intensity (below $\sim 10^{15}$W/cm^2) and long pulse duration in the nanosecond or picosecond regime, those fast ions exhibited large emittance angles and broad band spectra with energies of ~100 keV/u.

The invention of chirped pulse amplification (CPA) enables a quantum leap of the laser development from the mid of 1980s [5]. By temporally stretching laser pulse prior to the amplification, the intensity on optical elements is reduced by orders of magnitudes. The laser intensity thus quickly over the barrier of 10^{15}W/cm^2 which has been restricted by the size of laser cross section in the 1970s and 80s, as shown in Fig. 1.1. Multi-terawatt or even multi-petawatt table-top laser systems thus became available, opening up a new era in the studies of relativistic laser-plasma interaction, possibly with extreme intensities exceeding 10^{23}W/cm^2 in future [6]. Here the term 'relativistic' refers to the fact that electrons in the laser field can be accelerated close to the speed of light within

half a laser cycle, corresponding to an intensity threshold of 1.37×10^{18} W/cm^2 for 1 μm laser wavelength [1].
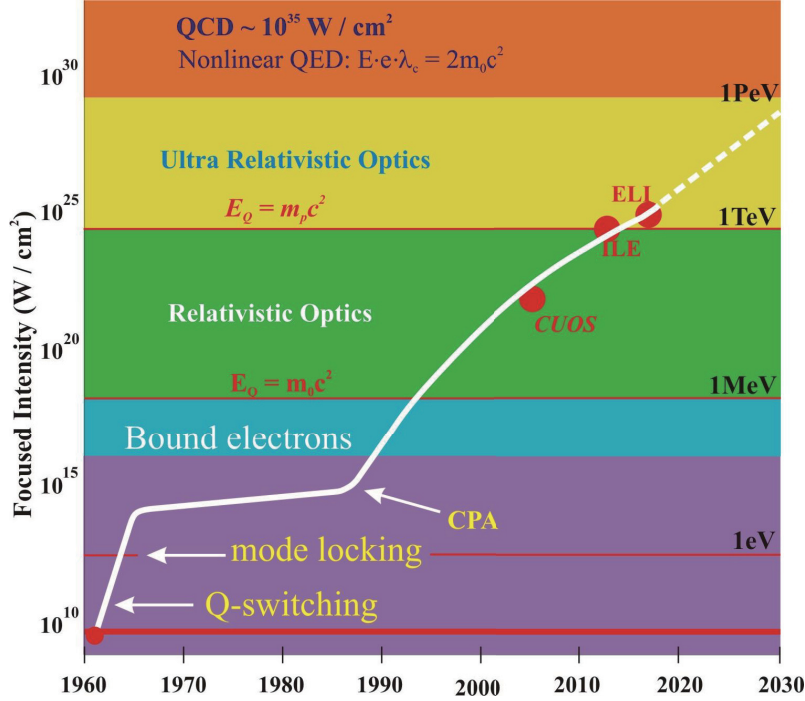
Fig. 1.1 | Laser intensity versus years. Adaption from [7].

The new interaction regime drastically changed the status of laser driven ion acceleration. Although mainly concerning on the energy loss for ICF, in 1994, Fews *et al* demonstrated more than 1 MeV ion emission with a slightly relativistic intense laser system (2×10^{18} W/cm^2) [8]. Later in 2000, significant attentions have been attracted in laser driven ion acceleration by a series of pioneering works [9–12], where highly energetic proton beams up to 58 MeV were observed by irradiating solid-density foils with the first petawatt laser [10]. In addition to higher energy, those proton beams had tremendously different properties as compared to earlier results at lower intensities. These protons are relatively well collimated [13, 14] along the direction normal to the target rear surface [10]. Moreover, the protons are emitted from a transverse region of $\sim 100~\mu m$ on target in a remarkable laminar manner, equivalent to a nearly virtual point source located several 100 μm in front of the target [15, 16]. Not surprisingly, superior characteristic in terms of transverse emittance (<0.004 mm mrad) was observed. The longitudinal acceleration is extremely laminar as well with typical emittance of 10^{-4} eV s owing to ultra short pulse duration induced by the acceleration field ($\sim$ few ps) [17]. These outstanding properties

---

[1]see Sec. 2.2.1 for the derivation of relativistic intensity threshold

make ion beams driven by intense lasers very attractive for many prominent applications (See Sec. 1.2).

Following the pioneering works, numerous experimental investigations have been performed all over the world [18–20]. Thin metal or insulator foil with thickness ranged from a few to hundred μm is one of the most popular targets. Protons have been observed as the most dominant ion species regardless of target material in the experiments, originating from contaminates adhered to target surface [21, 22]. The highest recorded proton energy from such targets has remained unaltered at 58 MeV [10] for almost 10 years and refreshed by 67 MeV recently [23]. The proton beams typically present broad, exponentially decaying spectra with conversion efficiencies below 1 % [24]. Apart from protons, heavy ions can be also accelerated using high intensity lasers [25]. By removing the contaminated protons before the laser irradiation, more efficient heavy ion acceleration has been demonstrated with energies > 10 MeV/nucleon [21, 26]. Similar to protons, those heavy ions exhibit thermal-like spectra. While with special target designs or treatments, quasi-monoenergetic proton [27, 28] or ion beams [29] have been demonstrated with μm thick target.

The determination of the scaling of ion energy is an essential step in order to optimize the ion sources for potential applications [24, 30]. Many investigations have been carried out to achieve such an optimization. One interesting dependence, the scaling of ion energy on target thickness, has been observed among experiments. For μm and sub-μm thick targets, a continued ion energy increase was observed by decreasing the target thickness down to certain optimum value, whereas the optimum thickness strongly relies on the laser contrast in each experiment [24, 31, 32]. With sufficiently high laser contrast, the optimum thickness shifts to nanometer scale [33–37], although the underlying physics changes drastically. Besides the significant enhancement of proton energy, the proton beams gain better collimation as compared to μm thick targets, with a reduced divergence less than 10° [33, 38]. Moreover, those nanometer targets are of great benefit to heavy ions. Large conversion efficiencies of >10 % for carbon ions has been reported [36]. Recently, carbon ions with energies exceeding 1 GeV has been demonstrated from preheated 225 nm diamond target [37], which is one of the biggest values achieved so far although using rather large laser facility (Trident, 80 J, 550 fs). More interestingly, those targets enable quasi-monoenergetic ion beam production without any complicated target configuration [39–42].

Another alternative way to optimize ion acceleration involves targets with lower densities than solid density. Underdense targets can be traced back to the 90s, with the first demonstration of MeV-scale ion beams [43]. Later, the maximum ion energy was founded to scale with plasma density [44], indicating more efficient ion acceleration with higher

plasma density. However, the observed ion beams were emitted with a large divergence, which hampered the use for applications. The collimation problem was quickly overcame, the experimental demonstration of a collimated ion beam from underdense target shows that the key parameter to solve such problem is again the plasma density, higher plasma density is favorable for generating collimated ion beam [45]. Recently, high efficient ion acceleration was reported from a cluster-gas target, ions are accelerated up to ~20 MeV/u with a small divergence of 3.4° from the specific mixture underdense target (of 90 % He and 10 % CO_2) [46].

Near critical density targets, as the intermediate regime between solid density and underdense targets, have attracted great attentions recently. On the one hand, the studies on underdense targets have already shown the advantages for higher plasma density. On the other hand, the researches on the ultrathin nanometer foils will naturally enter the specific regime as in many cases the initial solid density foils will eventually become relativistically transparent during the interaction. Enhanced ion acceleration were reported owing to the existence of near-critical phase [35, 37]. 160 MeV proton beam was demonstrated with near-critical density CH_2 targets, which is the highest value reported so far [47]. Besides, the afore mentioned quasi-monoenergetic ion beams generation from nanometer thin foils are strongly related to near-critical density regime as well. Nevertheless, by virtue of long wavelength CO_2 laser system ($\lambda = 10 \ \mu m$), gas jet can be used as near-critical density targets. Such combination has already shown the advantage of generating high-quality monoenergetic ion beams with high repetition rate [48, 49].

1.2   Applications - some examples

1.2.1   Radiography with proton beams

Laser driven proton beam is a superb alternative to radiography. Owing to the unique characteristics, in particularly spatial beam quality and short pulse duration, radiography with laser driven proton beams has intrinsically very high temporal and spatial resolution. Nearly micrometer spatial resolution and picosecond temporal resolution have been demonstrated by several groups [50–52]. The high resolution thereby allows a precise detection of ultrafast physical phenomena in plasmas. For instance, proton beam has been used as a probing tool to resolve soliton formation [53], shock wave [54], electric field [50, 55, 56], magnetic field structure [57, 58] and Rayleigh-Taylor instability [59]. Besides, this technology can be applied to diagnose dense plasma of ICF interest [60–62], which meanwhile raises higher aspirations on energy and monochromaticity.

1.2.2 Fast ignition by ions

In ICF, the fuel pellet needs to compressed to high densities with a necessary confinement time of a few nanoseconds to drive an implosion. The compression is obtained through two different approaches: direct drive [63, 64] and indirect drive [65, 66]. In the direct drive approach, the outer surface of the pellet is ablated by simultaneously irradiation of high power laser pulses. While in the indirect drive case, the fuel pellet is placed in a hohlraum. The implosion is driven by soft x-ray resulting from interior walls of the hohlraum, therefore substantially relaxes the requirement of the beam uniformity. The biggest laser construction, the National Ignition Facility [67] (NIF), containing 192 synchronized beams with a total energy of 1.8 MJ, is aiming to demonstrate ICF as a future energy source. The experiments in NIF are based on the indirect drive scheme. The latest news from NIF, a fuel gain exceeding unity in the implosion, has been released recently [68]. Note that, the total energy from the laser to the target is still far beyond the output fusion energy.

In the conventional central hot-spot ICF scenario, regarding the different approach of drive, the compression and hot spot ignition are produced by implosion alone, which request a high implosion velocity of 350-400 km/s, namely, a high cost of the driver energy. In contrast, in fast ignition concept [69], the fuel is ignited by a separate pulse after a pre-compression step. This two-step concept will relax the requested implosion velocity and significantly increase the gain. In principle, the ignition can be triggered by either a separate laser pulse or particle pulse such as electron and ion. One advantage for ion ignitor, is that ion deposits most of the energy in a well defined volume, termed as Bragg peak, at the end of the range, which is beneficial for the purpose. Besides, ion is less sensitive to instabilities as compared to electron. Fast ignition with laser driven proton beams [70] and ion beams [71] were therefore proposed, where proton beam with 7-23 MeV [70] and carbon beams with 450 MeV [71] was requested, respectively. While, a high conversion efficiency of ~10 % from the laser to ions is prerequisite for ignition which is still a big challenge for the state-of-the-art of laser driven ion acceleration to date.

1.2.3 Isochoric heating

The study on warm-dense-matter requires uniformly heated plasmas in a single temperature and density. Heating of the material should be extremely rapid and uniform, i.e., isochoric heating. Laser driven ion beams is a unique and powerful tool for that task. Not only because the intrinsic volumetric heating feature of ions, the short pulse dura-

tion of those ion beams meanwhile enables ultrafast heating of the target on a picosecond time scale without noticeable hydrodynamic expansion. The feasibility of this technology has been demonstrated in experiment [72], where the material is heated to a warm dense plasma state with temperature of several eV by an intense proton beam generated from a flat foil. By virtue of a hemispherically shaped target, the material can be further heated to significantly higher temperatures due to the focusing of proton beam. Several groups have applied the technique of proton heating to perform the equation of state (EOS) measurement [73–75], which is of fundamental interest in astrophysics and fusion research. The focusing scheme has been improved as well [76, 77], since it is relevant to many active fields.

1.2.4   Ion beam therapy

One of the most important envisioned applications, also of particularly interest for the scope of this thesis, is ion beam therapy (IBT). The initial concept was proposed in 1946 [78]. As is well known, radiation therapy is aiming to treat cancer with ionizing radiation at the target tumor. In the common x-ray therapy, photons (X-ray or gamma-ray) are used to destroy tumor cells. As shown in Fig. 1.2 (a), those photons slowly lose their energy, with an exponentially decaying curve with increasing thickness. Considerable damages on surrounding healthy cells are almost inevitable in a sense. Using of electrons is one alternative, however, the use is limited by the finite depth of penetration. In contrast, protons and heavier ions deposit major energy in the Bragg peak near the end of the range with zero (proton) or very little dose beyond the Bragg peak (heavier ions), allowing a precise irradiation on a target region with minor toxicity associated with the treatment. The small lateral scatter in the tissue and better depth profile of relative biological effectiveness (RBE) are other advantages for ions [79–81]. Despite many treatment facilities have been established or being built worldwide based on conventional accelerator technology, however, the extremely high global cost of those facilities (e.g. 119 Million Euro for Heidelberg Ion-Beam Therapy Center [82] (HIT)) severely retard widespread application.

A laser-based ion accelerator solution of IBT has been proposed as one attractive alternative [83, 84]. In a purely heuristic picture, the laser is delivered to a target locating in the treatment room [see Fig. 1.2 (b)]. In principle, this attractive all-optical system could rather compact and cost-effective owing to the small acceleration length and the potential minimized size of gantries. The prospect described by the simple picture is enthusiastic but overall optimistic. For example, in order to reaching deep-seated tumors (>25 cm depth of water equivalent), a proton beam with energy of 200 MeV (400 MeV/u
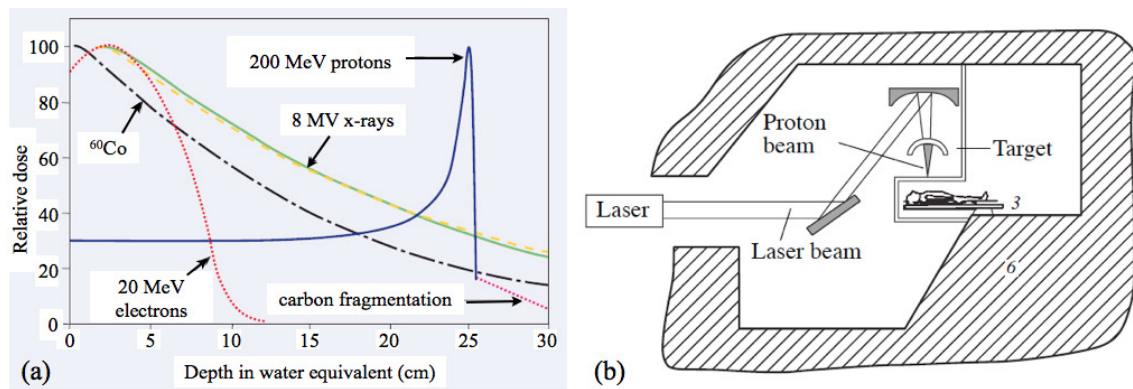
Fig. 1.2 | (a) Dose depth comparison for different radiation type. Adaption from [79]. and (b) Schematic of laser driven IBT. Figure extracted from [83].

for carbon ions) is required. The exact same concern along with few other issues has been raised in the initial proposal [83], which was supposed to reach soon. However, this issue remains unresolved till now and appears to be a complicated facet. Several crucial issues were addressed in [85] as well. More important, it emphasizes the fact that the development of the accelerator-patient-interface is equally important as the understanding of the underlying physics. In the frame of this thesis, a very compact laser-accelerator beam line including necessary components for biological studies is demonstrated (see Chap. 4), providing first benchmark towards the realization of laser-based IBT in future.

1.3 Thesis outline

The presented PhD thesis aims at understanding the fundamental physics of laser driven ion acceleration from nano-targets and their biological studies. One important task for the presented PhD work is the development of a prototype system for laser-based biological investigations. By combining advanced acceleration using nanometer thin targets, a compact nanosecond proton source with a table-top laser system is demonstrated and used for studying the biological effectiveness of ultrashort laser driven ion beams. The underlying physics concerning the laser driven ion source is of essential importance for the scope of this thesis as well. Therefore, the fundamental physics was investigated with different laser systems as the major focus of this thesis, which in turn providing better route towards future applications. The thesis is structured as follows:

chapter 2 introduces the most important theoretical fundamentals relevant to this thesis. Starting with laser field basics, it follows an introduction of single electron dynamics in relativistically intense laser field and laser-plasma interaction and ends with an overview of the main mechanisms of laser driven ion acceleration.

chapter 3 describes the experimental methods. A short introduction of the laser systems utilized in the frame work of this thesis is given. Additionally, the targets and ion diagnostics used in the experiments are discussed.

chapter 4 presents the first experimental demonstration of a truly nanosecond proton source utilizing a table top laser system, enabling irradiating living cells with a single shot dose of up to 7 Gray in one nanosecond. The fast radiobiological processes is studied by measurements of relative biological effectiveness of nanosecond proton bunches in human tumor cells. The experimental setup and the corresponding biological results are presented. The results are published in [86].

chapter 5 reports on experimental studies of divergence of proton beams from nanometer thick diamond-like carbon (DLC) foils irradiated by an intense laser with high contrast. Proton beams with extremely small divergence (half angle) of 2° are observed in addition with a remarkably well-collimated feature over the whole energy range, showing one order of magnitude reduction of the divergence angle in comparison to the results from μm thick targets. This reduction is the key point to the success of radiobiological studies presented in Chap .4. The experimental results are reproduced by 2D particle-in-cell (PIC) simulations. In addition, an analytical model is given to explain the experimental findings. The results are published in [87]

chapter 6 presents experimental results demonstrating that ion acceleration can be significantly enhanced by exploiting relativistic nonlinearties - an achievement that has not been demonstrated so far. This strong non-linearity is obtained by creating a controlled pre-plasma with near-critical density (NCD) and micrometer length using micrometer-thick carbon nanotube foam (CNF). When the CNF is attached to a nm-thick DLC foil, substantial improvement on the properties of ion bunches are observed both with circularly and linearly polarized laser pulses. The experimental results are summarized and the underlying physics is discussed with a aid of 3D PIC simulations.

chapter 7 presents detailed experimental studies investigating ion acceleration from DLC foils. Energetic proton beams with energies up to 6 MeV are observed with moderate laser intensities of about $5 \times 10^{18} W/cm^2$. Parallel measurements of laser transmission and reflection are used to determine laser absorption to the target, presenting a direct correlation between observed maximum proton energy and laser absorption. The dependence of proton energy on pulse duration of incident laser is studied as well, showing an optimum pulse duration much shorter as compared to μm targets. The experimental setup and results are presented. The underlying physics is discussed and supported by an analytical model.

chapter 8 summarizes the experimental results and presents future perspectives.

Chapter 2

Theoretical Backgrounds

To discuss and understand the experimental results presented in this thesis, this chapter is intended to introduce some theoretical fundamentals in laser plasma interaction which are of particular interest to laser driven ion acceleration. More details are be found in existing textbooks, e.g. [88–90].

2.1 Basics of laser field

Generally, Laser light is an electromagnetic wave with high coherence which can be described by Maxwell's equations [91]:

$$
\begin{aligned}
\nabla \cdot \mathbf{E} &= \frac{\rho}{\epsilon_0} \\
\nabla \cdot \mathbf{B} &= 0 \\
\nabla \times \mathbf{E} &= -\frac{\partial \mathbf{B}}{\partial t} \\
\nabla \times \mathbf{B} &= \mu_0(\mathbf{j} + \epsilon_0 \frac{\partial \mathbf{E}}{\partial t})
\end{aligned}
\tag{2.1}
$$

Here, $\mathbf{E}$ and $\mathbf{B}$ is the electric field and magnetic field, respectively. ρ is the charge density, $\mathbf{j}$ denotes the current density, and ϵ_0 and μ_0 represents the permittivity and the permeability of vacuum, respectively. Noted that symbols in bold represent vectors and all the units are given in SI-units in this thesis, unless otherwise indicated. The fields can be expressed by a vector potential $\mathbf{A}$ and a scalar potential Φ:

$$
\begin{aligned}
\mathbf{E} &= -\frac{\partial \mathbf{A}}{\partial t} - \nabla \Phi \\
\mathbf{B} &= \nabla \times \mathbf{A}
\end{aligned}
\tag{2.2}
$$

By applying Lorenz Gauge $\nabla \cdot \mathbf{A} + \frac{1}{c^2}\frac{\partial \Phi}{\partial t} = 0$ to Maxwell's equations will yield the symmetric wave equations:

$$\begin{aligned} \frac{1}{c^2}\frac{\partial^2}{\partial t^2}\mathbf{A} - \triangle \mathbf{A} &= \mu_0 \mathbf{j} \\ \frac{1}{c^2}\frac{\partial^2}{\partial t^2}\Phi - \triangle \Phi &= \frac{\rho}{\epsilon_0} \end{aligned} \tag{2.3}$$

Where $c = \frac{1}{\sqrt{\epsilon_0 \mu_0}}$ is the speed of the light in vacuum.

The simplest plane wave solution for Eq. 2.3 in vacuum can be expressed in a sinusoidal form as:

$$\mathbf{A} = \mathbf{A_0}\sin(\mathbf{k_0} \cdot \mathbf{r} - \omega_0 t + \phi_0) \tag{2.4}$$

where ω_0 is the angular frequency, $\mathbf{k_0}$ is the wave vector with $k_0 = \omega_0/c$, and ϕ_0 is the initial phase. Noted that, this is the linearly polarized solution, any plane wave with elliptical polarization is also a solution of Eq. 2.3.

Using Eq. 2.2, $\mathbf{E}$ and $\mathbf{B}$ are given by

$$\begin{aligned} \mathbf{E} &= \mathbf{E_0}\cos(\mathbf{k_0} \cdot \mathbf{r} - \omega_0 t + \phi_0) \\ \mathbf{B} &= \mathbf{B_0}\cos(\mathbf{k_0} \cdot \mathbf{r} - \omega_0 t + \phi_0) \end{aligned} \tag{2.5}$$

with the relationship between all those amplitudes

$$E_0 = cB_0 = \omega_0 A_0 \tag{2.6}$$

The intensity of the laser light I_0 is defined as the time-averaged magnitude of the Pointing vector $\mathbf{S} = \frac{1}{\mu_0}\mathbf{E} \times \mathbf{B}$ using Eq. 2.5,

$$I_0 = <\mathbf{S}> = \epsilon_0 c E_0^2/2 \tag{2.7}$$

2.2   Laser interaction with a single electron

2.2.1   Definition of relativistic laser intensity

The equation of motion of an electron in an electromagnetic field can be derived from the Lorentz equation

$$\frac{\partial \mathbf{p}}{\partial t} = -e(\mathbf{E} + \mathbf{v} \times \mathbf{B}) \tag{2.8}$$

where $\mathbf{p} = \gamma m_e \mathbf{v}$ is the relativistic momentum of the electron with $\mathbf{v}$ and $\gamma = 1/\sqrt{1 - v^2/c^2}$ is the velocity and the gamma factor of the electron, respectively. There are two forces on the electron, one is governed by the electric field, resulting in a so-called quiver motion in the direction of electric field with the maximum quiver velocity $v_{max,qv} = \frac{eE_0}{m_e \omega_0}$. A second force is given by the second part of the Lorentz force, the $\mathbf{v} \times \mathbf{B}$ component, pointing in the laser propagation direction. Based on Eq. 2.6, we can infer that a ratio of the amplitude of $\mathbf{v} \times \mathbf{B}$ force to the electric force is $v_{max,qv}/c$. Also, this ratio defines the dimensionless vector potential a_0, one important parameter which is frequently used in high intense laser physics instead of the amplitude of the electric or magnetic field, as

$$a_0 = v_{max,qv}/c = \frac{eE_0}{m_e c \omega_0} \tag{2.9}$$

Thus, for $a_0 \ll 1$, namely, the non-relativistic regime, $v_{max,qv} \ll c$, thus the $\mathbf{v} \times \mathbf{B}$ force can be neglected, the electron mostly oscillates in the plane of the electric field. While, in the ultra-relativistic case when $a_0 \gg 1$, the maximum quiver velocity $v_{max,qv}$ approaches c, those two forces become comparable and the electron is pushed in the direction of laser propagation. $a_0 = 1$ defines the relativistic threshold. The corresponding amplitudes of the electric field and magnetic field are given by

$$\begin{aligned} E_0 &= \frac{3.2 \times 10^{12} V/m}{\lambda\,[\mu m]} a_0 \\ B_0 &= \frac{1.07 \times 10^4 T}{\lambda\,[\mu m]} a_0 \end{aligned} \tag{2.10}$$

Combining Eq. 2.7 and Eq. 2.9, the laser intensity can be written in terms of a_0

$$I_0 = \zeta \frac{1.37 \times 10^{18} W/cm^2}{\lambda^2\,[\mu m^2]} a_0^2 \tag{2.11}$$

where λ is the laser wavelength in units of μm, ζ is the corrected coefficient for the polarization with $\zeta = 1$ for linear polarization and $\zeta = 2$ for circular polarization.

In the actual experiment, the peak intensity of the laser pulse can be determined by assuming a perfect Gaussian profile in space and time

$$I_0 = \frac{0.83 E_L}{t_{FWHM} \cdot d_{FWHM}^2} \tag{2.12}$$

Here, E_L, t_{FWHM} and d_{FWHM} denotes the energy, the full-width half-maximum (FWHM) duration and the FWHM focal spot size of the laser pulse, respectively.

2.2.2   Electron dynamics in a plane wave

Now we begin to discuss the single electron dynamics. For the sake of simplicity, all the variables are normalized in the relativistic units in this section as follows: $t \rightarrow \omega_0 t$, $r \rightarrow k_0 r$, $\mathbf{v} \rightarrow \mathbf{v}/c$, $\mathbf{p} \rightarrow \mathbf{p}/mc$, $\mathbf{A} \rightarrow e\mathbf{A}/m_e c^2$ and $E \rightarrow E/m_e c^2$.

Starting from the Lorentz equation Eq. 2.8, the single electron dynamics in a plane wave can be solved exactly [89, 90]. Two equations for the momentum conservation are given:

$$\begin{aligned} \mathbf{p}_\perp - \mathbf{A}_\perp &= c_1 \\ E - p_\parallel &= c_2 \end{aligned}$$

(2.13)

Here the subscript $\perp$ and $\parallel$ denotes the transversal and longitudinal dimensions, the symbol c_1 and c_2 are constants of the motion.

Substituting the electron energy $E = \gamma = \sqrt{1 + (p_\perp)^2 + (p_\parallel)^2}$ into Eq. 2.13, we obtain a general relationship between the transverse and longitudinal momentum

$$p_\parallel = \frac{1 - c_2^2 + p_\perp^2}{2c_2}$$

(2.14)

Assuming the electron is initially at rest in the laboratory frame (i.e., $c_1 = 0$, $c_2 = 1$), then the equations of motion for a plane wave propagating along z direction with $\mathbf{A} = (a_x, a_y, 0)$ read as

$$\begin{aligned} p_x &= a_x \\ p_y &= a_y \\ p_z &= \frac{A^2}{2} \end{aligned}$$

(2.15)

Hence in the presence of a linearly polarized (LP) pulse with $\mathbf{A} = a_0 \cos(\phi)$, and $\phi = x - t + \phi_0$ is the phase. Eq. 2.15 gives the trajectory of an electron

$$\begin{aligned} x(\phi) &= a_0 \sin \phi \\ z(\phi) &= \frac{a_0^2}{4} \left[\phi + \frac{1}{2} \sin(2\phi) \right] \end{aligned}$$

(2.16)

These equations reveal two motions of the electron, as shown in Fig. 2.1 (a), (c) and (d). The transverse motion oscillates at the laser frequency ω_0 with its amplitude linearly scales with a_0. While the longitudinal motion scales with a_0^2 with two components, one

is the oscillation component at double frequency $2\omega_0$ and the other is an additional linear term ϕ, resulting a net drift in the forward direction with average velocity

$$v_d = < \frac{p_x}{\gamma} > = \frac{a_0^2}{4 + a_0^2} \tag{2.17}$$

Clearly, when $a_0 \gg 1$, the electron motion is dominated by the longitudinal component, pointing in the forward direction, consistent with the simple discussion in Sec. 2.2.1.
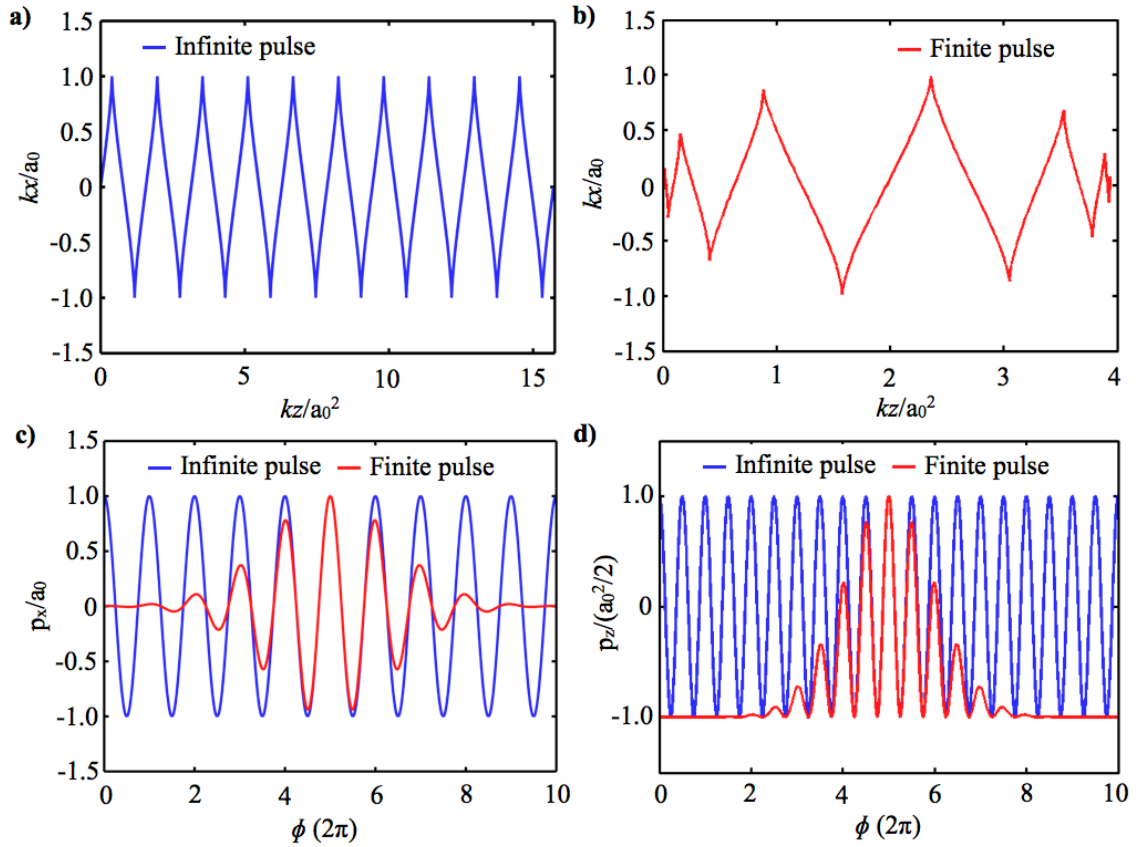
Fig. 2.1 | (a) The trajectory of single electron in an infinite LP plane wave in the laboratory frame with $a_0 = 10$. (b) The trajectory of single electron in a finite LP plane wave with finite pulse duration $a_0(t) = a_0 \exp(-(t-5)/\tau_0)^2$, where $a_0 = 10$, and $\tau_0 = 2$. (c) and (d) show the corresponding transverse and longitudinal momentum, respectively.

Now we consider a more realistic situation, the single electron motion with a pulse with finite duration, as illustrated in Fig. 2.1 as well. Here the temporal envelope is described by a Gaussian profile as $a_0(t) = a_0 \exp(-(t-5)/\tau_0)^2$ with $a_0 = 10$, and $\tau_0 = 2$. As we can see from Fig. 2.1 (c) and (d), the conservation of momentum holds as described by Eq. 2.15 with the slowly varying $a_0(t)$. And the trajectory now can be calculated numerically (see Fig. 2.1 (b)), showing the electron oscillates more longitudinally with the increasing $a_0(t)$.

For circular polarization (CP) with $\mathbf{A} = (\frac{1}{\sqrt{2}}a_0\cos(\phi), \pm\frac{1}{\sqrt{2}}a_0\sin(\phi), 0)$, the electron then can be described by

$$x(\phi) = \frac{1}{\sqrt{2}}a_0\sin\phi$$

$$y(\phi) = \mp\frac{1}{\sqrt{2}}a_0\cos\phi \tag{2.18}$$

$$z(\phi) = \frac{a_0^2}{2}\phi$$
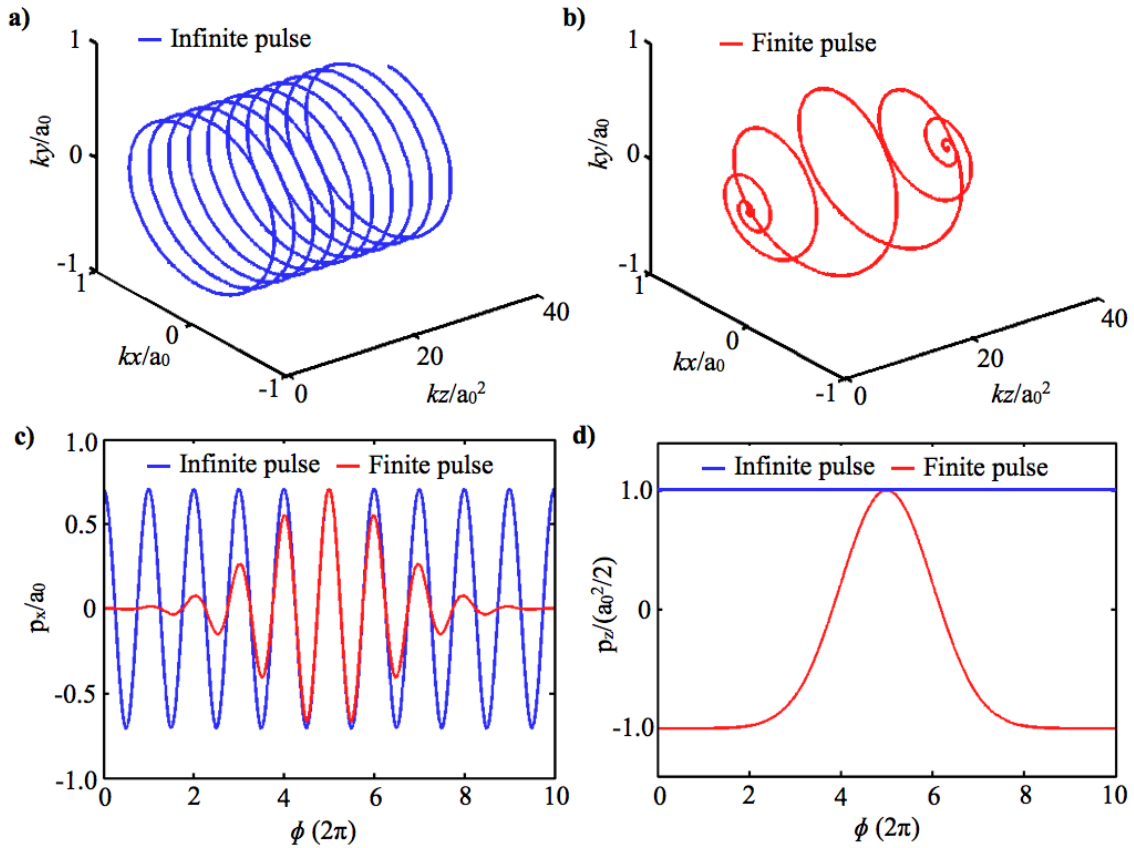
Fig. 2.2 | (a) The trajectory of single electron in an infinite CP plane wave in the laboratory frame with $a_0 = 10$. (b) The trajectory of single electron in a finite CP plane wave with finite pulse duration $a_0(t) = a_0\exp(-(t-5)/\tau_0)^2$, where $a_0 = 10$, and $\tau_0 = 2$. (c) and (d) show the corresponding momentum p_x and p_z, respectively.

In contrary to linear polarization, $2\omega_0$ oscillation component in the longitudinal motion vanishes owing to the identical cancellation from both transverse polarizations. Note that this absence will result in a significant difference in terms of laser absorption and ion acceleration (see Sec. 2.3.3 and Sec. 2.4.2). The electron moves along a helical trajectory with a constant drift velocity v_d (c.f. Eq. 2.17), while for a finite pulse duration, the drift

velocity scales with a_0^2. The comparison of the electron motions in an infinite and a finite pulse can be seen in Fig. 2.2.

As can be seen from Fig. 2.1 and Fig. 2.2, regardless of polarization, the electron will be back in its initial state (Return to rest in our case) after the pulse passed over. There is no net energy transfer from the laser light to the electron, the electron only has a net drift in longitudinal direction. In order to gain energy from the laser, we need to break up the symmetric conditions for the Lawson-Woodward (LW) theorem [92, 93], for example, the introduction of a plasma background or a tight focus beam. In the latter case, we could estimate the emission angle θ out of the laser focus based on previous discussion in this section. Recalling Eq. 2.14, it gives the kinetic energy of electron

$$E_{kin} = \gamma - 1 = p_\parallel = p_\perp^2/2 = a^2/2 \qquad (2.19)$$

This relationship indicates that the kinetic energy of the electron, or in other words, the energy gain, is originally from the transverse electric field, not the $\mathbf{v} \times \mathbf{B}$ force. And it keeps being valid for the tight laser focus as well [89, 90]. Hence one obtains

$$\tan(\theta) = \frac{p_\perp}{p_\parallel} = \sqrt{\frac{2}{\gamma - 1}} \qquad (2.20)$$

2.3 Laser Interaction with a plasma

2.3.1 Basics of plasma

In the actual experiment, the laser is not interacting with single electron but with a pre-formed plasma that being ionized from a solid density target. A plasma is basically an ionized state of a multi-body system that is composed of free charged particles. Typically it has a zero overall charge, however, in certain circumstances, the neutral condition can be violated [1]. Here we introduce few basic concepts of the plasma, which are frequently recalled in the laser-plasma interaction. More details can be found in [88–90].

A feature that identify the plasma from other states is the collisionless (collective) behavior in a relatively macro spatial scale, characterized by the Debye length λ_D, which

---

[1] For a plasma, it requests quasi-neutral rather than completely neutral, namely, being neutral in a spatial scale larger than the Debye length.

is the length over which an individual particle is completely shielded by the surrounding charged particles:

$$\lambda_D = \sqrt{\frac{\epsilon_0 k_B}{e^2} \left[\frac{n_e}{T_e} + \sum_{k=1}^{m} \frac{Zn_i}{T_i} \right]^{-1}} \tag{2.21}$$

Here, k_B is Boltzmann's constant, n_e and T_e denote the electron temperature and density of the plasma, respectively. n_i and T_i are the temperature and density for given ion species, and Z is the corresponding ionized charge of the ions. It is worth to note that due to the high inertia, the ions stays immobile as a background. Their contribution to the Debye length are negligible and the Debye length is thus simplified as

$$\lambda_D = \sqrt{\frac{\epsilon_0 k_B T_e}{e^2 n_e}} \tag{2.22}$$

Beyond the Debye length λ_D, the collective motions take place. While the built-up of such collective motions request certain time scale τ_{pe}. In a very intuitive way it can be estimated as

$$\tau_{pe} = \frac{\lambda_D}{v_{te}} = \sqrt{\frac{\epsilon_0 \gamma m_e}{e^2 n_e}} \tag{2.23}$$

Where $v_{te} = \sqrt{\frac{k_B T_e}{\gamma m_e}}$ is the thermal speed of the electrons. and γ is the time-averaged Lorentz factor in the plasma.

In other word, τ_{pe} is the characteristic response time to a perturbation, such as a laser pulse. τ_{pe} is directly connected to another well known parameter, the electron plasma frequency or Langmuir frequency ω_{pe}

$$\omega_{pe} = \frac{1}{\tau_{pe}} = \sqrt{\frac{e^2 n_e}{\epsilon_0 \gamma m_e}} \tag{2.24}$$

Similarly, the characteristic response time scale τ_{pi} and frequency ω_{pi} for the ions can be defined by $\omega_{pi} = 1/\tau_{pi} = \sqrt{Z^2 e^2 n_i / \epsilon_0 m_i}$. Again, owing to the high mass, we would neglect the influence from the ions. Hence we set $\omega_p \equiv \omega_{pe}$ in the following sections.

A plasma can be completely described by Maxwell's equations (Eq. 2.3) along with the two fluid equations of the electrons and ions that derived from Vlasov equations:

$$\begin{aligned}
(\frac{\partial}{\partial t} + \mathbf{v_j} \frac{\partial}{\partial \mathbf{x}}) n_j &= -n_j \frac{\partial \mathbf{v_j}}{\partial \mathbf{x}} \\
(\frac{\partial}{\partial t} + \mathbf{v_j} \frac{\partial}{\partial \mathbf{x}}) \mathbf{v_j} &= \frac{Ze}{m_j}(\mathbf{E} + \mathbf{v_j} \times \mathbf{B}) - \frac{1}{m_j n_j} \frac{\partial P_j}{\partial \mathbf{x}}
\end{aligned} \tag{2.25}$$

Here, the subscript $j = e, i$ denote the quantities for the electrons and ions, respectively. $\mathbf{v_j}$ is the mean velocity, and P_j is the pressure.

In the laser plasma interaction, three waves are essentially important, two of them are plasma waves, i.e., the electron plasma wave and the ion acoustic wave, and another is an electromagnetic wave, the laser pulse itself. The dispersion relation for electron plasma wave and ion acoustic wave can be derived from Eq. 2.25 as [88]

$$
\begin{aligned}
\omega^2 &= \omega_p^2 + 3k^2 v_{te}^2, \text{ for electron plasma wave} \\
\omega^2 &= k^2 c_s^2, \text{ for ion acoustic wave}
\end{aligned}
\tag{2.26}
$$

where $c_s \simeq \sqrt{Z k_B T_e / m_i}$ is the ion sound velocity.

The dispersion relation of an electromagnetic wave in a collisionless plasma is given by

$$
\omega_0^2 = \omega_p^2 + k_0^2 c^2
\tag{2.27}
$$

Immediately one obtains phase velocity v_p and group velocity v_g from Eq. 2.27 for the laser propagating in the plasma in terms of refraction index $\eta = c k_0 / \omega_0$

$$
\begin{aligned}
v_p &= \frac{\omega_0}{k_0} = \frac{c}{\eta} \\
v_g &= \frac{d\omega_0}{dk_0} = c\eta \\
\text{with } \eta &= \sqrt{1 - \omega_p^2 / \omega_0^2} = \sqrt{1 - n_e / \gamma n_c}
\end{aligned}
\tag{2.28}
$$

This shows that the laser pulse starts to reflect back from a plasma when $\omega_0 = \omega_p$ since the group velocity $v_g = 0$. Such transition point is called the critical density n_c

$$
n_c = \frac{\epsilon_0 \gamma m_e \omega_0^2}{e^2} = \gamma \cdot \frac{1.1 \times 10^{21} cm^{-3}}{\lambda^2 \left[\mu m^2 \right]}
\tag{2.29}
$$

Recalling Eq. 2.15, the Lorentz factor is often used as $\gamma = \gamma_0 = \sqrt{1 + a_0^2 / 2}$ for laser plasma interaction [89, 90] [2].

The critical density n_c separates two distinct regimes for the interactions of laser and plasma. $n_e < n_c$ and $n_e > n_c$ defines the underdense and overdense plasma regimes in which plasma is transparent or opaque, respectively. In case of an overdense plasma, the laser pulse could penetrate evanescently into the plasma beyond the critical surface (where $n_e = n_c$). The characteristic length is identified as the skin depth l_s, over which the mag-

---

[2] $\gamma = \sqrt{1 + (\mathbf{p}/m_e c)^2}$

nitude of the electric field decays to $1/e$ of its initial value. For a step-like, collisionless plasma, the skin depth is given by[3]

$$l_s = \frac{c}{\omega_0 \, \text{Im}(\eta)} = \lambda_0 \left[2\pi \sqrt{\frac{n_e}{\gamma n_c} - 1} \right]^{-1} \tag{2.30}$$

Now we introduce an important concept in laser plasma interactions, the ponderomotive force, which is a force that acts in a plasma or on a single electron due to a non-uniform electric field. The derivation can be carried out in different ways, for example, from single electron dynamics in an electromagnetic wave, or fluid dynamics. Detailed derivation can be found in many text books [88, 90]. The expression of non-relativisic ponderomotive force is given by

$$\mathbf{F_p} = -\frac{e^2}{4m_e\omega_0^2} \nabla \mathbf{E}^2 \tag{2.31}$$

This equation shows that the ponderomotive force is proportional to the gradient of time-averaged electric field, or the laser intensity I_0. Consequently, the electrons will feel such force and drift away from high intensity region (away from the center of the focus). In this process, the electrons will gain energy from laser pulse.

In the relativistic case, the ponderomotive force is obtained by taking the longitudinal motion into account [94]

$$\mathbf{F_p} = -\frac{e^2}{2m_e\bar{\gamma}} \nabla \mathbf{A}^2 = -m_e c^2 \nabla \gamma \tag{2.32}$$

2.3.2 Pulse shaping effects

The refractive index η is a very interesting parameter in the relativistic laser plasma interactions. From Eq. 2.28 one can see that any variation in plasma density or in laser intensity will lead to a modification in the refractive index η. Such modification gives rise to a number of nonlinear effects. In this section, we intend to introduce three interesting nonlinear effects which are closely connected to the refractive index η, i.e., self focusing, relativistic self-phase-modulation, and relativistic induced transparency. In turn, those nonlinearities have the potential to be used to shape the relativistic laser pulses.

---

[3]Noted that for a high density plasma, the skin depth is expressed approximately in a more simple form as $l_s = c/\omega_0$.

Self-focusing

Self-focusing effect is caused by the spatial variation of the refractive index η. Two mechanisms are responsible for that. One is known as ponderomotive self-focusing, resulting from the expulsion of the electrons by the ponderomotive force. As stated, the ponderomotive force will expel electrons from high intensity regimes, resulting a transverse density gradient with lower electron density in the center of laser focus. According to Eq. 2.28, the refractive index η is larger in the center. Hence the plasma acts as a positive lens, leading to self-focusing of the laser pulses to higher intensities. Analogously, the electron oscillating in the laser field and the instantaneous relativistic mass correction $\gamma = \sqrt{1 + a^2/2}$ depends on the laser intensity. The spatial distribution of the laser intensity thus leads to a transverse variation of the refractive index η and cause self-focusing. Such phenomena is referred to as relativistic self-focusing, as demonstrated in three-dimensional particle-in-cell (3D PIC) simulations [95]. Noted that the self-focusing increases gradually during the propagation owing to the resultant increased laser intensity.

Assuming a laser pulse with Gaussian radial intensity profile $a(r) = a_0 \exp(-2 \ln 2 \cdot r^2/D_L^2)$ interacting with a plasma. Here, λ is the wavelength and D_L is the FWHM diameter of the laser. According to Eq. 2.28, the refractive index for relativistic self-focusing is given by

$$\eta = \sqrt{1 - \frac{n_e}{n_c \sqrt{1 + a^2/2}}} \tag{2.33}$$

and the phase velocity v_p is determined by:

$$v_p = \frac{c}{\eta} \simeq c \left[1 + n_e/2n_c a(r)\right], \text{ for } a(0) \gg 1 \tag{2.34}$$

The maximum difference of velocity $\triangle v_p$ through the area of $\sqrt{2}D_L$ (the FWHM diameter of $a(r)$) is $\triangle v_p = cn_e/2n_c a_0$. Thus the divergence angle of the laser beam is given by:

$$\theta = \sqrt{\frac{\triangle v_p}{c}} = \sqrt{\frac{n_e}{2n_c a_0}} \tag{2.35}$$

With this, the self-focused spot FWHM diameter D_{FWHM} and self-focusing length f can be estimated by applying Gaussian beam propagation as

$$D_{FWHM} = \frac{2\sqrt{\ln 2}\lambda}{\pi\theta} \approx 0.74\lambda\sqrt{\frac{n_c a_0}{n_e}}$$
$$f = \frac{\sqrt{2}D_L}{2\theta} \approx D_L\sqrt{\frac{n_c a_0}{n_e}} \tag{2.36}$$

Although the derivation is far from rigorous, the rough estimation reveals the same scaling for the focal spot size in previous publications except for some small deviation in pre-factors [96, 97].

The derivation above is valid for relativistic laser pulse, while in non-relativistic case when $a_0 \ll 1$, we should rewrite Eq. 2.34 as

$$v_p = \frac{c}{\eta} \simeq c\left[1 + n_e/2n_c(1 - \frac{a(r)^2}{4})\right], \text{ for } a(0) \ll 1 \tag{2.37}$$

The divergence angle is thus given by

$$\theta = a_0\sqrt{\frac{n_e}{8n_c}} \tag{2.38}$$

This gives the well known expression of the threshold power for self-focusing, detailed derivation can be found in [90]

$$P_c = 17.5\frac{\omega_0^2}{\omega_p^2} \, [GW] \tag{2.39}$$

Relativistic self-phase-modulation

Similar to self-focusing, the variation of the refractive index give rises to relativistic self-phase-modulation (SPM). Whereas, SPM is nearly a one-dimensional (1D) problem. When a laser pulse propagating through a plasma, it induces a varying refractive index in longitudinal dimension (time-dependent) owing to the time-varying laser intensity. This time-dependent refractive index causes a phase shift of the pulse, resulting in a broadening of the frequency spectrum, i.e., the self-phase-modulation. At the pulse front, the intensity rises and causes an increasing refractive index η, this time-dependent refractive index causes a frequency red shift. While the pulse back is blue-shifted due to the decreasing refractive index. Since the group velocity v_g at the pulse back is faster than the pulse front (based on Eq. 2.28), it leads to a compression (steepening) of the laser pulse. And the compression becomes essentially asymmetric and exhibit a positive chirp, as demonstrated in the theoretic work [98]. The pulse compression has been observed in

the experiment [99]. And the asymmetric compression has been verified experimentally [100], showing pulse steepening at pulse front or the back respectively.

Relativistically induced transparency

As discussed in Sec .2.3.1, for the overdense plasma, the laser pulse can only penetrate evanescently into the target characterized by the skin depth l_s. While according to the dispersion relation Eq. 2.27, the mass of the electrons has to be corrected by the Lorentz factor γ owing to the relativistic motion of the electrons. As γ increases and simultaneously the plasma density reduces owing to the expansion during the interaction, the plasma eventually becomes transparent at a critical point

$$\frac{n_e}{\gamma n_c} \leqslant 1 \tag{2.40}$$

Thereafter the initially opaque plasma suddenly acts as a transparent medium. This phenomenon is called relativistically induced transparency. In particular, the transition from opaque to transparent happens in a picosecond timescale, making it ideally suitable for ultrafast optical shutters. The dynamics of relativistically induced transparency has been investigated in experiments recently [101].

2.3.3 Laser absorption in plasmas

For laser driven ion acceleration, one should be aware that the laser can not directly accelerate ions with current available laser intensities. Substituting the proton mass into Eq. 2.9, we can rewrite the laser intensity as

$$I_0 = \zeta \frac{4.62 \times 10^{24} W/cm^2}{\lambda^2 \left[\mu m^2\right]} a_0^2 \tag{2.41}$$

Hence, even for proton to directly gain relativistic energy from the laser field, it requires an intensity far exceeding the laser intensities today ($I_0 \sim 10^{18} - 10^{22} W/cm^2$). Instead, the laser energy is intermediately transferred to the electrons. The electrons are pushed forward and a high electrostatic field comparable to the laser field is thus built up due to charge separation. In turn, the electrostatic field acts on the ions and is responsible for ion acceleration. Thus, laser absorption by electrons is of particular interest for ion acceleration and will eventually determine the efficiency of ion acceleration. In this section we will briefly introduce few important absorption mechanisms, a more comprehensive introduction can be found in [102].

Inverse bremsstrahlung

Inverse bremsstrahlung is one of the most common absorption mechanism happened at low laser intensity ($I_0 \leqslant 10^{15} W/cm^2$). It involves two sequential processes. Initially, electrons oscillate in the presence of a laser field (see Sec .2.2.2). Then, the oscillation energy is converted into plasma by collisions of electrons with ions, resulting in effective heating of the plasma. As it is the opposite process of bremsstrahlung, this phenomenon is named as inverse bremsstrahlung. The absorption depends on the electron-ion collision frequency ν_{ei} [88]

$$\nu_{ei} \propto \frac{n_e Z}{T_e^{3/2}} \tag{2.42}$$

Clearly, the absorption is large for high densities, high Z plasmas and low electron temperatures. At higher laser intensities, as the electron temperatures increase accordingly, inverse bremsstrahlung becomes less efficient. The heating process will be dominated by collisionless absorption mechanisms as introduced in the following.

Resonance absorption

As mentioned in Sec .2.3.1, a laser pulse will be reflected back from the critical surface when $n_e = n_c$. Considering an obliquely incident laser pulse at an angle θ between wave number k and plasma density gradient ∇n_e, the laser pulse reflects at lower electron density n_e depending on the incidence angle

$$n_e = n_c \cos^2 \theta \tag{2.43}$$

Some partial field can tunnel beyond it and reach the critical density region. In this case, if the electric field $\mathbf{E}$ of the laser pulse has some component in the direct of the plasma density gradient ∇n_e ($\mathbf{E} \cdot \nabla n_e \neq 0$), typically referred to p-polarized laser, it oscillates electrons along ∇n_e and generates density fluctuations which can be resonantly enhanced by the plasma at the plasma frequency ω_p. An electron plasma wave will be excited at the tunneling point and the laser energy is damped into the plasma wave via collision at low intensities or collisionless effects at high intensities. This phenomenon is termed resonance absorption, and the fractional absorption rate f_{ra} is given by [88]

$$f_{ra} \approx \frac{\phi^2(\tau)}{2} \tag{2.44}$$

where $\phi(\tau) \approx 2.3\tau \exp(-2\tau^3/3)$ is the characteristic resonance function and the variable $\tau = (\omega_0 L/c)^{1/3} \sin \theta$ is depending on the plasma density scale length L and incidence angle

θ. It is worth to mention that a rippling of the critical surface due to two or three dimensional effects [103] can cause resonance absorption even with s-polarized laser pulse.

Vacuum heating

In case of a steep plasma density gradient ($L \ll \lambda$), the classical resonance absorption ceases to work since no resonance. In fact, the laser energy can be converted into plasma via a 'Not-so-resonant, resonant absorption' mechanism, known as vacuum heating or Brunel heating [104]. The laser field can directly act on the electrons near the sharp plasma-vacuum interface now. If $\mathbf{E} \cdot \nabla n_e \neq 0$ (termed an obliquely incident p-polarized laser), the electrons can be pulled out into vacuum by the electric field of the laser and pushed back into plasma when the laser field reverses its direction, i.e., at frequency ω_0. The laser field can only penetrate evanescently into the overdense plasma up to a skin depth l_s (see Eq. 2.30), while the electrons can penetrate further beyond l_s and eventually transfer the absorbed energy from the laser pulse to plasma via collisions. The fractional absorption rate f_{vh} can be estimated based on a very simple analytical model as [90]

$$f_{vh} = \frac{4}{\pi} \frac{\sin^3 \theta}{\cos \theta} a_0 \tag{2.45}$$

Thus the absorption increases with higher laser intensity and larger incidence angle. For a more rigorous derivation, some necessary corrections, e.g. the corrections resulting from imperfect reflection and relativistic motion of the electrons, need to be taken into account [90, 104].

j × B heating

This absorption mechanism arises from the oscillating component of the $\mathbf{v} \times \mathbf{B}$ term of the Lorentz force. As shown in Sec .2.2.2, the electron motion will be dominated by the $\mathbf{v} \times \mathbf{B}$ component of the Lorentz force for relativistic laser intensities ($a_0 \gg 1$), which will cause a longitudinal oscillation at frequency $2\omega_0$ for linearly polarized laser pulses. Analogous with the vacuum heating mechanism, this $\mathbf{j} \times \mathbf{B}$ force can accelerate electron into plasma for a steep plasma density gradient and result in heating [105]. Obvious, this $\mathbf{j} \times \mathbf{B}$ force performs best at normal incidence and gain significance at relativistic intensities. Numerical simulations have shown that this absorption increases with increasing

laser intensity I_0 and decreases with increasing plasma density n_e [88, 106, 107], leading to a hot electron temperature scaling as [106]

$$T_h = (\gamma - 1)m_e c^2 \approx (\sqrt{1 + \frac{I_0 \lambda^2 \left[\mu m^2\right]}{2 \times 1.37 \times 10^{18} W/cm^2}} - 1)0.511 MeV \qquad (2.46)$$

This form is the standard expression of the transverse ponderomotive potential which is understandable since the energy gain of electrons initially result from the transverse electric field (see Eq. 2.19). In fact, this scaling has been verified experimentally [108].

Finally, It is important to point out that this mechanism works for any polarizations except for circular polarization where the oscillation component of the $\mathbf{j} \times \mathbf{B}$ term vanishes (c.f. Sec. 2.2.2).

2.4 Laser driven ion acceleration

As discussed above, direct ion acceleration by laser field is not possible with current laser intensities. Almost all the ion acceleration mechanism investigated so far are resulted from the charge separation between fast electrons and ions. Depending on the laser and target parameters, many different mechanisms have been proposed, including coulomb explosion (CE) [43], collisionless shock acceleration (CSA)[109–111], acceleration in a dipole vortex [112, 113], breakout afterburner (BOA) [114–117] and many other mechanisms. A more comprehensive introduction are referred to the existing review papers [18–20]. In this section, we will present acceleration mechanisms most relevant to the works of this thesis in the following.

2.4.1 Target normal sheath acceleration

Target normal sheath acceleration (TNSA) mechanism was firstly introduced [118, 119] to interpret the experimental observation of MeV-level ion beams [9–12], which is later found to be the most dominant acceleration mechanism in most of the experiments therefore attracts enormous attentions. As shown in Fig. 2.3 (a), in a simple physical picture of TNSA mechanism, a relativistic laser pulse incident on a μm thick solid-density target. The front surface of the target feels the prepulse of the laser and expands spherically. As the target remains opaque during the interaction, the laser pulse only interacts with the front side of the target and generates lots of hot electrons via different absorption mechanisms (see Sec. 2.3.3). Those hot electrons penetrate through the target, a portion of

them (the electron cloud) can escape the target to the rear side vacuum, forming an electrostatic field owing to charge separation which can ionize the rear surface of the target and accelerate ions to high energy.
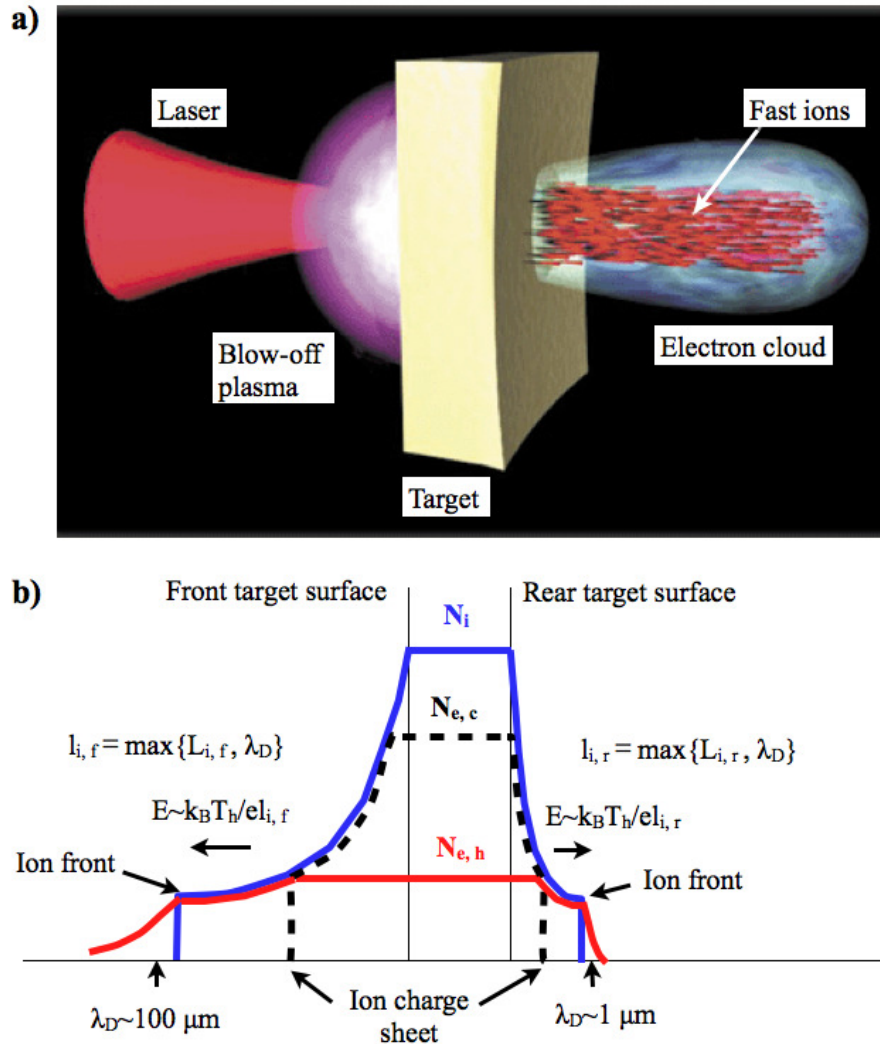
Fig. 2.3 | (a) Schematic of TNSA mechanism. Adaption from [120]. (b) Schematic representative of the TNSA Model, showing 1D ion (blue), cold electron (black), hot electron (red) density distributions. Note that the prepulse of the laser ionizes the front surface of the target and forms a plasma with the Debye length of the order of $100\,\mu m$. While at the rear side, the target has a sharp density gradient with the Debye length of few μm. Adaption from [118].

This simple TNSA picture can explain most of the experimental observations. Owing to the low ionization potential and large charge-to-mass ratio, protons response to the electrostatic field firstly and gain most effective acceleration, thereafter screening the accelerating field for other ion species. This explains why mainly the protons have been observed experimentally [9–12]. The presence of the protons is attributed to hydrocarbon or water contaminants adhered to the target which has been verified experimentally

[21, 22]. Since the electrostatic field is strongly dependent on the spatial distribution of the hot electrons that escapes from the target, leading to an acceleration normal to the target surface. This is consistent with experiment [10], thereby referred to as target normal sheath acceleration. Also, the spatial distribution of hot electrons is responsible for the observed small divergence angle of ion beams [13, 14]. A relatively flat rear surface gives rise to the collimation of ion beams in forward direction from the target rear and the local curvature of the rear surface results in an decreasing divergence with increasing ion energy. In fact, the electrostatic field has a 3D distribution initially depending on the spatial distribution of hot electrons and later modulated by expansion of the surface during the interaction, leading to the observed dependence of divergence on ion energy.

The TNSA model also explains the different characteristics between the ion beams observed at target front (backward) and target rear (forward) [118]. The accelerating field E_{acc} via TNSA is given by

$$E_{acc} = \frac{k_B T_h}{e l_{i,k}} \tag{2.47}$$

where $l_{i,k}$ is the maximum value between the scale length of ions density $L_{i,k}$ and the Debye length λ_D. The subscript $k = f, r$ denote quantities for front and rear side, respectively. Fig. 2.3 (b) shows the 1D density distributions for different particles for both sides of target. Obviously, owing to the steep gradient at target rear, E_{acc} is significantly higher as compared to the one at target front. Typically, ion beams at the rear side are accelerated to much higher energies than at the front. Moreover, the large spherical blow off plasma at the target front gives rise to a 2π ion emission in contrast to the forward ion beams from the target rear. In fact, the above discussion can be extended further to explain the characteristics of ion beams with low laser intensities back to the old days [3, 4].

TNSA mechanism can be described by the freely expanding plasma model [121–125]. Assuming the density of electrons follows Boltzmann distribution with $n_e = n_{e0} \exp(e\Phi/k_B T_e)$ with the electron density $n_{e0} = Z n_{i0}$ in unperturbed plasma and the electrons are in isothermal equilibrium, along with Eq. 2.25 to describe the ion motion, one obtains the basic self-similar solution based on the quasi-neutrality condition (i.e., $n_e = Z n_i$) as

$$\begin{aligned} n_e &= Z n_i = n_{e0} \exp(-x/c_s t - 1) \\ v_i &= c_s + x/t \\ E_{acc} &= k_B T_e / e c_s t \end{aligned} \tag{2.48}$$

where v_i is the ion velocity and $c_s = \sqrt{Z k_B T_e / m_i}$ is the ion sound velocity. Note that the accelerating field given by Eq. 2.47 is reproduced for a density scale length $c_s t = L_i$.

This simple solution shows few important aspects. First, the accelerating field E scales with the electron temperature and decreases with time or with the scale length. Second, the energy increases with time while the number of ions decays exponentially with time. Although it predicts an infinite acceleration which is physically impossible, this dilemma can be resolved with more realistic consideration, for example, taking the inertia of electron and electron cooling into account. Roughly speaking, the acceleration terminates when the scale length L_i equals the Debye length λ_D, which gives a maximum ion velocity as [121, 125]

$$v_{max} = 2c_s \ln(\omega_{pi}t) \tag{2.49}$$

where $\omega_{pi} = \sqrt{Z^2e^2n_i/\epsilon_0 m_i}$ is the ion plasma frequency.

A more precise solution concerning the structure of ion front predicts an exponential ion spectra with a high energy cutoff E_{max} which is typically observed in experiments [126]

$$E_{max} = 2Zk_BT_h\{\ln(\tau + \sqrt{\tau^2 + 1})\}^2 \tag{2.50}$$

Here $\tau = \omega_{pi}t/\sqrt{2e_N}$ and $e_N = 2.71828...$ is the numerical constant. In fact, the electron temperature T_h is found to approximate to the pondermotive potential in the experiments, namely, it scales with the square root of $I_0\lambda^2$ (see Eq. 2.46). and the acceleration time is given by $\tau = 1.3\tau_L$, where τ_L is the laser duration in a rather crude approximation [24]. More complicated solution for the freely expanding plasma model concerning two-temperature electron distribution and electron cooling can be found in [127–129].

In another point of view, TNSA mechanism can be described in terms of laser absorption by electrons f [130]. The major advantage of this model is that the complicated process regarding electron heating in laser-plasma interaction is avoided, which strongly simplify the discussion. By considering the transverse spread of the electrons during the propagating through the target as

$$B = r_L + d \cdot \tan\theta \tag{2.51}$$

where B represent the radius of the electrons bunch at the rear surface given by the radius of the laser r_L, the target thickness d and θ the half angle of the electrons propagating through the target, thus the maximum possible ion energy for an infinitely long acceleration $E_{i,\infty}$ is characterized in terms of f as

$$E_{i,\infty} = 2Zm_ec^2(fP_L/P_R)^{1/2} \tag{2.52}$$

where P_L is the laser power and $P_R = m_e^2 c^5/e^2 = 8.71 GW$ is the relativistic power unit. Importantly, it shows $E_{i,\infty}$ depends on the square root of the absorbed laser energy only but no direct dependence on the incident laser intensity I_0 as compared to the freely expanding plasma model (cf. Eq. 2.50).

Considering the finite accelerating time, the maximum ion energy E_{max} is given by [130]

$$\frac{\tau_L}{\tau_0} = X \left\{ 1 + \frac{1}{2} \frac{1}{1 - X^2} \right\} + \frac{1}{4} \ln \frac{1 + X}{1 - X} \tag{2.53}$$

Here, $\tau_0 = B/v(\infty)$ with $v(\infty) = \sqrt{2E_{i,\infty}/m_i}$ stands for the accelerating time and $X = (E_{max}/E_{i,\infty})^{1/2}$. Again, the equation shows no explicit dependence on I_0.

2.4.2 Radiation pressure acceleration

Radiation pressure originates from the momentum transfer from the electromagnetic (EM) wave to a surface via either reflecting or absorption. For a plane EM wave, it can be expressed as [20]

$$P_{rad} = (1 + R - T)\frac{I_0}{c} = (2R + A)\frac{I_0}{c} \tag{2.54}$$

where R, T and A denotes the reflection, transmission and absorption coefficients, respectively.

When the laser intensity is sufficiently high, the radiation pressure of the laser pulse can lead to another important acceleration mechanism, named radiation pressure acceleration (RPA) mechanism [131–145]. It has been already proposed in a theoretical study in 2004 [131]. In such scenario, all the electrons inside the target can be pushed forward with the velocity close to the speed of light by the radiation pressure while the ions keep immobile, leading to a strong electrostatic field set up by the charge separation. Such electrostatic field is strong enough to accelerate the ions to relativistic energies within one laser cycle when the laser intensity is extremely high ($I_0 > 1.2 \times 10^{23} W/cm^2$). The target is comoving with the laser pulse as a whole, as in a light sail picture. Thus most of the laser energy is transferred to the ions due to the high mass, leading to highly efficient ion acceleration. Also, the ion spectrum presents a monoenergetic feature instead of the exponential spectra obtained via TNSA (see Sec. 2.4.1). Note that this senario has much in common with the idea of interstellar vehicle driven by the laser light [146]. And all the other definitions such as laser piston acceleration (LPA) [131], sweeping acceleration (SA) [132], phase-stable acceleration (PSA) [135], and light sail (LS) acceleration [139, 140] are literally one individual name for the RPA mechanism.

It has been quickly realized that the requested high laser intensity ($I_0 > 1.2 \times 10^{23} W/cm^2$) for RPA [131] could be substantially released by using circularly polarized laser pulse [133]. As discussed in Sec. 2.2.2 and Sec. 2.3.3, the oscillation component of the $\mathbf{j} \times \mathbf{B}$ force vanishes, resulting in a strong suppression on the electron heating in case of circular polarization. Naturally, the ion acceleration via TNSA is inhibited and RPA could dominate the acceleration process at much lower laser intensities.

At an early stage, the electrons are steadily pushed inward to an equilibrium position where the radiation pressure of the laser balances the charge-separation electrostatic field, forming a compressed electron layer in front of the laser and a depletion layer left behind, as shown in Fig. 2.4 (a). Assuming the electrostatic field E_x has linear profiles both in the depletion layer ($E_x = E_0 x/d$ for for $0 < x < d$) and the compression layer ($E_x = E_0 [1 - (x - d)/l_s]$ for $d < x < d + l_s$), the balance condition then reads as

$$E_0 n_0 (d + l_s)/2 = (1 + R - T)\frac{I_0}{c} \tag{2.55}$$

Combining the Poisson equation as $E_0 = en_{p0}l_s/\epsilon_0$ and the equation of charge conservation $n_0(d + l_s) = n_{p0}l_s$, we rewrite Eq. 2.55 as

$$\frac{\epsilon_0 E_0^2}{2} = \frac{(1 + R - T)I_0}{c} \tag{2.56}$$

and the thickness of the depletion layer can be derived with the approximation $n_0 d \approx n_{p0}l_s$ as

$$d = \sqrt{\frac{2((1 + R - T)I_0\epsilon_0}{cn_0^2 e^2}} = \sqrt{\frac{(1 + R - T)\zeta}{4\pi^2}}\frac{n_c}{n_0}a_0\lambda \tag{2.57}$$

where ζ is again the corrected coefficient for the polarization with $\zeta = 1$ for linear polarization and $\zeta = 2$ for circular polarization. Clearly, d defines the threshold target thickness that the balance condition still hold. Typically, thinner targets than d causes less efficient ion acceleration. To some extend this issue can be compensate with multi species of ions inside the target, which could result in higher energetic light ion beam [144]. Nevertheless, the uneven situation can also lead to the generation of very dense monoenergetic electron bunch which can be used as a relativistic flying mirror for coherent X-ray generation [147]. Note that, in case of $R = 100\%$ with circular polarization, Eq. 2.57 gives the same expression $d = (a_0\lambda/\pi)(n_c/n_0)$ as [135].

Depending on the location, the ions have two distinct behaviors. The ions in the depletion layer will never catch up these ions in the compression layer due to the linearly increasing electrostatic field. The ion density decreases during the time, forming a shelf

density region. In contrast, for the ions locate in the compression layer, they will reach the ending point of the compression layer ($x = d + l_s$) at the same time owing to the linearly decreasing electrostatic field with a maximum velocity v_{max}. Ideally, the density goes infinite. This process is essentially the same process when a laser pulse pushes the plasma forward by the radiation pressure and reflects ions from the plasma surface up to twice the recession velocity, the so-called hole boring (HB) acceleration process. In such process, all the ions regardless of the species have quasi-stationary velocity as [106, 133]

$$\frac{v_{max,HB}}{c} = 2\frac{v_{HB}}{c} = 2\sqrt{\frac{(1 + R - T)\zeta}{2}\frac{m_e}{m_i}\frac{Zn_c}{n_e}}a_0 \qquad (2.58)$$
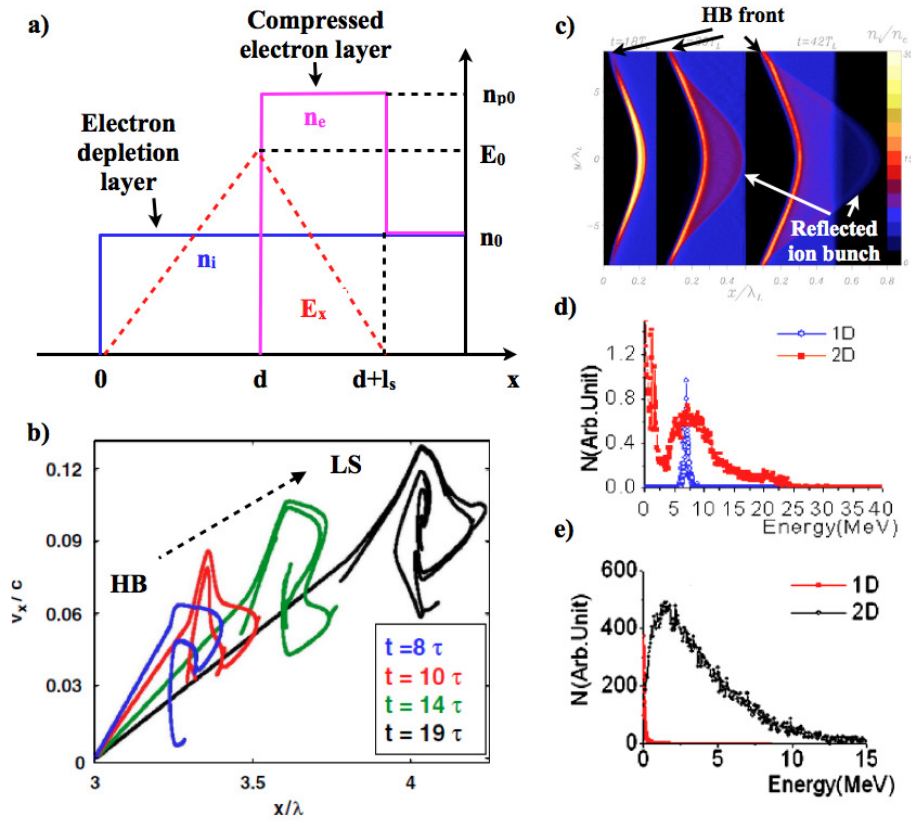
Fig. 2.4 | (a) Schematic of density profiles for ion density (blue line), electron density (magenta line), and the resultant electric field due to charge separation (red dashed line) at the equilibrium position when the radiation pressure of the laser balances the electrostatic pressures. Here d is the thickness of the depletion layer and the thickness of the compression layer is characterized by the plasma skin depth l_s (c.f. Eq. 2.30). and n_0 denotes the initial electron density. Adaption from [133]. (b) An example of ion phase space evolution from 1D particle-in-cell (PIC) simulations, here τ presents one laser cycle. Figure extracted from [134]. (c) Snapshots of ion density from 2D simulations. Figure extracted from [134]. (d) Energy spectrum of protons, showing a monoenergetic spectra from 1D simulation. For comparison, the 2D simulation result is shown as well. (e) The corresponding energy spectrum of electrons from 1D and 2D simulations. Figures extracted from [135].

Therefore The maximum velocity scales with $a_0/\sqrt{n_e}$ and the ion phase space contains a flat-top structure, as shown in Fig. 2.4 (b) in the very early time ($t = 8\tau$). The corresponding HB front and the resultant high-density ion bunch at the velocity $v_{max,HB} = 2v_{HB}$ can be clearly seen in Fig. 2.4 (c). Note that, the ion phase space and the density distribution at this stage look very similar to the results from CSA driven by shocks with moderate Mach number $M = v_{shock}/c_s = 2 - 3$, where v_{shock} is the shock velocity[109–111]. This explains why sometimes the process is referred to as collisionless shock or electrostatic shock acceleration [141, 142].

As long as the laser is on, the HB process continues accelerating ions via a repeated process until all the adjacent ions are reflected to the same velocity $v_{max,HB}$ by the HB front, or in other words, when the compression layer reaches the initial rear surface of the target. After the whole target is set in motion, the acceleration changes to another stage named light sail (LS) acceleration. It can be regarded as a multi-staged acceleration of the whole target as a plasma slab by the radiation pressure to a nearly the same maximum velocity $v_{max,LS}$ which can be derived from the conservation of momentum in the non-relativistic case as [134]

$$\frac{v_{max,LS}}{c} = \frac{Z(1 + R - T)I_0\tau_L}{c^2 n_e m_i l} = \frac{(1 + R - T)\zeta}{2} \frac{Zn_c m_e}{m_i} \frac{a_0^2\tau_L}{n_e l} = \frac{(1 + R - T)E_L}{Mc^2} \quad (2.59)$$

where l is the initial target thickness, M is the target mass.

Clearly, the maximum velocity is not limited to $v_{max,HB}$ but can reach higher values depending on the laser and target parameters. It scales more rapidly with $a_0^2\tau_L$ as compared to the TNSA mechanism and inversely proportional to the initial areal density $\sigma = n_e l$. Such a scaling has been verified experimentally recently [42].

Fig. 2.4 (b) presents a typical loop structure in the ion phase space at later time ($t = 10, 14, 19\tau$) owing to the multi-staged acceleration process at LS stage, which is analogous to the PSA in the conventional radio frequency (RF) linac [135]. The ions are synchronously accelerated and bunched, resulting in a high density, monoenergetic ion beam (see Fig. 2.4 (d)). Nevertheless, the multidimensional effects should be addressed. For example, Fig. 2.4 (f) show that the electron heating is almost negligible in 1D, whereas in 2D, there is a substantial electron heating resulting from the target deformation due to the inhomogeneous transverse laser intensity distribution. Consequently, the ion spectrum is significantly broaden as compared to 1D simulation results, as shown in Fig. 2.4 (d). A large number of theoretic studies have been devoted to this issue, for example [134–136, 138, 139, 143, 145].

Chapter 3

Experimental Methods

In this chapter, the basic experimental methods are introduced. Generally speaking, it contains three main components: a high intensity laser system, targets, and the related diagnostics. Brief introductions about those parts will be presented in the following.

3.1 High Intensity Laser Systems

3.1.1 The ATLAS laser system

The Advanced Titanium: sapphire LASer (ATLAS) in Garching is a table-top TW CPA laser system based on conventional Ti:sapphire technology. It is based on the original ATLAS 10 Laser located at Max-Planck-Institut of Quantum Optics (MPQ) in 1996 [148] and has been reconstructed and upgraded several times. During the time of this thesis, the system located at MPQ and is available to deliver $\sim 100\ TW$ peak power with 5 Hz repetition rate (the so-called ATLAS 100) which is responsible for experiments described in Chap. 4, Chap. 5, and Chap. 7.

Laser setup

A layout of the ATLAS laser system is shown in Fig. 3.1 (a). The laser is seeded by a train of pulses of energy $E_L \sim 5\ nJ$ and $\tau_L \sim 20\ fs$, produced by a modified broadband Femtolasers Rainbow oscillator with 70 MHz repetition rate [149]. The output pulses from the oscillator are guided through a first 10 Hz multi-pass (8-pass) Ti:Sapphire amplifier before the stretcher. This amplifier is referred to as preamplifier, with the purpose of providing sufficient seed energy for the regenerative amplifier in order to improve the ns-contrast of the laser pulse [150]. 10 pulses per second out of the 70 MHz train are boosted to an energy of $\sim 50\ \mu J$. After preamplifier, the pulses are stretched to a duration

of 300 *ps* in a Martínez-type grating stretcher [151]. An acousto-optic programmable dispersive filter [152] (DAZZLER, Fastlite) is located at the exit of the stretcher to correct higher order dispersion for optimum pulse compression. The stretched pulses are then sent through a regenerative amplifier [153]. A Pockel cell acts as a 10 Hz pulse picker to select the highest energy pulses from the pre-amplifier which are then amplified from a few *μJ*-level to ∼ 2 *mJ* of energy in the regenerative amplifier. In addition, an acousto-optic programmable gain control filter [154] (MAZZLER, Fastlite) is implemented in the regenerative cavity to obtain an uniform amplification over a broad spectral range and thus prevent gain narrowing. As a consequence, a spectral bandwidth of ∼ 80 nm FWHM after the regenerative amplifier and ∼ 50 nm FWHM through the entire amplification chain is obtained. Next, the pulses pass through a series of multi-pass Ti:Sapphire amplifiers. Finally, the system delivers ∼ 3 *J* pulse energy with 5 Hz repetition rate behind the final amplifier.
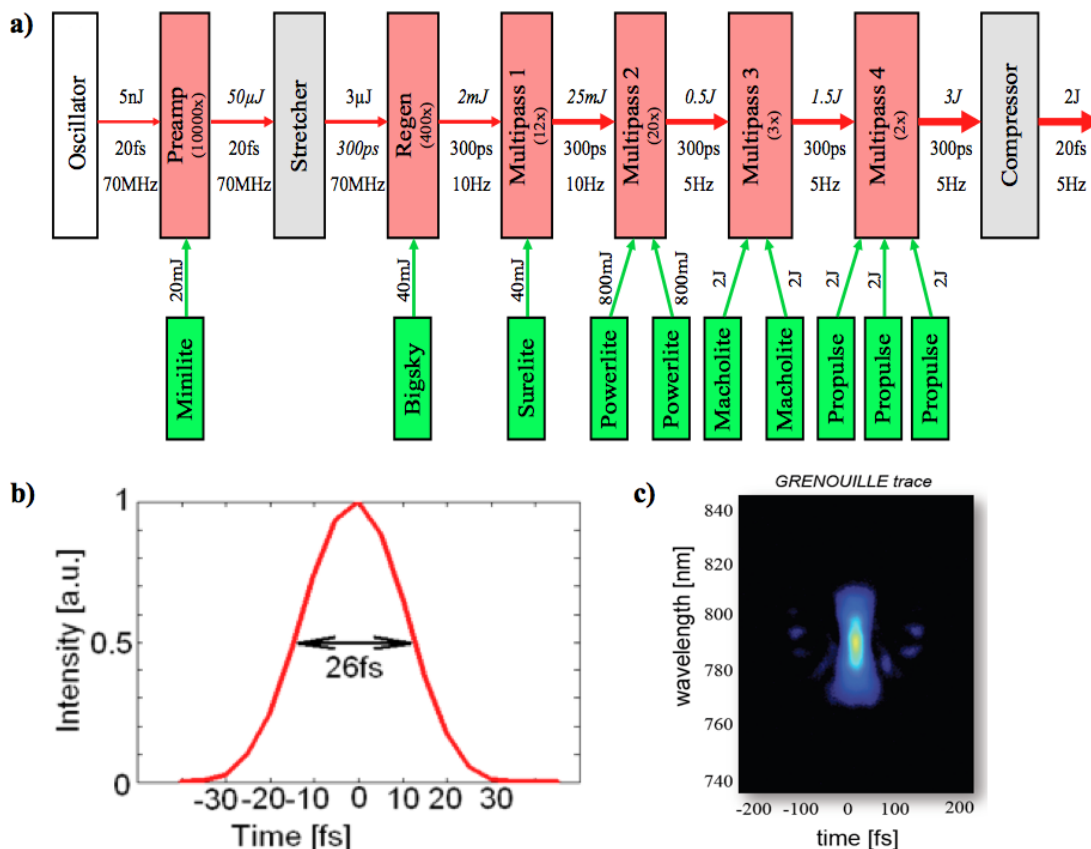

Fig. 3.1 | (a) Layout of the ATLAS laser system. (b) The temporal shape of ATLAS shows a typical pulse duration of 26 fs, which is characterized with a FROG device (GRENOUILLE, Swamp optics). The corresponding raw GRENOUILLE trace is shown in (c). Courtesy of J. Wenz and K. Khrennikov, MPQ

After the amplification chain, the pulses are guided to an adaptive mirror incorporating a Shack-Hartman wavefront sensor [155] to optimize the wavefront of the laser pulses before they enter the compressor. Afterwards, the pulses are compressed to a duration of $\sim 20\,fs$ FWHM centered at 800 nm wavelength by a negative-dispersion grating compressor. The pulse duration is determined by a GRENOUILLE device [156] (GRENOUILLE, Swamp optics) based on frequency resolved optical gating (FROG) technology [157]. An example is shown in Fig. 3.1 (b), presenting a typical ATLAS FWHM pulse duration of 26 fs retrieved from the raw FROG image (see Fig. 3.1 (c)). In the end, one pulse contains about 2 J energy at the exit of the compressor owing to $\sim 70\%$ transmission efficiency of the compressor.

Temporal contrast and laser focus

For the experiments presented in this thesis, the temporal contrast and focusability of the laser beam are the most important parameters. In the following a detailed description of those parameters are given.
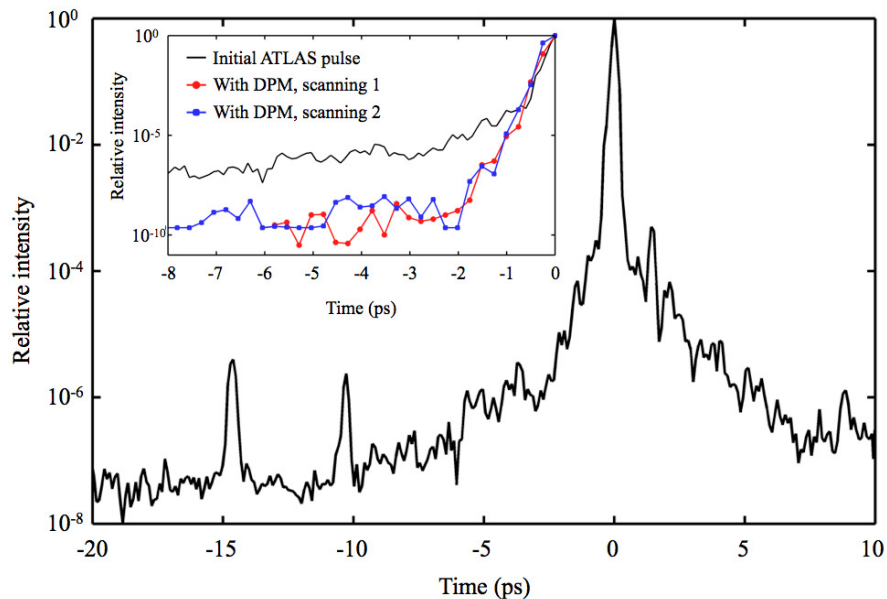
Fig. 3.2 | Third order scanning autocorrelation (Sequoia, Amplitude) of the ATLAS laser system at full power. The prepulses at -15 ps and -10 ps are the artificial ghost of the post pulses. The inset shows the measured curve with the initial ATLAS pulse with a zoomed region between -8 ps to 0 ps (black) and the corresponding enhanced curves from two individual scans with a double plasma mirror setup after the compressor. Here Time < 0 corresponds to the pulse front.

The temporal structure of ATLAS laser pulse is characterized by a commercial third oder scanning autocorrelator (Sequoia, Amplitude). A typical result is shown in Fig. 3.2, presenting a temporal contrast of $1:10^{-6}$ at 5 ps before the main peak. Here the temporal

contrast is defined as the ratio with respect to the main peak. In order to further enhance the contrast, a so-called re-collimating double plasma mirror (DPM) setup is implemented after the compressor at MPQ as part of this PhD work. Basically, a plasma mirror serves as an ultrafast optical shutter owing to the suddenly increase (within some femtoseconds) in reflectivity when an initially dielectric target is ionized and converted into an overdense plasma [158, 159]. The contrast enhancement simply depends on the ratio of the plasma and the initial target reflectivity. The DPM setup at MPQ is described in depth in [160]. A significant contrast enhancement by more than three orders of magnitude has been achieved with the price of 50 % energy loss through DPM setup (see inset in Fig. 3.2).
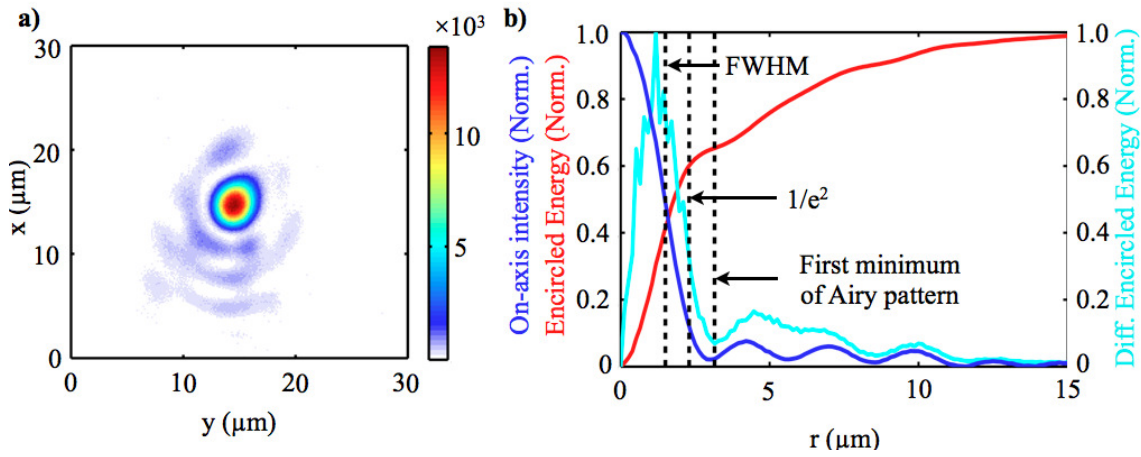
Fig. 3.3 | (a) The focal spot image of ATLAS laser after background subtraction. (b) A lineout of on-axis intensity extracted from (a) that normalized to the peak intensity (blue) and the corresponding encircled energy (red) and the first derivative of the encircled energy (cyan) are plotted as a function of radius. The black dashed lines are used to visualize the values of the radius of the FWHM, $1/e^2$, and the first minimum of Airy pattern, respectively.

		Uniform flat-top	Gaussian beam
FWHM	Diameter	$1.03\lambda F_\#$	$1.50\lambda F_\#$
	Encircled energy	50%	50%
$1/e^2$	Diameter	$1.65\lambda F_\#$	$2.54\lambda F_\#$
	Encircled energy	76.6%	86.5%
First minimum of Airy pattern	Diameter	$2.44\lambda F_\#$	\
	Encircled energy	83.8%	\

Tab. 3.1 | Different characteristic Diameters of focal spot and corresponding encircled energy for uniform circular beam and Gaussian beam with a truncated ratio $T = 0.5$, where $T = d_{1/e^2}/D$ is defined as the ratio of the input Gaussian beam $1/e^2$ diameter d_{1/e^2} to the clear aperture D of the focusing optics. For $T = 0.5$ it approximates an untruncated Gaussian beam. The detailed derivations of those diameter values of the Gaussian beam can be found in [161].

For all the experiments at MPQ, A 90° off-axis parabolic (OAP) mirror with a clear aperture $D = 100$ mm and an effective focal length $f = 200$ mm is used to focus the

pulses onto the targets, corresponding to a F-number $F_{\#} = f/D$ of 2.5 for the ALTAS laser (diameter of 80 mm). The laser focus is magnified and monitored by a 10× plan-apochromatic microscope objective along with a 14-bit CCD camera. A typical focal spot image of ATLAS laser is shown in Fig. 3.3 (a). An Airy-shape focus is clearly seen from this image owing to the fact that the ATLAS laser has a uniform flat-top beam profile rather than a Gaussian profile. A quantitatively comparison on the focusability between an uniform flat-top circular beam and a perfect Gaussian beam is shown in Tab. 3.1. Clearly, the focusability differs considerably with different beam profiles.

To further analyze the focus, the line out of the focus, encircled energy and its first derivative as a function of radius are extracted from Fig. 3.3 (a), where the encircled energy ratio was calculated by comparing the integral quantities of the readout in the full image area detected by the camera and the readout inside different radii. It provides an estimated FWHM diameter spot size of 3 μm containing 40 % of the pulse energy. Whereas 60 % and 65 % of the energy is encircled within the $1/e^2$ diameter of 4.6 μm and within the first minimum of the Airy pattern with a diameter of 6.3 μm, respectively (see Fig. 3.3 (b)). Considering an on-target energy of 400 mJ on a daily basis due to the energy loss through DPM and beamline, it yields a measured peak intensity of $1.0 \times 10^{20} W/cm^2$. Also, the other different relevant laser intensities are listed in Tab. 3.2.

	Intensity	a_0
Theoretic peak intensity	$1.2 \times 10^{20} W/cm^2$	7.5
Measured peak intensity	$1.0 \times 10^{20} W/cm^2$	6.8
Mean intensity within FWHM diameter	$7.4 \times 10^{19} W/cm^2$	5.9
Mean intensity within $1/e^2$ diameter	$4.8 \times 10^{19} W/cm^2$	4.7
Mean intensity within first minimum of Airy pattern	$2.8 \times 10^{19} W/cm^2$	3.6

Tab. 3.2 | Different relevant ATLAS laser intensities. For the theoretic peak intensity, it is calculated by substituting the measured FWHM diameter of the focused pulse into Eq. 2.12.

3.1.2 The Astra Gemini laser system

The Astra Gemini laser is a Ti:sapphire based, high power, ultra-short pulse laser system located at the STFC Rutherford Appleton Laboratory (RAL) at UK, which is one of the most powerful Ti:sapphire laser systems in the world. It is an extension of Astra laser system with a two-beam design which can delivers two synchronized 0.5 PW laser pulses every 20 seconds (the so-called Gemini) and is utilized for experiments described in Chap. 6.

Laser setup
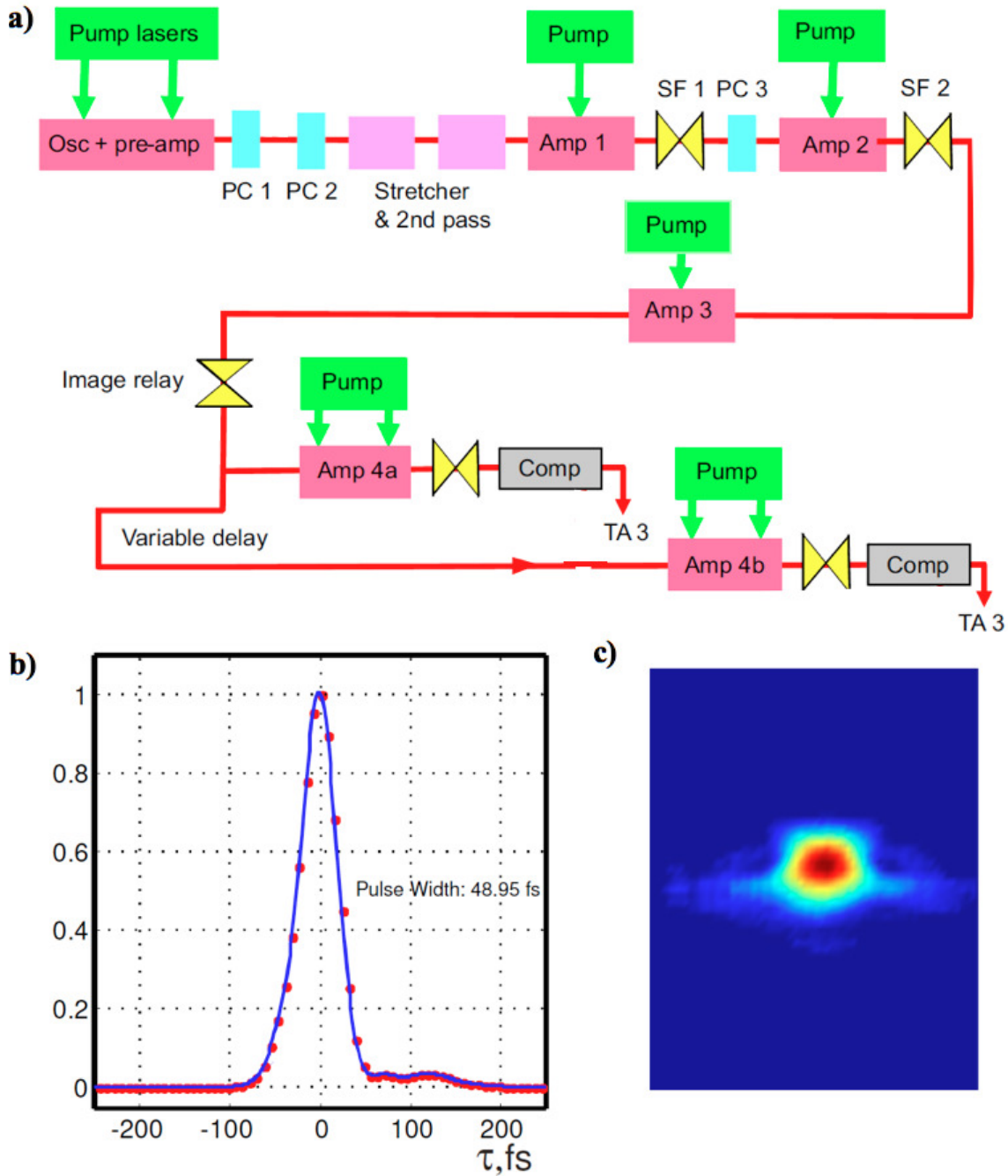
Fig. 3.4 | (a) Layout of the Astra Gemini laser system. Adaption from [162]. (b) Pulse profile and (c) the corresponding raw FROG trace at the output of the Gemini compressor, showing a pulse duration of 50 fs. Figures extracted from [163].

Fig. 3.4 (a) shows the layout of the Astra Gemini laser. The frond-end consists of a commercial Femtolasers oscillator delivering pulses of 12 *fs* with 75 *MHz* repetition rate. These pulses are stretched to 7 *ps* and guided through a *kHz* 9-pass Ti:sapphire

preamplifier to boost the energy. The 1 *kHz* amplified pulses train is selected at 10 *Hz* using a fast Pockels cell (PC) and sent to the stretcher. Each pulse is stretched to either 530 *ps* (for Astra only) or 1060 *ps* (for Astra Gemini). Later, the pulses are sent through an amplification chain which consisting three sequential 4-pass Ti:sapphire amplifier with a FWHM spectral band width of 42 nm, delivering about 1.2 *J* at the output of the Amplifier 3. Next, the amplified pulses are sent either to the Astra target area or used as the source for Gemini. It then split into two halve beams. In an ideal condition, after its individual 4-pass amplifier, each beam can be amplified as much as 25 *J* with a diameter of 150 mm.

Finally, the output pulses from the final amplifier is compressed to a FWHM duration of ∼ 50 *fs* centered at 800 nm wavelength with a grating compressor, as shown in Fig. 3.4 (b) and (c). An energy of about 15 *J* in a single pulse after the compressor is estimated assuming 60 % transmission of the compressor.

Temporal contrast and laser focus

Similar to the ATLAS laser, a re-collimating DPM setup for contrast enhancement is available in Astra Gemini [164]. The measured laser contrast is shown in Fig. 3.5. The laser system presents a temporal contrast of $1:10^{-5}$ at 5 *ps* before the main peak and has been improved by around 4 orders of magnitude by using the DPM setup, reaching an significantly enhanced contrast of $1:10^{-9}$. The overall throughput after DPM is measured to be 48 ± 5% [164].
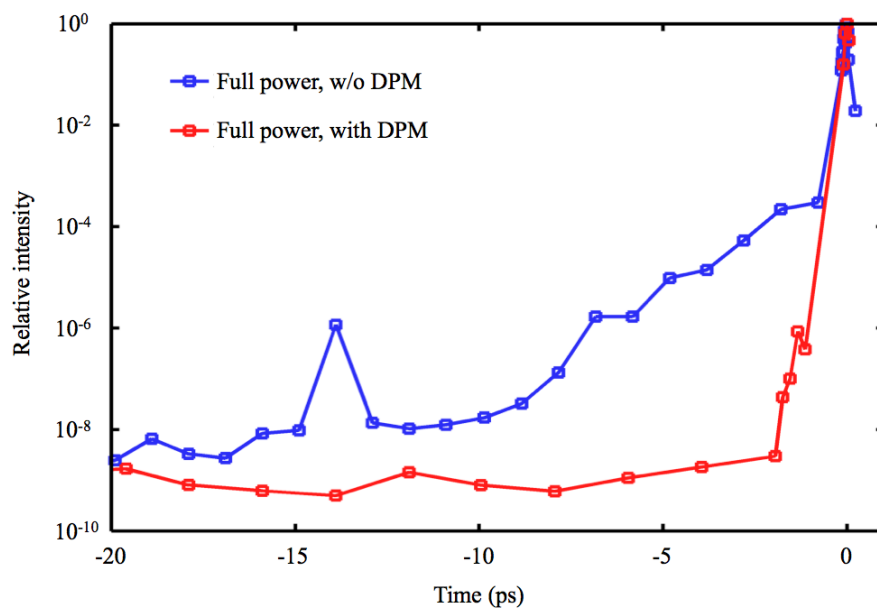

Fig. 3.5 | Astra Gemini laser contrast characterized with a third order scanning autocorreletor (Sequoia, Amplitude) at full power (black curve). The laser contrast is further enhanced by using a DPM setup installed after the compressor (red curve). Courtesy of P. Foster, CLF.

After the DPM, the laser pulse is focused using a f/2 OAP with an effective focal length f = 300 mm. Note that the OAP has a 2 cm diameter hole in the centre, allowing diagnostics of backscatter radiation. Like in ATLAS, the focus is determined using a 15× microscope objective in combination with a 16-bit CCD camera. The typical dynamic range for such kind of laser focal imaging is about 2-3 orders of magnitude based on the ratio between the bit depth of the camera used for the focal imaging and the normal noise readout level of a few 100 counts (see Fig. 3.3 (a) and Fig. 3.6 (a)). In order to enlarge the observed dynamic range, a so-called sequential unsaturated-saturated imaging method was employed in Astra Gemini. The results are published in [165].
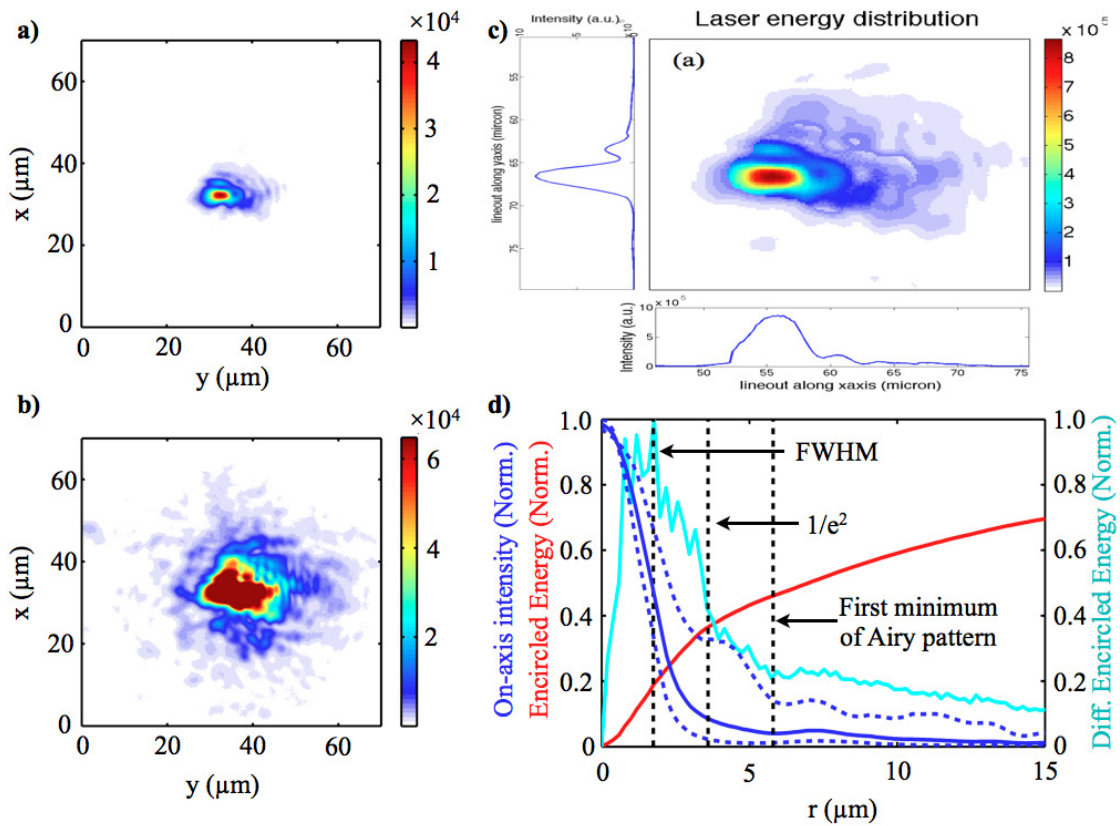
Fig. 3.6 | By using sequential images of unsaturated focal spot image (a) and saturated focal spot image (b), we obtain an enhanced focal spot image with high dynamic range of Astra Gemini laser (c). (d) The normalized on-axis intensity distribution (blue) extracted from (c) and corresponding encircled energy (red curve) and the first derivative of the encircled energy (cyan curve) are plotted as a function of radius. Here, the dashed blue curves shows the measured intensity lineout extracted along x and y axis, respectively. While the solid blue curve represents a fitting profile with calculated radii of equal-area circles. Again, the black dashed lines are used to visualize the values of the radius of the FWHM, $1/e^2$, and the first minimum of Airy pattern, respectively.

As shown in Fig. 3.6 (a) and (b), a saturated focal image is obtained by irradiating the laser pulse through the imaging system with medium power (1 mJ) so as to saturate

the centre part but keep the camera running without damage and get readout in the outer area; while the unsaturated image is sequentially obtained by attenuating the laser with a reflective optics, in our case, one special mirror with 5 % reflectivity. The relative ratio could be also derived from data by comparing the readout values located in the same area of two images. The average ratio derived from the data is 21, which fits very well with the actual reflectivity of the mirror. Based on this method, the dynamic range was further enhanced to be about 4 orders of magnitude by joining these two images, as shown in Fig. 3.6 (c). Owing to the experimental limitation, the laser focal spot in Astra Gemini could only be optimized to the tightest spot with an imperfect elliptical shape. Clearly, there is a big difference for different axes. In order to minimize the quantities for characterizing the focal spot, in the following analysis a fitting laser intensity profile is introduced based on equal-area circles approximation, where we assume the area of the circles are equal to the measured ellipses under the same intensities. We then estimate a FWHM diameter of 3.5 μm containing 18 % of the pulse energy. While 36.4 % and 46 % of the energy is encircled within the $1/e^2$ diameter of 7.2 μm and within the first minimum of the Airy pattern with a diameter of 11.6 μm, respectively (see Fig. 3.6 (d)). A peak intensity of $2.3 \times 10^{20} W/cm^2$ was obtained from the measured focal spot image with the laser pulse duration of 50 fs FWHM and 4.5 J laser energy on target. All the relevant laser intensities are shown in Tab. 3.3. Not like in the ATLAS laser case (c.f. Tab. 3.2), the actual values are significantly reduced as compared to a laser with a perfect Gaussian profile. To a certain extent, this may be attributed to the hole in the parabolic mirror and the absence of the adaptive optic system which is developed but not used for the experiments presented within the framework of this thesis.

	Intensity	a_0
Theoretic peak intensity	$6.0 \times 10^{20} W/cm^2$	16.8
Measured peak intensity	$2.3 \times 10^{20} W/cm^2$	10.4
Mean intensity within FWHM diameter	$1.7 \times 10^{20} W/cm^2$	8.9
Mean intensity within $1/e^2$ diameter	$8.5 \times 10^{19} W/cm^2$	6.3
Mean intensity within first minimum of Airy pattern	$2.6 \times 10^{19} W/cm^2$	3.5

Tab. 3.3 | Different relevant Astra Gemini laser intensities. For the theoretic peak intensity, it is calculated by substituting the measured FWHM area into Eq. 2.12.

3.2   Targets

In this section, two novel nano targets used for the presented experiments in the framework of this thesis will be briefly introduced. One is diamond-like carbon (DLC) foils, the other is carbon-nanotube foam (CNF) targets.

3.2.1   DLC Foils

The fabrication of nm thin diamond-like carbon (DLC) foils is self-developed in our laboratory employing cathodic arc deposition technique (CAD) [166]. By igniting an arc on a graphite cathode (graphite rod, POCO graphite sarl), highly ionized carbon plasma is generated and flowed towards the anode. A portion of the generated plasma is then guided through a 90° magnetic duct to filter out macro particles on the order of 0.1 to 10 μm [167]. Afterwards, the carbon ions are deposited on the substrate (polished silicon wafer with a thin layer of NaCl) with the deposited energy controlled by a substrate bias. After deposition, the grown films are floated to steel target holders over a diameter of 1 mm, as shown in Fig. 3.7 (a).
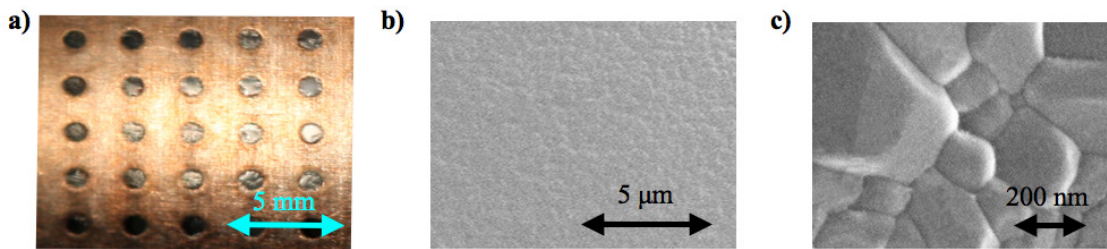
Fig. 3.7 | (a) A microscope image of freestanding DLC foils. (b) and (c) show SEM images of a freestanding DLC foil with different scales. Adaption from [168].

The produced DLC foils is a metastable form of amorphous carbon with a mixture of sp^2 and sp^3 hybridized carbon atoms. Owing to the high fraction of sp^3 bonds, DLC foils possess exceptional diamond-like properties such as high tensile strength, hardness, heat resistance, and optically transparence, making it a perfectly suitable material for ultrathin, freestanding targets. In addition, the produced DLC has super smoothness, which is essential for laser driven ion acceleration. It shows almost perfect smoothness with a $10 \times 10 \ \mu m^2$ scale (see Fig. 3.7 (b)) while a fluctuation with a size of 100 nm appears with $1 \times 1 \ \mu m^2$ scale (see Fig. 3.7 (c)). In fact, the surface structure is mainly arised from the smoothness of the NaCl layer on the substrate. Based on the CAD technique, freestanding DLC foils with thickness ranged from 3 nm to 60 nm can be produced [168]. The average density of DLC foils is $(2.7 \pm 0.3) \ g/cm^3$, corresponding to a highly overdense

plasma electron density of $470\pm52\ n_c$ for $\lambda_0 = 800nm$ assuming full ionized carbon atoms. The fabrication and characterization of DLC foils are described in depth in [169, 170].

Laser damage threshold

Knowing the laser damage threshold for targets is of great importance for laser plasma experiment since it indicates when the target start to ionize. The laser damage threshold of DLC foils is measured at MPQ.
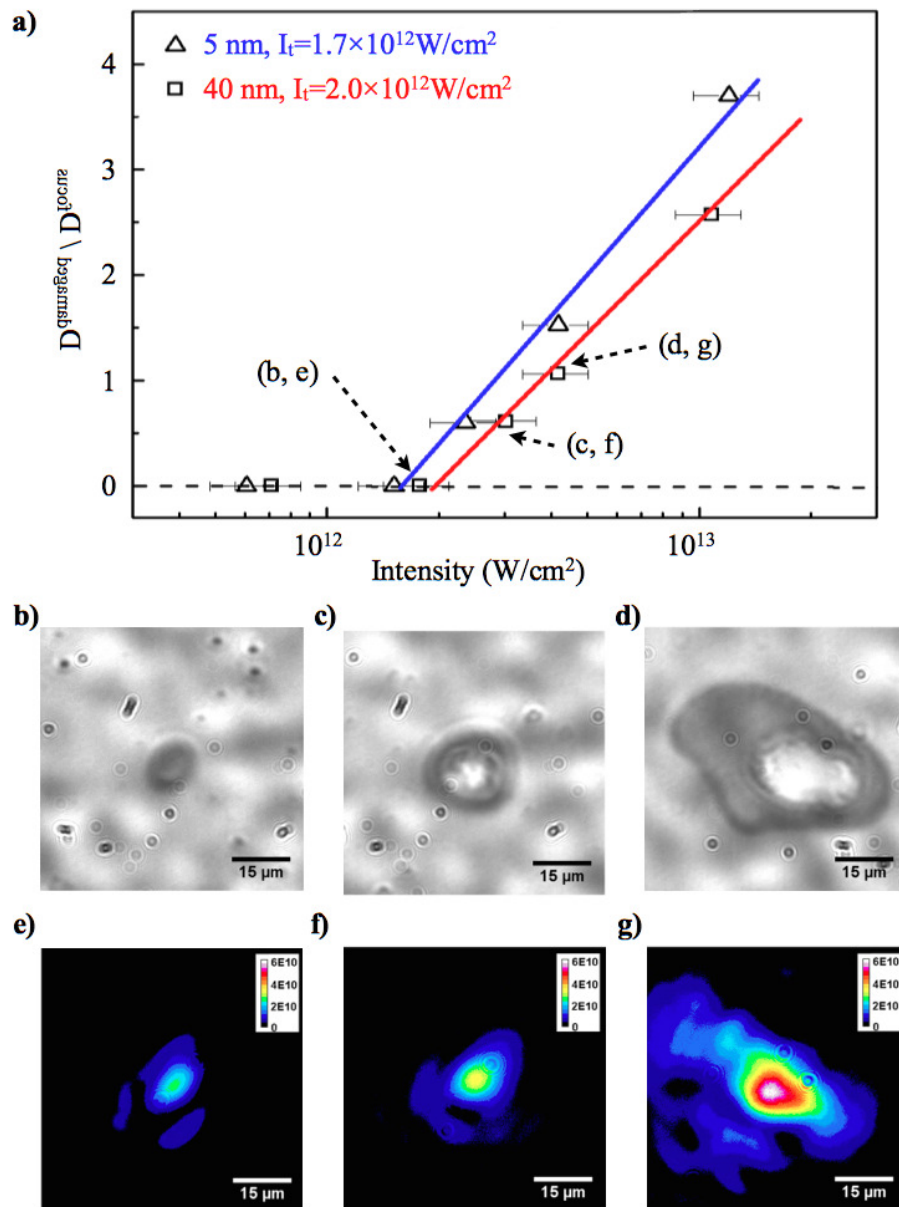

Fig. 3.8 | (a) Measurements of damage spot size for DLC for varying laser intensity. (b) - (d) show raw images of damaged spot while (e) - (g) are the corresponding laser intensity distribution, respectively.

The result is shown in Fig. 3.8. In the experiment, the damaged spots of DLC foil were monitored with the same imaging setup for laser focal spot (see Sec. 3.1.1) after each shot with attenuated ATLAS laser pulses (Fig. 3.8 (b) - (d)). The measured diameters of the damaged spots ($D_{damaged}$) are then compared with the incident laser focal spots (D_{focus}) for varying laser intensity (Fig. 3.8 (e) - (g)). The damage threshold I_t is inferred by interpolating the measurements to undamaged area when $D_{damaged}/D_{focus}$ approaching zero. The damage threshold does not deviates much for different target thicknesses. From Fig. 3.8 (a) we estimate a $I_t = 1.7 \times 10^{12} W/cm^2$ and $I_t = 2.0 \times 10^{12} W/cm^2$ for 5 nm DLC and 40 nm DLC, respectively.

Laser energy transmission

After ionization, the target expands rapidly owing to the increased hot electron population via different absorption mechanism (see Sec. 2.3.3), resulting in a significant pre expansion of the target before the main pulse arrives. The main pulse is then interacting with an expanded target with a reduced effective density n_{eff} rather than with the initial target. Extraction of the effective density or the pre expansion is therefore of most importance for the laser-plasma interaction. Laser energy transmission measurement provide an inline tool to determine the effective density.

In a simple physical picture, the laser energy transmission can be estimated as $T = \exp(-2d/l_s)$, where l_s is the skin depth given by Eq. 2.30 for a collision-less, box-shaped overdense plasma slab with thickness d and effective plasma density n_{eff}. For the sake of simplicity, we assume the shape of the plasma remains box-like, the areal density $\sigma = n_{e0}d_0 = n_{eff}d$ remains constant when premature expansion occurs with n_{e0} and d_0 the initial electron density and its initial thickness of the target, respectively. The transmission is then written as

$$T = \exp\left[-4\pi \frac{\sigma}{n_{eff}\lambda_0} \sqrt{\frac{n_{eff}}{\gamma n_c} - 1}\right] \tag{3.1}$$

Thus, based on Eq. 3.1, we can infer more details about n_{eff} and pre expansion of the target from the measurements of laser energy transmission.

Fig. 3.9 (a) shows the measurement of time-integrated laser energy transmission for Astra Gemini laser interacts with freestanding DLC foils. Clearly, the transmission decreases with increasing DLC thickness. The dashed black curves show the calculated transmission by Eq. 3.1 for a range of n_{eff}. The observed transmission values for DLC foils with various initial thicknesses cannot be explained by a single density value n_{eff}. This observation consists with the afore mentioned perspect that the targets are ionized long before the laser pulse reaches its peak intensity (starts from the intensity level of

about $2.0 \times 10^{12} W/cm^2$ - the measured damage threshold) and then expands on a ps-timescale. For a fixed degree of expansion, thinner targets will be intrinsically heated more rapidly and decompress more rapidly, resulting in a lower n_{eff} as compared to thicker targets. Fig. 3.9 (b) shows n_{eff} inferred from the transmission measurements for different thickness DLC foils. n_{eff} is estimated to vary from $50n_c$ to $470n_c$, in good agreement with the densities expected for increasingly thick DLC targets exposed to a laser prepulse. The determination of pre-expansion is essential to understand the detailed process of applications such as laser driven ion acceleration. Besides, such pre-expansion of DLC foils has been observed in [171], where the effective electron density was determined in a different approach by means of high harmonics radiation generation.
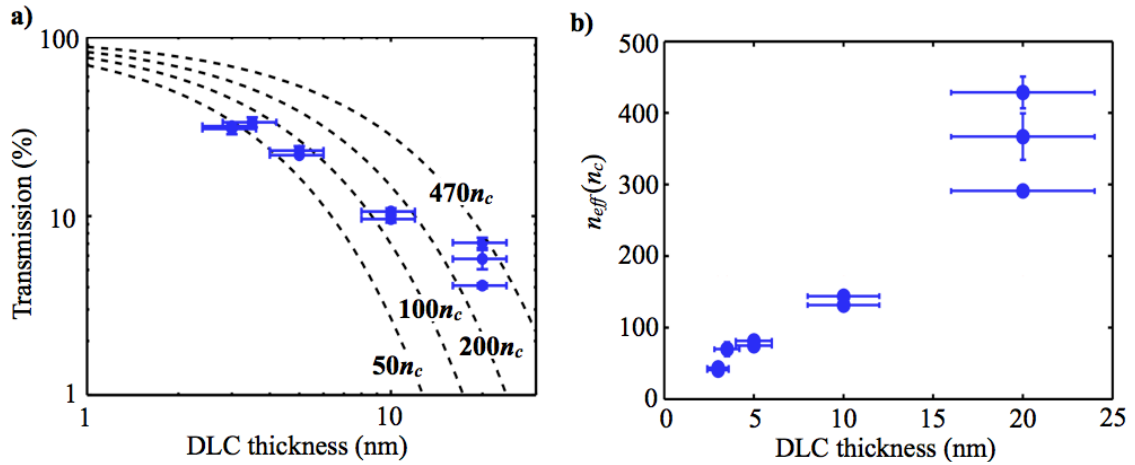
Fig. 3.9 | (a) Time-integrated laser energy transmission for the Gemini laser pulse interacting with DLC foils. Main sources of errors are uncertainties in the thickness measurement and background subtraction. The black dashed curves corresponds to the calculated transmission with $n_{eff} = 50n_c$, $100n_c$, $200n_c$ and $470n_c$, respectively. (b) The estimated effective density n_{eff} for different thicknesses of DLC foils derived from (a).

3.2.2 CNF targets

Ultrathin carbon nanotube foams (CNF) are fabricated through floating catalyst vapor deposition (FCCVD) [172]. Ferrocene/sulfur powder is sublimated under $85°C$ as catalyst, and carried into the reaction zone by a gas mixture of 1400 sccm argon and 10 sccm methane. The temperature of the reaction zone is $1100°C$. In the reaction zone, single walled carbon nanotubes grow out of the floating catalyst to a length of tens of micrometers within a few seconds, and self-assemble as bundles with a diameter of 10-20 nm. After their growth, nanotube bundles are transported to the deposition zone by the carrier gas, and deposited as a thin foam. The average interspace spaces between adjacent carbon

nanotube bundles is about 50-100 nm. Consequently, the foams are highly homogeneous above micrometer scale, as can be seen in Fig. 3.10.

Fig. 3.10 | (a) A SEM image of a freestanding CNF target. (b) The schematic of CNF target.

The thickness of the foam is controlled by the deposition time, allowing production of CNF with micron scale overall length and micron accuracy. Other important feature of CNF is that it can be 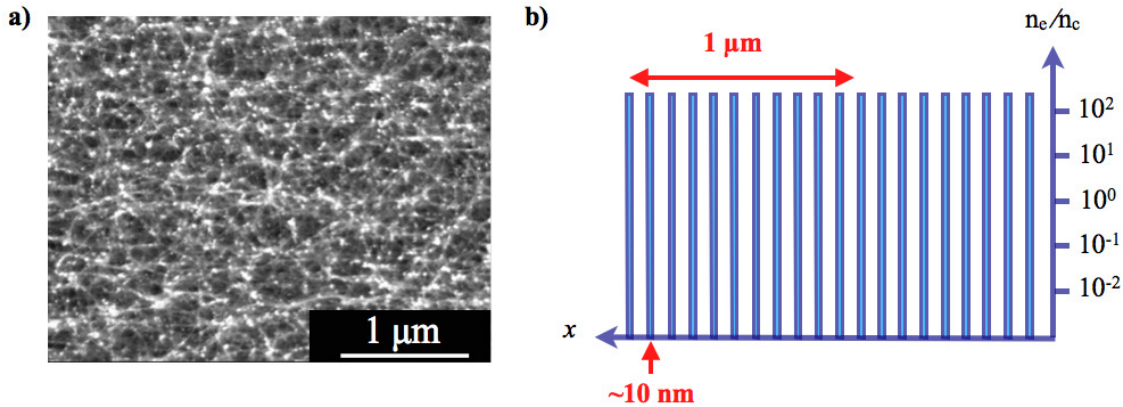coated onto solid target, like DLC foils. Its average density is controlled by the feeding rate of catalyst and methane. Under the parameters given above, the growth rate of the foam is $0.1 \, \mu g/cm^2/min$. The average density of the foam is (12 ± 6) mg/cm^3, which corresponds to a near-critical plasma density (NCD) of $(2 \pm 1) \, n_c$ if all the carbon atoms are fully ionized.

Laser damage threshold

CNFs are a highly absorptive material for lasers with center wavelength of 800 nm. Thus it has a much lower damage threshold as compared to transparent materials, for example, DLC foils. Fig. 3.11 (a) shows the experimental measurement results of damage threshold for CNF with varying laser pulse duration. For instance, CNF has a damage threshold of $I_t = 8 \times 10^{11} W/cm^2$ for a laser pulse with a duration of 45 fs. Therefore, for a Astra Gemini laser pulse, with an enhanced temporal contrast by DPM as shown in Fig. 3.5, the rising edge of such laser ionizes CNF approximately 5 ps Before reaching the peak. During these 5 ps, the plasma homogenizes further to form a reasonably uniform near-critical density (NCD) plasma on the scale of the laser wavelength ($\lambda_0 = 800nm$).

This simple interpretation is supported by hydrodynamic simulations. In Fig. 3.11 (a), hydrodynamic calculations carried out by MULTI-fs code [173] have been also plotted. A single carbon graphite layer with thickness of 20 nm was considered in the simulation as a single carbon nanotube bundle. Damage threshold was defined in the simulation either as partial vaporization or spallation of the layer, whichever comes first. The values extracted

from hydrodynamic simulations agree very well with the measured values. When the measured Gemini laser pulse is used, the bundle survives up to 5 ps before the peak of the main pulse. At this moment laser intensity is above $10^{11} W/cm^2$ and it is increasing exponentially with time. In less than 2 ps, the bundle is completely vaporized and turns into a plasma cloud with 5-8 eV electron temperature and expanding with a velocity of around 2×10^6 cm/s. Starting from this time, the remains of the bundles interact each other and with the laser field in a complicated way.
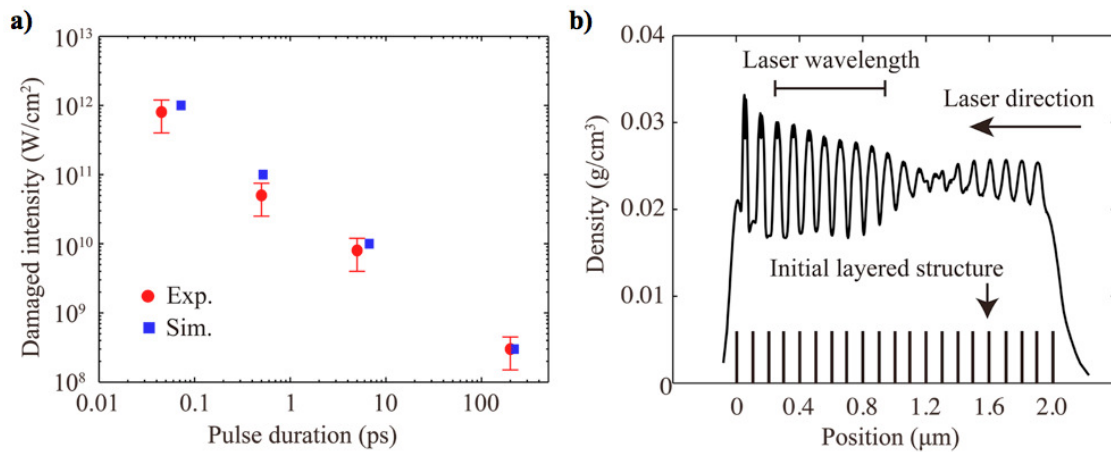
Fig. 3.11 | (a) Measurements of damage threshold for CNF (red circles) with varying laser pulse duration. The values extracted from hydrodynamic simulations (blue squares) are plotted as well (Courtesy of R. Ramis, Universidad Politécnica de Madrid), agreeing well with the measured ones. (b) Simulated longitudinal density profile of a multi-layer target (resembling a 1D-structured target) at the end of prepulse.

To study qualitatively this situation, the 1D evolution of a 2 micrometers multi-layer target with the same average density as the real target and with layers spaced 100 nms (i.e. the average distance between adjacent bundles) has been simulated during the last 5 ps of the laser prepulse. Fig. 3.11 (b) shows the longitudinal density profile at the end of the simulation (when laser intensity reaches $10^{16} W/cm^2$, the limit of validity of MULTI-fs code). The density is quite homogeneous, with sharp front and back borders. The small modulations reflect the initial layered structure. Their amplitude is 20 % in the back side of the foam and 10 % in the directly irradiated side. The homogenous density distribution of CNF is essential for the experiments described in Chap. 6.

Laser energy transmission

As discussed above, the laser energy transmission provide detailed information about the pre-expansion of the targets. Fig. 3.12 shows the measured laser energy transmission of freestanding CNF performed at Astra Gemini. In order to compare these two groups of

data for CNF and DLC targets, the transmission values are plotted as a function of areal density σ. Again, the transmission decreases with increasing target thickness (in here, the increasing areal density). While the laser transmission values through freestanding CNF are significantly higher at given areal density as compared to DLC foils owing to their much lower plasma density. Furthermore, The measured laser transmission through freestanding CNF is compared with the values from 3D PIC simulations, supporting our estimate of an average electron density between $1n_c$ and $3n_c$. For thicker CNF, comparison of the measured values to PIC simulation suggests higher densities around $6n_c$.
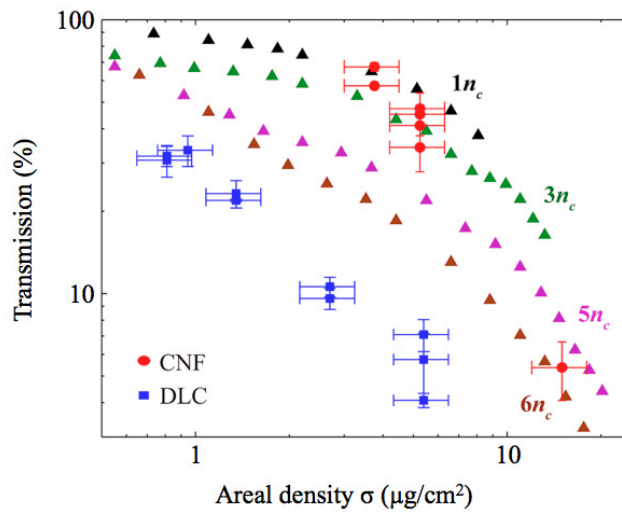
Fig. 3.12 | (a) Time-integrated laser energy transmission for the Gemini laser pulse interacting with CNF foils. The transmission for DLC foils extracted from Fig. 3.9 are shown for comparison. Error bars are the same as in Fig. 3.9. The triangles with different colors represent the transmission extracted from 3D PIC simulations performed for effective electron densities of $n_{eff} = 1n_c$, $3n_c$, $5n_c$ and $6n_c$ respectively.

3.3 Diagnostics

3.3.1 Utilized detectors

CR39

CR39 (Columbia Resin #39), or allyl diglycol carbonate (ADC), is a plastic polymer of chemical formula $C_{12}H_{18}O_7$ and a density of $\rho = 1.3 \ g/cm^3$. It is transparent in the visible spectrum but almost opaque in the ultraviolet range. A commercial type of CR39 (TASTARK, Track Analysis Systems Ltd) is used as a solid state nuclear track detector (SSNTD) in the scope of this thesis. When a particle moves through CR39, it ionizes the

material and deposits energy along its path. The chemical bonds break when the deposited energy exceeds a material dependent threshold, forming a track trail of the damage within CR39. Owing to the threshold, CR39 is insensitive to UV, X-ray, γ-ray and also electrons, allowing merely the detection of ions with energy above ~ 100 keV/nucleon.

Next, to make the damage track visible under a microscope, the track is enlarged by immersing in a caustic alkaline solution (NaOH, 6 mol/L, $80°C$) due to the different etching rate between the damaged and undamaged region. The etching process results in a conical hole in the surface of CR39 containing not only the position but also the spectroscopic information, and is then read out by a scanning microscope [174]. Due to the time consuming data analysis process, CR39 is only temporally involved in the described experiments in this thesis, mainly used as a cross-calibration detector.

Radiochromic film (RCF)

Radiochromic film (RCF) is widely employed in radiation dosimetry. It is based on radiochromic effect which involves a permanent color change on exposure to energetic radiation. A commercial poly-diacetylene based RCF (GafChromic EBT2, ISP International Specialty Products Inc.) is used in the framework of this thesis. In contrast to CR39, it is relatively insensitive to visible light but sensitive to all kinds of ionizing radiation, such as electrons, protons and heavy ions. EBT2 contains a 30 μm thick active layer where a micro-crystalline diacetylene (Lithium salt of pentacosa-10,12-diynoic acid, PCDA) is used as the sensitive component. The PCDA monomer undergoes a blue-colored polymerization process by exposing to ionizing radiation. Therefore, without additional imaging development, the initially colorless film turns darker blue proportionately to the absorbed dose.

For experiments described in Chap. 4, GafChromic EBT2 is employed for the proton dosimetry. The film is scanned by a CCD scanner system (Epson Perfection V700 Photo scanner) in landscape format in transmission mode with a resolution of 1200 dpi and recorded as 48-bit RGB tiff image with all image correction features turned off. The scanning is done 57 ± 1 hours after exposure to minimize uncertainty in optical density due to post-irradiation growth [175]. The red color channel is extracted and pixel values (*pv*) is converted into net optical density values (netOD). To determine the absorbed dose, an absolute dose-to-water calibration for the exact utilized film is done with a 6 MV clinical photon beam at Klinikum rechts der Isar in munich for doses between 0.1 and 8 Gy. The result is shown in Fig. 3.13 (a). Another dose calibration with different GafChromic EBT2 films with both photon and proton beams at various energies shows that the photon calibration can be also used for protons (see Fig. 3.13 (b)). This was also reported for the
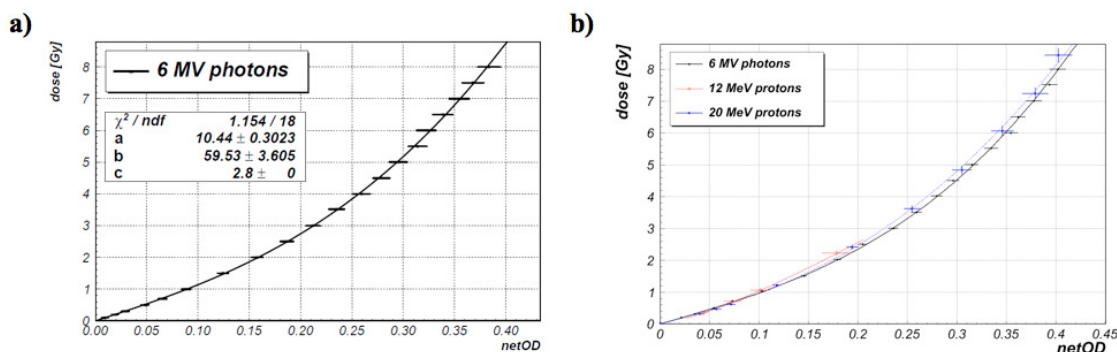
Fig. 3.13 | (a) Calibration curve (dose vs. netOD) for one used lot of radio chromic film (Gafchromic EBT2) using a 6 MV photon beam from a clinical linear accelerator. (b) Calibration curve for another lot of Gafchromic EBT2 film with a 6 MV photon beam as well as protons with 12 MeV and 20 MeV. Here, horizontal error bars are the standard deviation of the netOD across the chosen region of the interest irradiated with homogeneous dose. Error bars in dose (< 5% at lowest dose, and < 1% at highest dose) are not clearly visible on this scale.

predecessor EBT film (GafChromic EBT, ISP International Specialty Products Inc.) with the same active component as EBT2.

Noted that there is an under-response of RCF at very low proton energies [176, 177]. For instance, for the described experimental setup in Chap. 4, the mean proton energy in the active layer of the film was 3.1 MeV, where EBT was shown to underestimate the dose by 10% [177]. Measured dose values were therefore divided by 0.9, although we assume that the systematic uncertainty in this correction factor may be as large as ±20%. Due to the rising edge of the Bragg curve, the dose at the position of the cells (mean energy 4.45 MeV) was smaller than the dose at the position of the film (3.1 MeV in the active layer), as shown in Fig. 3.14. Therefore the doses measured with the film were multiplied with the stopping power ratio of protons in water at these energies (here: 0.76 ± 0.03 according to ICRU report 49 [178] and SRIM [179]) to obtain the dose at the position of the cells. The systematic uncertainty in the correction factor was obtained by running multiple simulations with variations in the air gap between exit window and cell holder as well as by accounting for the energy spread within the active layer. More details can be found in [86, 180].

Image plate (IP)

Image plate (IP) is an area detector based on photo stimulated luminescence (PSL) process [181–183]. It is a flexible plastic plate coated with fine Eu-doped phosphor crystal ($BaFBr:Eu^{2+}$). When exposed to radiation, a portion of the incident energy is stored mainly by exciting Eu^{2+} ions to a metastable state, yielding a population of Eu^{3+} state
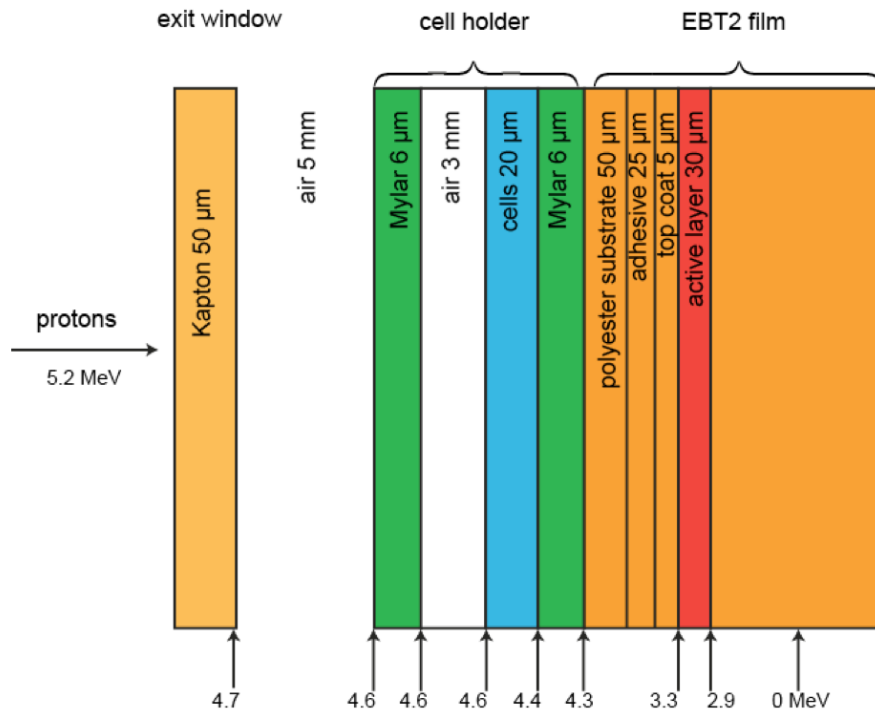
Fig. 3.14 | Simulation of proton energy loss through all layers involved in the presented experiments in Chap. 4 using SRIM.

and liberated electrons trapped in the vacancies of the halogen ions in the crystal lattice (i.e., F^+-centers). When stimulated by visible or infrared light, the trapped electrons at F^+-centers are released back to the conduction band and recombine with Eu^{3+} ions, converting them to Eu^{2+} ions. During this recombination, luminescence light (385 nm) is emitted which is proportional to the incident dose. Due to the small Eu^{2+} photoionization absorption value of 6.6 eV, IP is sensitive to any kind of radiation, including x-ray, electron, ions, and neutron.

In the framework of this thesis, two types of IP (BAS-IP TR and BAS-IP MS, Fujifilm) are used. IP film is read out by a special IP scanner system (FLA-7000 scanner, Fujifilm) which scans IP with a HeNe laser pulse (633 nm) and detects the PSL light with a photomultiplier tube (PMT) converting the light into electrical signals. The readout is stored in a logarithm digital image due to the logarithmically amplification by the PMT. As compared to other detectors, IP film has high sensitivity, high dynamic range ($\sim 10^5$) and high resolution ($\sim 25 \mu m$). Most importantly, it can be erased with an intense white light source after readout and be reused many times. Therefore IP has been used as the standard ions detector for the experiments described in Chap. 4, Chap. 5, and Chap. 7. Calibration of the utilized IP films was performed at the Maier-Leibniz-Laboratory (MLL) Tandem accelerator in Garching, a detailed description can be found in [180].

RadEye^{TM} silicon pixel detector

In contrast to all the afore-mentioned detectors such as CR39, RCF and IP which are only used as offline detectors, silicon pixel detector allows online real time detection of radiation. Typically, it is used incorporating with a scintillating phosphor screen, converting visible lights into electrical signals and read out. While for the presented experiments in Chap. 6, a commercial type of silicon pixel detector (RadEye^{TM} 1, engineering grade, Teledyne Rad-icon Imaging Corp.) is used as online ions detector. RadEye^{TM} 1 is a large-area imaging sensor module based on Complementary Metal-Oxide Semiconductor (CMOS) technology. It contains a large sensitive area (24.6 mm × 49.2 mm) composed of a 2D CMOS silicon photodiode array with 512 by 1024 pixels on 48 μm pixel pitch. Since optimized for visible light detection, RadEye^{TM} 1 module consists an active layer of 2 μm made of Si which is supported by a ceramic substrate. Additionally, a 2 μm SiO$_2$ passivation layer is placed on top of the active layer. The pixel value pv, i.e., the response to ion signals, scales linearly with energy loss $\triangle E$ of ions within the 2 μm Si active layer as [180]

$$pv = (1.09 \pm 0.12)\triangle E \, [keV] \qquad (3.2)$$

The signal is processed by a separate readout camera electronic module (Remote Rad-Eye camera system with ethernet interface, Teledyne Rad-icon Imaging Corp.) which is capable of parallel readout of up to 4 sensors. The readout is then saved in a 14-bit digital image. Afterwards, the signal is erased from the sensor and can be reused. Noted that, the reusability is strongly restricted on the radiation damage level, depending on the particle flux and dose. It is found that after irradiation of 20 MeV proton beam with a dose of 6×10^{10} protons/cm^2, the dynamic range decays to about 50% of initial value but the linear response to proton fluence still holds [180]. The RadEye^{TM} detector offers a high sensitive (single ion detection), a high dynamic ($\sim 10^5$) and high spatial resolution ($\sim 50\mu m$), making it a suitable online detector for laser driven ion acceleration.

Scintillating phosphor screen

The working principle of scintillating phosphor screen is straight forward. Upon exposure, it converts the incident energy into the form of light, i.e., scintillation. The emitted light can be collected with an electronic light sensor, e.g. CCD, CMOS and PMT.

In the presented experiments in this thesis, a scintillating phosphor screen (Kodak Biomax MS intensifying screen, PerkinElmer Inc.) is used for the online detection of energetic electrons. The phosphor layer is composed of mixtured phosphor powder (Gd$_2$O$_2$S:Tb)

in a urethane binder. The emitted 546 nm green light from the screen is detected by two types of electron multiplying CCD (EMCCD) (iXon EMCCD, Andor and ProEM, Princeton Instruments) in two individual experimental setups, respectively. The calibration is done by employing a tritium light source (Trigalight round source, mb-microtec) as a luminosity reference. The response for independent optical system is then obtained and cross related an absolute charge calibration with well-characterized electron beams [184]. It is worth mentioning that the calibration strongly depends on the tritium source age as it degrades over time, a repeated reference measurement is necessary in the long run. More details can be found in [160].

3.3.2 Spectrometers

Thomson parabola (TP) spectrometer
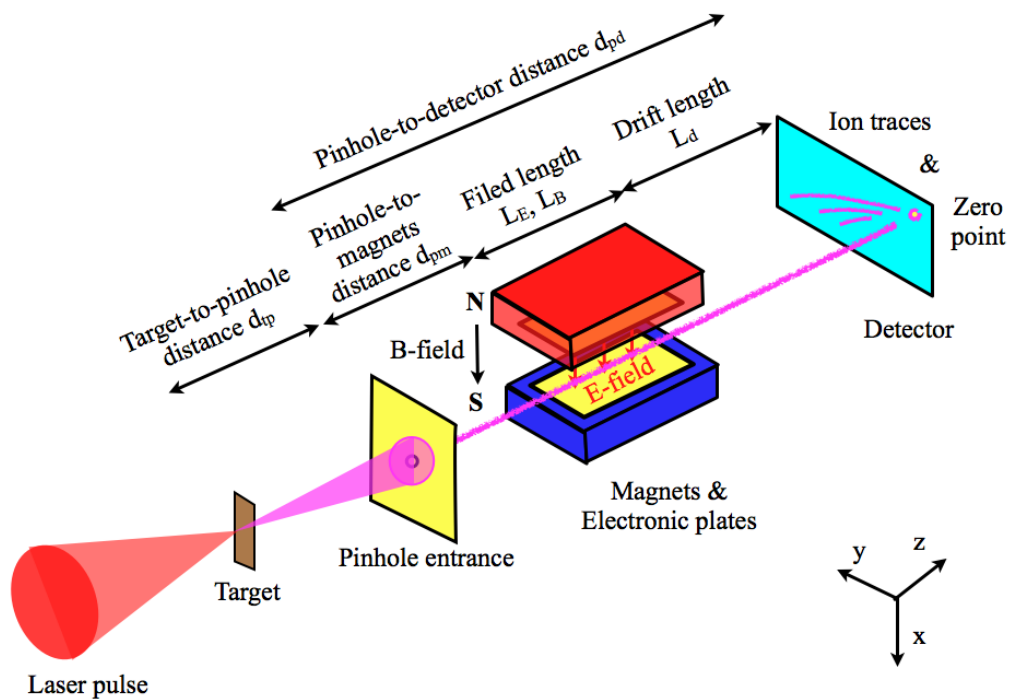
Fig. 3.15 | A schematic of a standard Thomson parabola (TP) spectrometer. Ions from a target are accelerated by ultra-intense laser pulses. A pinhole entrance is placed after the target with a distance of d_{tp} is used to select ion beams within a small solid angle Ω (typically $\sim 1 \times 10^{-7}$ sr). The selected ions are deflected in parallel magnetic and electric fields oriented perpendicular to the initial propagation direction of ions and with a length of L_E and L_B, respectively. After a drift of length L_d, the ions are detected by 2D area detector at the detector plane with a distance of d_{pd} to the pinhole. The image of the pinhole, i.e., the zero point, reflects the impact on the detector by uncharged particles.

Thomson parabola (TP) spectrometer [185] is one of the most commonly used spectrometers for detection of laser driven ion beams. As shown in Fig. 3.15, in a TP, parallel magnetic and electric fields are set up oriented perpendicular to the propagation direction of charged particles. The magnetic field is generated by a pair of permanent magnets supported by an iron yoke. While the electric field is provided by a pair of electronic plates (copper plate moulded on insulating plastic) separated with a gap of few centimeters.

A small fraction of the ions (within a solid angle Ω of $\sim 1 \times 10^{-7}$ sr) are selected by a pinhole entrance positioned in front of the parallel magnetic and electric fields and are deflected in two perpendicular directions when passing through the TP. The magnetic deflection scales with the charge-to-momentum ratio of ions and is perpendicular to the propagation direction as well as the electric deflection. While the electric deflection is proportional to the charge-to-energy ratio. The resulting ion traces are detected at the detector plane by a 2D area ion detector (see Sec. 3.3.1). The curvature of these traces depend on the charge-to-mass ratios of the ions, providing the spectroscopic information. The positions and numbers are then used to determine the respect ion energy spectrum.

In a standard TP configuration (see Fig. 3.15), where the location of electric field coincides with the magnetic field with the field length $L_E = L_B = l$, the deflections in the non-relativistic case is derived from the Lorentz equation (c.f. Eq. 2.8)

$$
\begin{aligned}
x(E_{kin}) &= \frac{q_i E l}{2 E_{kin}} \left(\frac{l}{2} + L_d \right) \\
y(E_{kin}) &= \frac{q_i B l}{\sqrt{2 m_i E_{kin}}} \left(\frac{l}{2} + L_d \right)
\end{aligned}
\tag{3.3}
$$

Here $q_i = Ze$ is the charge of ions and a simple assumption of constant fields is applied which holds its validation owing to the tiny pinhole used in the TP [186].

Hence, the well known parabola trace is given by

$$
y^2 = \frac{q_i B^2 l}{m_i E} \left(\frac{l}{2} + L_d \right) x
\tag{3.4}
$$

By fitting the calculated parabolas to the measured ion traces on the detector, one can extract the energy spectrum with respect to every involved ion species in a single shot.

For a TP, the energy resolution is determined by a certain minimum spatial interval that can be resolved in the ion traces. Typically, this minimum is referred to the diameter s of the pinhole image at the detector plane

$$
s \approx a(1 + d_{pd}/d_{tp})
\tag{3.5}
$$

with the initial pinhole diameter a, the target-to-pinhole distance d_{tp} and the pinhole-to-detector distance $d_{pd} = d_{pm} + l + L_d$.

The corresponding energy resolution $\triangle E_{kin}/E_{kin}$ is given by

$$\frac{\triangle E_{kin}}{E_{kin}} = \frac{2s/y(E_{kin})}{\left[1 - (s/2y(E_{kin}))^2\right]^2} \tag{3.6}$$

Substituting Eq. 3.4 into Eq. 3.6, we obtain a simple form for $\triangle E_{kin}/E_{kin}$ assuming $1 - (s/2y(E_{kin}))^2 \approx 1$

$$\frac{\triangle E_{kin}}{E_{kin}} = \frac{2s\sqrt{2m_i E_{kin}}}{q_i Bl(\frac{l}{2} + L_d)} \tag{3.7}$$

Clearly, smaller s (in other words, smaller pinhole diameter a), larger B, l, and longer drift length L_d are favorable for better resolution.

Note that, the standard TP can be adapted under certain circumstance. For instance, in a modified TP setup (TP-Gemini) for the presented experiments in Chap. 6, the electronic plates are located after the magnets and two perpendicular sequential entrance slits located in front of each field are used, acting as a pinhole. While in the described experiments in Chap. 4, there is absence of electric field in the TP setup (TP-MPQ). The detailed parameters are listed in Tab. 3.4.

	TP-MPQ	TP-Gemini
B $[T]$	0.58	0.14
E $[kV/m]$	0/0.03	7/0.015
l $[mm]$	100	200(150)
d_{tp} $[mm]$	650(810)	300(548)
d_{pd} $[mm]$	323(423)	855(607)
a $[mm]$	2.5(9)	0.4 (0.1)
L_d $[mm]$	203(303)	637(425)

Tab. 3.4 | Summary of utilized TPs used for the experiments in the scope of this thesis. TP-MPQ is responsible for experiments in Chap. 4. TP-Gemini configuration is responsible for experiments in Chap. 6, where the electronic plates are placed behind the magnets. For TP-MPQ, the numbers with and without parentheses are used in different combinations. For TP-Gemini setup, the numbers without parentheses are for magnetic field and those with parentheses are for electric field.

Wide angle spectrometer (WASP)

As discussed above, a TP can only resolve ion beams within a small solid angle. In order to obtain particle information over a large angular range, which is important for understanding the underlying physics of laser driven ion acceleration, a novel spectrom-

eter so-called wide angle spectrometer (WASP) is introduced. Basically, it is a magnetic spectrometer with a large acceptance angle, as shown in Fig. 3.16. Compared to the TP, a magnetic field with a gap of 14 cm and a total field length l of 20 cm is employed alone with the absence of the electric field. The magnetic field is provided by two yoked pair of permanent magnets, each one has a field length of 10 cm and a magnetic field B of $0.1 - 0.24T$. In addition, a long entrance slit of few 100s μm width a instead of a tiny pinhole is placed in front of the magnetic field. The slit entrance is made of two iron plates (ferromagnetic) in order to shield the magnetic field, and directly attached to the yoked magnets. This configuration enables angularly-resolved high-accuracy energy distribution measurement.
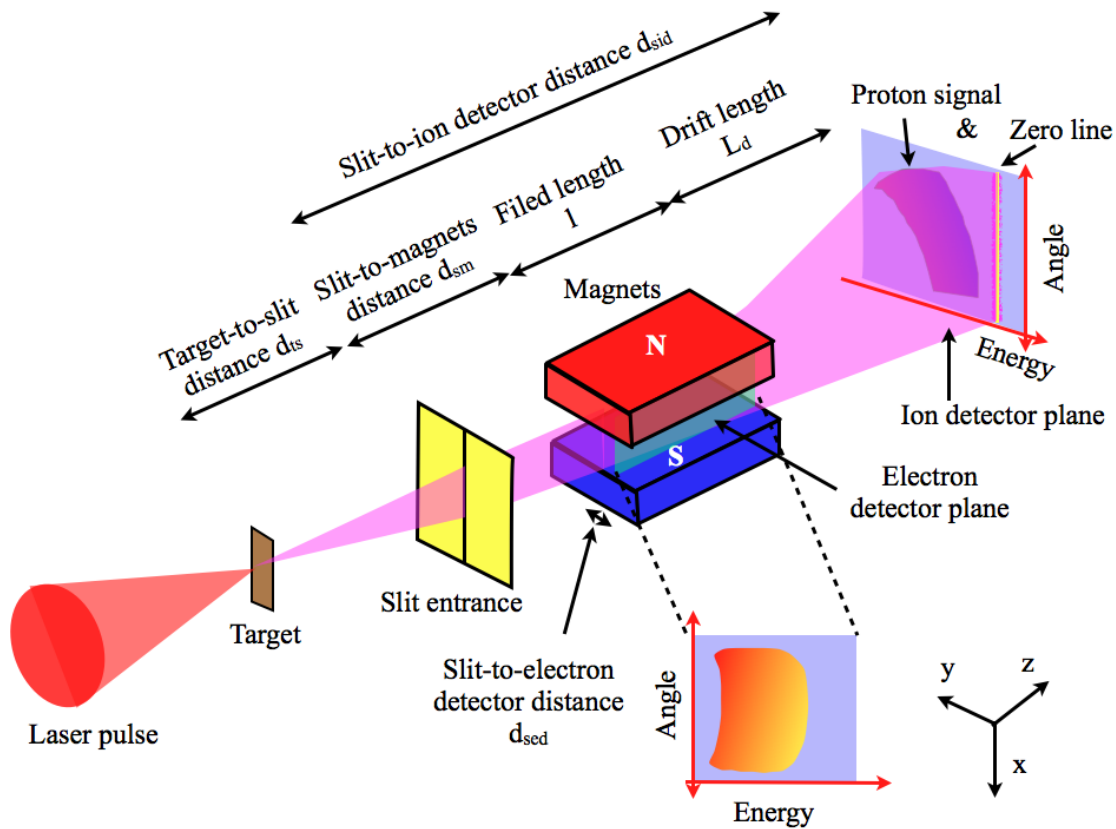
Fig. 3.16 | A schematic of a wider angle spectrometer (WASP). In contrast to TP, a long slit entrance placed d_{ts} away from the target is used to collect charged particles with a broad angular range. The selected particles are deflected by a magnetic field with its orientation perpendicular to the laser propagation direction and with a field length of l. After a drift length of L_d, ions are captured by a 2D area ion detector at the ion detector plane (xy plane) at a distance of d_{sid} to the slit entrance. While electrons are detected by a scintillating phosphor screen (see Sec. 3.3.1) at the electron detector plane (xz plane) with an offset of d_{sed} from the laser propagation direction.

Ions are captured at the ion detector plane (xy plane) with an area detector such as CR39, IP or RadEye^{TM} (see Sec. 3.3.1). Differ from other ion wider angle spectrometer

designs [187, 188], the moderate magnetic field employed in our setup $(0.1 - 0.24T)$ allows simultaneously detection of angular resolved energy distribution of both ions and electrons. A scintillating phosphor screen (see Sec. 3.3.1) placed at the xz plane with an offset of d_{sed} from the laser propagation direction is used to detect electrons.

The corresponding traces for ions and electrons can be calculated based on the Lorentz equation (Eq. 2.8). While, in the WASP, a constant field assumption is not longer valid, the inhomogeneity of the magnetic field substantially contributes to the deflections of both species in the broad angular range and has to taken into consideration. The 3D magnetic field distribution is hereby simulated numerically from the geometry of the magnets (CST EM STUDIO, CST GmbH) and was verified by the measurement of actual field distribution using a Hall probe [160]. Later, the trajectories of ions and electrons through the spectrometer are modeled based on the 3D magnetic field where monoenergetic beams of different energies emitted with different angles from a point source are considered. The resultant isoenergy contours on the detectors containing the angular information are used to transfer the 2D spatial information from raw images to the energy angular distributions of both species.

	WASP-MPQ	WASP-Gemini
B $[T]$	0.1-0.24	0.1-0.24
l $[mm]$	200	200
d_{ts} $[mm]$	185	300
d_{sid} $[mm]$	517	\
d_{sed} $[mm]$	15	15
a $[mm]$	0.3	0.4
L_d $[mm]$	287	\

Tab. 3.5 | Summary of utilized TPs used for the experiments in the scope of this thesis. WASP-MPQ is used for experiments in Chap. 5 and Chap. 7. While TP-Gemini configuration is used for experiments in Chap. 6.

Tab. 3.5 summaries the parameters of utilized WASP setup in the scope of this thesis. As an example, the calculated isoenergy curves for ions and electrons corresponding to the WASP-MPQ configuration is shown in Fig. 3.17 (a) and (b). The energy of ions increases towards the zero line (with smaller y). While due to the special orientation of the electron detector plane (xz plane), the energy of electrons decreases towards the zero reference (with smaller z). In such configuration, we obtain an on-axis detectable range for the electrons up to 40 MeV, which is limited by the size of the scintillating phosphor screen for a certain offset d_{sed}. This detectable range can be slightly extended (up to about 50 MeV) by reducing $d_{sed} = 10$ mm but with a price of degraded resolution. Higher energetic electron can be detected by putting a second electron plane in xy plane (see Fig.

3.17 (c)). In this case, a broad detectable range from few MeV to few 100s MeV can be achieved.
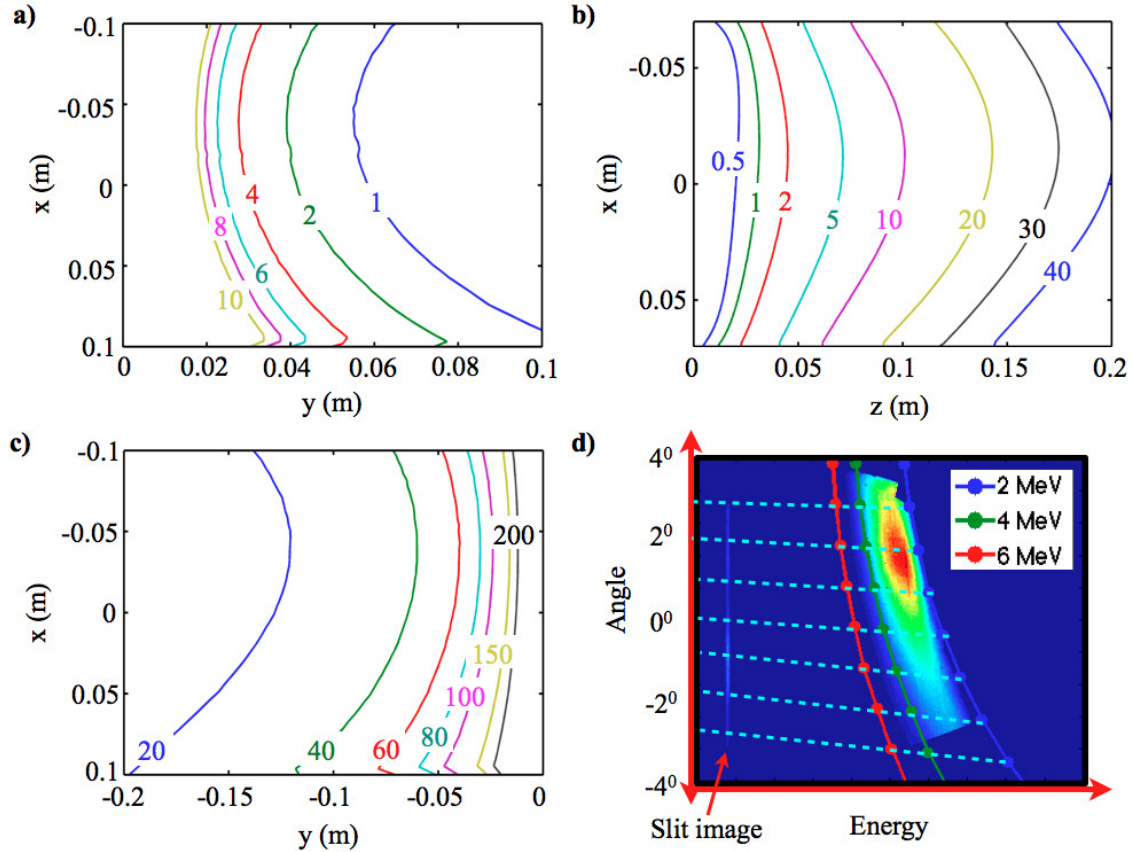

Fig. 3.17 | The calculated isoenergy curves of protons (a) and electrons (b) corresponding to the WASP-MPQ configuration. While (c) shows the corresponding isoenergy curves of electrons of much higher energies when the electron detector is located at the ion detector plane. The energies are given in the unit of MeV. An isoenergy contours of the protons which are superimposed with a raw image containing the measured proton signal and the slit image is shown in (d). Here a Al foil of 45 μm was used, corresponding to a low proton energy cutoff at 2 MeV. The dashed cyan lines indicate different angles with respect to the laser propagation direction.

Owing to the absence of electric field, there is lacking information about multi-species of ions. In case of existence of only two distinct ion species, this issue can be overcame by employing detector stack, for instance, a stacked detector composed of a CR39 in front of a IP. In another way, as presented in experiments in Chap. 5, since proton signals are the major concerning, a layer of thin Al foil of few tens of μm was added in front of the ion detector to block heavy ions and to protect it from direct and scattered laser light. Only protons above certain low energy cutoff by the Al foil are recorded. The image of the entrance slit, *i.e.*, the zero line, and the low energy cutoff line from proton signal allows to extrapolate the average magnetic field for different angles, allowing a double calibration

for the numerical analysis. The measured low energy cutoff lines are compared to the modeled isoenergy curves from the analysis, showing fair agreement. An example is shown in Fig. 3.17 (d).

Chapter 4

A laser-driven nanosecond proton source for radiobiological studies

As mentioned in Sec. 1.2, protons (or more generally ions) can be favorable choices in IBT owing to the superior depth-dose profile (see Fig. 1.2 (a)). However, owing to the high global cost, only a small number of ion beam facilities based on conventional accelerator technology are in use worldwide. The technique is still on a stage of testing the maturity and have not yet been fully established. Laser driven ion acceleration offers a potentially more compact and cost-effective means of delivering ion beams for IBT [83, 189, 190]. This technology gained increasing interest recently, especially since highly energetic proton beams beyond 50 MeV were observed experimentally [10]. However, the laser systems used to obtain these energies were rather large (typically with footprint areas of 100s m^2) with pulse energies of 20-500 J and were limited to single laser shots every 10-20 min. Nowadays, table-top femtosecond lasers with a repetition rate of 10 Hz and pulse energy of several J are available and continuously developing. By using such small and economic lasers, maximum proton energies of up to 40 MeV [31, 191–193] have been achieved. Higher ion energies and more efficient energy conversion from laser photons to ion kinetic energy is predicted with new acceleration mechanisms like radiation pressure acceleration, which involving nm thin targets (see Sec. 2.4).

Currently, the investigations are still in a research stage starting from *in vitro* experiments (i.e., cell irradiation) [194]. As the benchmark, cell irradiation experiments with laser-driven beams [192, 195–197] constitute an important preliminary step to demonstrate the increasing maturity of this technology. In addition, the biological effectiveness of ultrashort-pulsed beams with nanosecond ion bunches of high charge compared to quasi-continuous beams from conventional accelerators can be assessed. In a more general context, time-resolved radiobiological studies with sub-nanosecond particle bunches

might help to elucidate the ultrafast processes underlying the biological response of cells to ion irradiation [198]. In contrast to previous biological experiments with laser-driven beams that either used much broader energy spectra [192, 195, 197] or that had to accumulate 10-20 shots over a few seconds or longer in order to obtain relevant doses above 1Gy [192, 195, 196], in this chapter a method to irradiate cells with truly nanosecond quasi-monoenergetic proton bunches with single shot doses of several Gy driven by a table-top high-power laser is presented. The results are published in [86].

4.1   Experimental setup
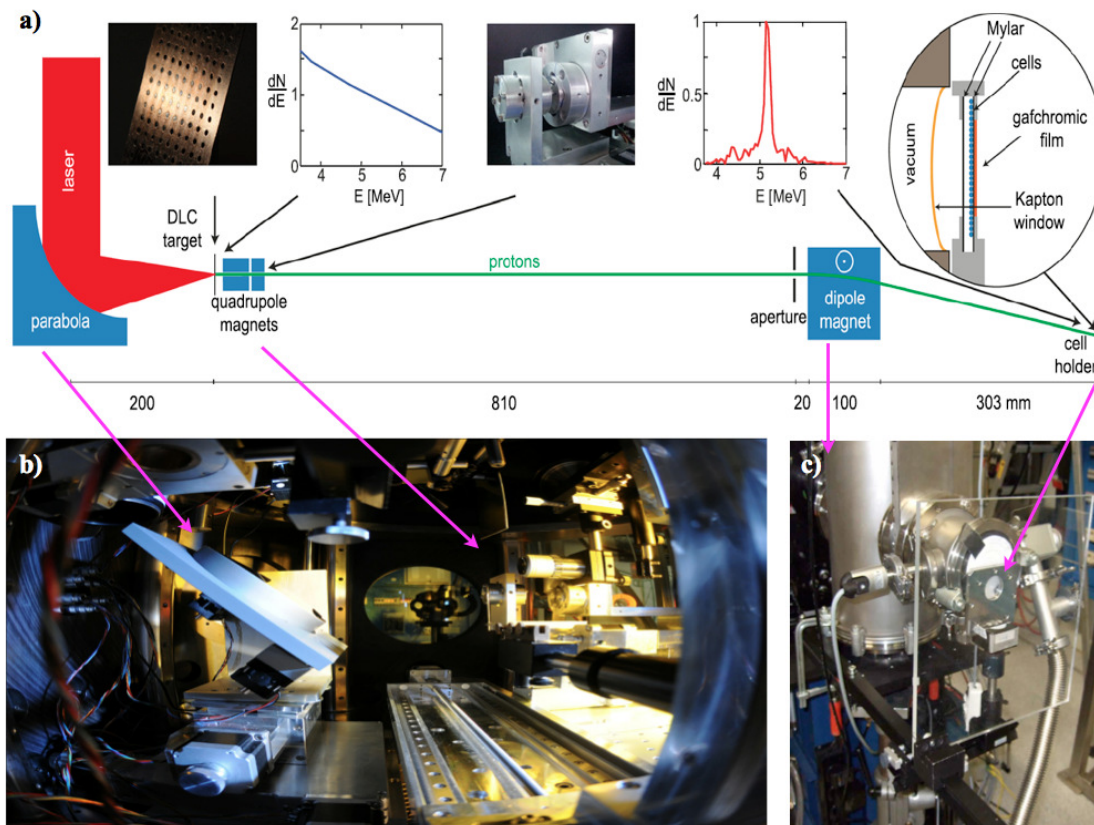
Fig. 4.1 | (a) The schematic picture of the laser driven proton beamline. (b) and (c) shows the actual photography of the experimental setup inside and outside the target chamber, respectively. Protons accelerated from DLC foils are collimated by miniature quadrupoles in a small energy band. The TP-MPQ setup (see Sec. 3.3.2) deflects the beam downwards. Protons exit the vacuum chamber and enter the biological sample. The proton spectra are normalized to 1 for the design energy of 5.2 MeV.

The technical setup of the laser driven proton beamline is shown in Fig. 4.1. The experiments were conducted using the ATLAS laser (for details see Sec. 3.1.1). This

table-top (15 m^2) laser system delivers pulses with a FWHM duration of 30 fs at 795 nm central wavelength. In order to irradiating nm-thin foils, the temporal contrast is enhanced by more than three orders of magnitude by utilizing the DPM setup that is implemented in the laser. A 90° OAP is used to focus the laser pulses with the remaining 0.4 J energy to a measured spot size of 3 μm FWHM diameter, yielding a peak intensity of $8 \times 10^{19} W/cm^2$, slightly lower than $1.2 \times 10^{20} W/cm^2$ for a perfect Gaussian beam. The experiments were performed in single shot mode. DLC foils (c.f. Sec. 3.2.1) with thicknesses of 20 and 40 nm were irradiated under normal incidence. As comparative studies, 5 μm thick titanium foils were irradiated without a plasma mirror (and therefore laser energy of 0.8 J) with p-polarization and an angle of incidence of 45°.
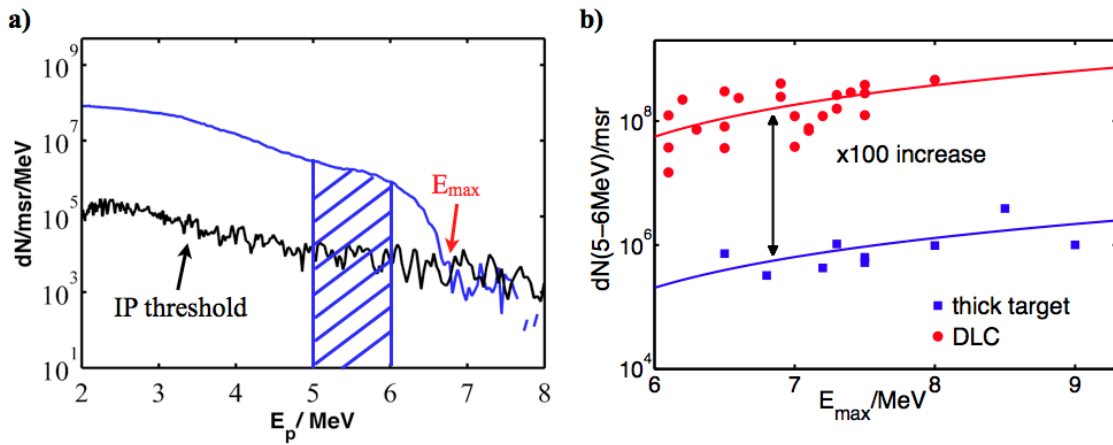

Fig. 4.2 | (a) One exemplary broad spectrum of protons from nm-thin DLC foil. The maximum proton energy E_{max} is defined when the ion signal measured by a IP is comparable to the background noise level, i.e., the IP threshold. The striped blue area indicates the energy regime where the proton number is extracted. (b) Proton numbers per msr for nm-thin DLC targets (red) and 5 μm thick titanium targets (blue) in the energy band 5-6 MeV plotted as a function of E_{max}.

A miniature quadrupole (QP) doublet composed of permanent magnets [199] with an aperture of 5 mm is implemented mounted on motorized stages to focus protons with 5.2 MeV at a distance of 1.2 m. The first QP (with a length of 36.0 mm and field gradient of 433 T/m) was placed 12.4 mm behind the DLC foil and was separated by 7.7 mm to the second QP (with a length of 17.0 mm and a gradient of 505 T/m). The TP-MPQ setup (see Sec. 3.3.2) was used to deflect the proton bunch downwards at a distance of 810 mm away from the target. This setup avoids irradiation of the cell samples by X- or gamma-rays eventually originating from the laser-target interaction. A number of radiation monitors were located outside of the target chamber and recorded such radiation, showing a substantial suppression by more than one order of magnitude compared to thick foil experiments.

By removing the quadrupoles, the setup served as a proton spectrometer allowing optimization of the proton beam to achieve highest energies by varying target thickness and position with respect to best laser focus. The energy distributions of the protons were recorded on an IP detector (c.f. Sec. 3.3.1) behind the dipole magnet. The typically broad spectrum extends from energies below 1 MeV to a certain maximum energy E_{max} with decaying flux at higher energies, as shown in Fig. 4.1 (a) and Fig. 4.2 (a). A hundred-fold higher proton fluence is obtained with 0.4 J laser energy compared to standard TNSA (c.f. Sec. 2.4.1) where 5 μm thick titanium foils and twice the laser energy were used. The maximum proton energy E_{max} remains similar in both cases. However, the number of protons accelerated to energies between 5 and 6 MeV in a solid angle of 1 msr, which can be easily transported with our quadrupole setup, is significantly increased by a factor of 100 (see Fig. 4.2 (b)).

After the quadrupoles were inserted again, the setup produced an elliptical focus in the plane of the cells (1230 mm away from the target) with half axes of 0.45 mm and 5.2 mm at 50 % of the maximum dose (see Fig. 4.3 (a)) rotated by 40° with respect to the horizontal plane. The dose distribution was measured using self-developing RCF (Gafchromic EBT2, see Sec. 3.3.1). The functionality of the complete setup was tested at the MLL Tandem accelerator prior to implementation in the proton beamline with a continuous beam of 9.8 MeV protons.
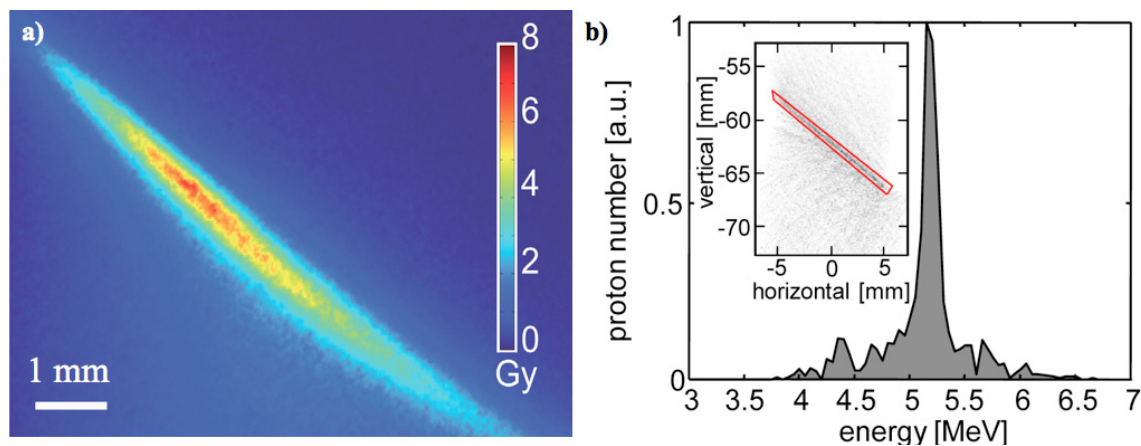
Fig. 4.3 | (a) Elliptical dose distribution at the position of the cell sample measured with RCF. Here the maximum dose obtained in a single laser shot was 7.1 Gy. (b) Simulated spectral (main graph) and spatial (inset) distribution of protons in vacuum at the same position. The spectrum is formed by all protons within the red polygonal region.

The imaging properties of the complete setup including the quadrupoles, TP-MPQ setup were calculated via a Monte-Carlo simulation. Starting from a point source with stochastically varying angle of emission, 4×10^5 protons with energies between 3 and 7 MeV are traced through the complete setup. To produce a 2D distribution that can be

compared to the one measured by the IP detectors or RCF, the protons that reach the plane where cells are positioned are binned into 100 μm large pixels. In the simulated image, all points within the red polygonal region, corresponding to the measured high-dose spot, are used to calculate the energy distribution, yielding a narrow spectrum with central energy of 5.2 MeV and with an energy spread of dE/E=6%, as shown in Fig. 4.3 (b). A cross check was done by a range measurement using a stack of Aluminum cover foils with varying thickness that covered the region on the detector where the line focus was visible. The result was well inline with the resultant deflection in the TP-MPQ setup (deviation of 62 mm away from central axis at the exit window). Due to the narrow energy band, the initially broad energy distribution which may vary from shot to shot has little effect on the result.

Hence, owing to the chromaticity of the quadrupoles, the initially broad energy distribution measured without the quadrupoles narrows over propagation as depicted by normalized spectra at different positions in Fig. 4.1 (a) and Fig. 4.3 (b). At the plane of the cells, half the protons are contained within a band of 0.3 MeV. This results in a difference in time of flight of 1 ns, which determines the proton bunch duration as it is much longer than the 30 fs laser pulse. Under best conditions, a maximum proton fluence of 5.1×10^6 mm^{-2} (mean fluence over the area of the line focus within 50% of maximum dose: 3.3×10^6 mm^{-2}) was achieved in a single shot, which corresponds to a maximum (mean) dose of 7.1 Gy (4.6 Gy) at the position of the cells. The maximum dose amounts to a peak dose rate of 7×10^9 Gy/s over an interval of 1 ns.

To irradiate living cells in radiobiological experiments, the proton bunch leaves the vacuum through a 50 μm thick Kapton window and enters a self-developed cell holder [200]. The Kapton foil is able to completely shield a potential contribution of low-energy carbon ions which - if present in the primary beam at all - would be focused to the same point as 5.2 MeV protons depending on their charge and energy (e.g., C^{6+} ions with 1.3 MeV/u). The cell container was positioned as close as possible to the exit flange of the vacuum chamber, leaving ~5 mm of air between the Kapton exit window and the front side (c.f. Fig. 3.14). As shown in Fig. 4.1 (a), it is composed of a sealable, stainless steel housing with two windows (front and back) formed by two Mylar foils (6 μm thickness each, at a distance of 3 mm).

Monolayers of human cervical cancer cells (HeLa) were seeded ~48 h prior to irradiation directly on the back Mylar foil of the cell containers in 10 ml RMPI 1640 medium without phenol-red (PAA Laboratories, Cölbe, Germany). Medium were supplemented with 10% FCS, 25 mM HEPES (4-(2-hydroxyethyl)-1-piperazineethanesulfonic acid), 100 U/ml penicillin, and 50 μg/ml streptomycin. Cell containers were kept in a CO_2-incubator at 37^oC and maintained in a horizontal position up until ~5 min prior to

irradiation (last 30 min without CO_2 control). If brought upright, the medium will collect at the bottom, leaving the cells in an atmosphere saturated with water vapor. Appropriate control samples were treated under the same conditions including bringing the cell containers in a vertical position as for irradiation. On the outside of the back Mylar foil, a microstructured square grid (area 10×10 mm^2, spacing of grid lines 150 μm) and coordinate system (letter pairs every 300 μm) visible in microscopic images allows for localization and identification of cells. The HeLa cell monolayer covered the full area of the grid on the Mylar foil and was exposed to protons generated in a single shot (mean energy at the position of the cells: 4.45 MeV), while the dose distribution was measured by the RCF placed immediately attached to the outside of the cell container in contact to the foil containing the cells ~1-2 h before irradiation. By means of the microstructured grid on the cell holder and predefined marks on the film, the dose distribution can be spatially registered to microscopic images of the cells (see Fig. 4.4). Customized image processing tools in MATLAB (The MathWorks, Inc.) allowed a registration with a spatial uncertainty of ±1 pixel of the scanned film (21 μm).
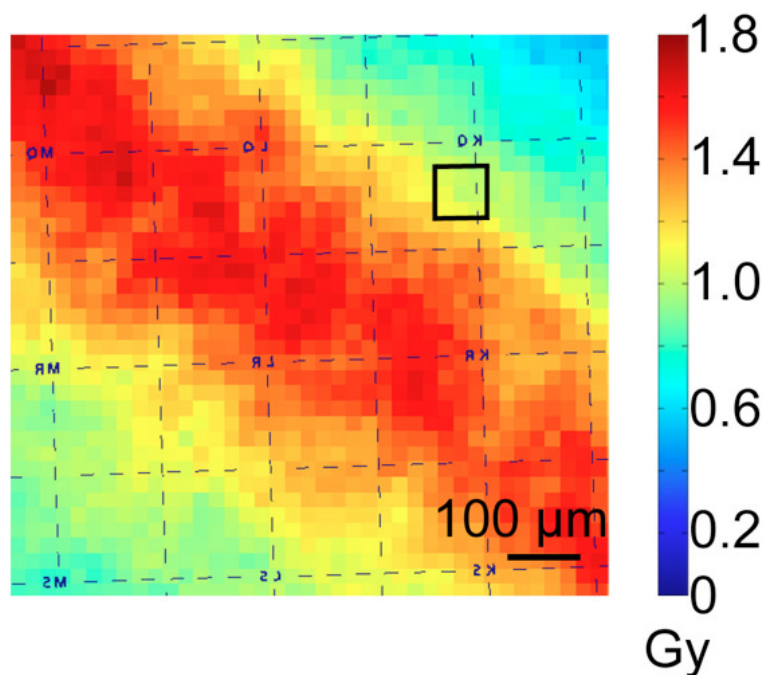

Fig. 4.4 | Registration of the dose distribution measured by RCF with the microstructured grid on the Mylar foil holding the cells. The black square indicates the exact location of the region of interest shown in Fig. 4.5 (a).
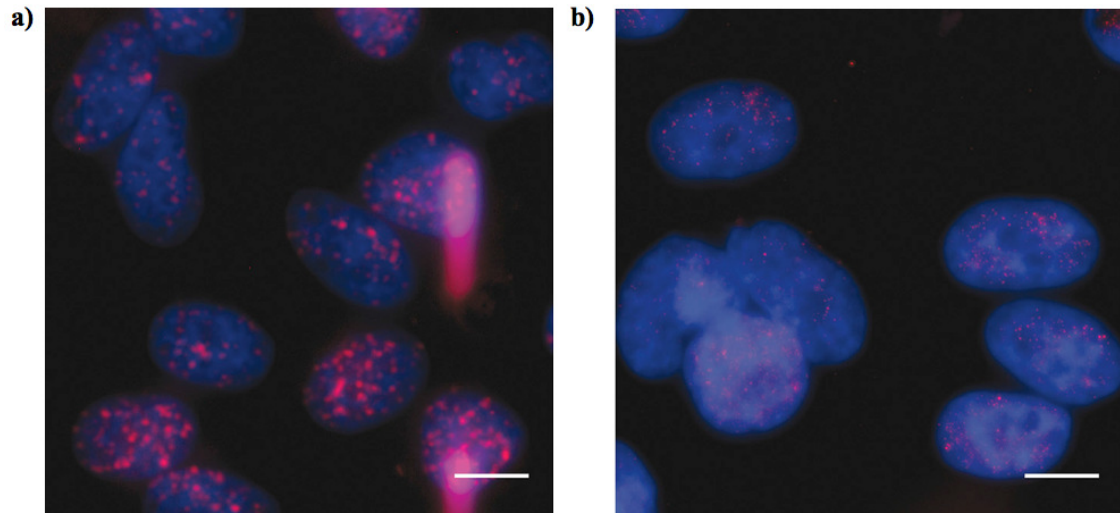
4.2 Radiobiological studies

Fig. 4.5 | Initial DNA damage in HeLa cells. (a) Sample exposed to a mean dose of 1.0 Gy and (b) corresponding unirradiated control. Foci of γ-H2AX (red) and cell nuclei (blue) are shown (3D microscopy, maximum intensity projections, background correction, contrast enhanced). The red vertical bars in (a) are part of the grid used for spatial registration (see Fig. 4.4). Horizontal scale bars, 10 μm.

After exposure to laser-driven protons, the cells were incubated at $37^{o}C$ (without CO_2 control) for 30 min prior to fixation and immunostaining. The biological response in terms of initial damage to the deoxyribonucleic acid (DNA) was quantified using the γ-H2AX assay. Double-strand breaks in the DNA are followed by a rapid phosphorylation of the histone H2AX, leading to a local concentration of the phosphorylated form (γ-H2AX) at the damaged site. The primary antibody used was mouse-anti-γ-H2AX (1:350; Upstate, Charlottesville, VA, USA) and the secondary antibody sheep-anti-mouse-Cy3 (1:500; Jackson ImmunoResearch, West Grove, PA, USA). Nuclei were stained with DAPI in blue. The samples were covered with a cover glass, extracted from the cell container, transferred to an object slide and sealed with nail polish. Images were acquired using an inverted epifluorescence sectioning microscope (Zeiss AxioObserver Z1), a Zeiss LCI Plan Neofluar 63x objective with 1.3 numerical aperture and a Zeiss AxioCam MRm camera resulting in a pixel size of $0.102 \times 0.102 \ \mu m^2$. The Cy3 and DAPI digital images were captured serially. Z-stacks with at least 10 slices per stack ($\sim$10-40 cells per stack) were taken at various positions from each sample. Since this assay works best for doses below 2 Gy (otherwise the number of foci becomes too large to differentiate and count them individually), biological results are presented here for a cell sample exposed to a maximum dose of 1.7 Gy in a single shot. Fig. 4.5 (a) shows some of the cells of this

sample (exposed with a mean dose of 1.0 Gy across the depicted region (see Fig. 4.4), along with an unirradiated control sample (Fig. 4.5 (b)). The bright red spots are foci of γ-H2AX visualized with specific antibodies labeled with a fluorescent dye.
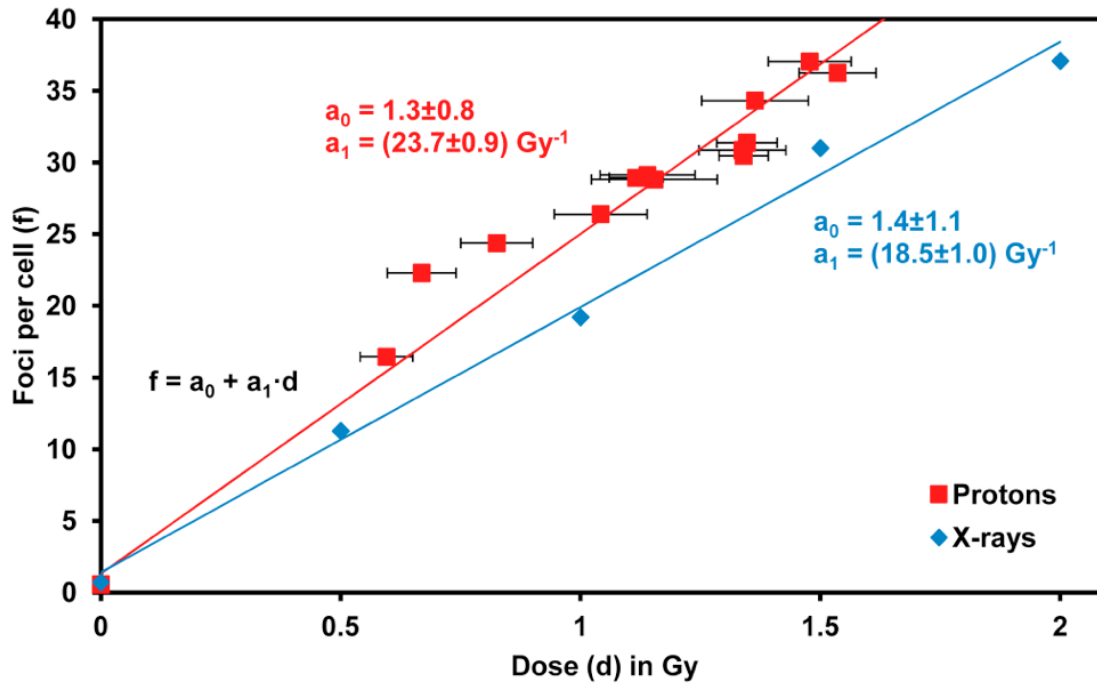

Fig. 4.6 | Mean number of γ-H2AX foci per cell as a function of dose for laser-driven protons and 200 kV X-rays. Each data point for protons contains 20 cells. Error bars in dose show the dose inhomogeneity (standard deviation) across the regions of interest used for evaluation.

The inhomogeneous dose distribution across the line focus in combination with the precise spatial registration of the delivered dose and the position of each cell allowed us to obtain full dose response curves for each irradiated sample in a single shot. Data were analyzed using ImageJ (ImageJ, NIH) with a custom semiautomatic software macro FociCount [201]. The original stacks were subjected to background correction with a rolling ball algorithm (ball size 200). Nuclear boundaries and foci were automatically identified on maximum intensity projections by a threshold algorithm and the number of cells as well as the total number of foci was determined. Minimum foci size (area) of 5 pixels (0.05 μm^2) and maximum foci size of 200 pixels (2.08 μm^2) were selected. An example is shown in Fig. 4.6, where the mean number of foci per cell is plotted against the mean dose for various regions of interest (142 $\times$ 106 μm^2) across the area of the line focus. Each data point is the mean over 20 cells (total: 273 cells from the same sample). Horizontal error bars show the standard deviation of the dose values within each region (as a measure of the inevitable dose inhomogeneity due to the steep dose gradients). The

uncertainty of ±1 pixel in the image registration leads to an additional uncertainty of ±4% in the mean dose value.

Fig. 4.6 also gives a photon reference curve taken for the same cell line with 200 kV X-rays and linear fits to the data using a least squares fit method where each data point was weighted with the corresponding number of cells [202] . Here, to acquire an X-ray reference curve, cells treated in the same way were exposed to doses of 0, 0.5, 1.0, 1.5 and 2.0 Gy (dose uncertainty: 5%) of 200 kV X-rays using the RS225 device (Gulmay Medical, Surrey, United Kingdom) with a dose rate of 0.88 Gy/min (15 mA, 0.5 mm Cu filter) and a source-cell distance of 50 cm using a field of 20×20 cm^2 at Klinikum rechts der Isar and evaluated accordingly (>150 cells per data point, 1000 cells in total). The slopes are 23.7 ± 0.9 foci per cell per Gy for protons and 18.5 ± 1.0 for X-rays. In both cases, sham-irradiated control samples showed only a low number of foci (on average 0.7 foci per cell). At an effect of 30 foci per cell (corresponding to an X-ray dose of 1.5 Gy), the relative biological effectiveness (RBE, defined as the ratio of X-ray dose and proton dose required to yield the same biological effect) for the induction of repair foci turned out to be 1.3 ± 0.3. The error estimate was determined by Gaussian error propagation of the uncertainties of the X-ray dose and proton dose values required for 30 foci per cell (X-ray dose uncertainty: ±10% according to the uncertainties in the fit parameters (Fig. 4.6) and ±5% in absolute dosimetry (systematic); proton dose uncertainty: ±9% according to the uncertainties in the fit parameters, ±4% for image registration (61 pixel), and ±20% in absolute dosimetry (systematic) including film calibration). This relatively large error is acceptable for a proof-of-principle experiment and will be reduced in subsequent experiments, mainly by improving the absolute proton dosimetry in the few MeV energy range.

The preliminary RBE obtained in the experiments is in agreement with proton RBE values in conventional beams at comparable proton energies [203] although measured for different biological endpoints. This indicates that no new radiobiological effects are to be expected for the distinctive combination of nanosecond proton delivery and single bunch dose rates of 10^9-10^{10} Gy/s as realized by the single bunch irradiation prototype setup, even though it could equally be used for accumulated multi-bunch irradiations. This finding is in line with previous studies in single, nanosecond proton bunches at conventional sources [204, 205] and single or multiple ns bunches of laser driven protons [196, 197]. This confirms that for future applications in radiotherapy, where bunches of at least ns length (due to the propagation along an inevitable beamline of at least one meter between target and patient) and a maximum dose of a few Gy per shot will be applied, the same RBE as for conventional sources can be assumed.

4.3   Summary

In summary, as the first benchmark, the potential of small, high repetition rate lasers for generating high proton yield, a nearly monoenergetic spectrum, and a reduction of background radiation (X- and gamma rays) is demonstrated by combining nanometer thin targets and proton beam optics. This method allows analyzing the full dose response to the nanosecond proton bunch attributed to a single laser pulse, enabling precise radiological experiments even in the presence of significant shot-to-shot fluctuations. This novel approach is the most important point of the presented study here. It qualitatively confirms for future medical application the applicability of laser driven ion bunch with ns duration and high pulse dose of few Gy. Moreover, by reducing the size of our setup further, proton bunches of sub-ns durations will be accessible for fundamental biological research in the low ion energy range of a few MeV. Although many issues still remain to be solved, most importantly the progress towards higher ion energies beyond 100 MeV per nucleon, the demonstration of the feasibility of a very compact laser-driven beamline for proton acceleration, transport and delivery strongly bolster future medical applications. As the next step, the prototype system will be adapted to the studies of sub-ns biological response and *in vivo* experiments (i.e., animal irradiation) at the prospect of the new ungraded ATLAS system (300TW, 6J, 20fs).

The key to success in this method is the achieving of the hundred-fold higher proton fluence by utilizing nm-thin foils as compared to *μm* thick targets. This finding motivates in-depth investigation on the underlying physics. Thus, in the next chapter, the fundamental physics resulting in the high fluence from nm-thin foil is investigated.

Chapter 5

Ultrasmall divergence of laser-driven ion beams from nanometer thick foils

The short time scale on which laser-driven ion acceleration occurs along with the small source size enable extremely high ion densities in the MeV bunches which could be superior for specific applications (see Sec. 1.2). However, such high density is only maintained close to the source, it drops quickly due to typical angular spread of few tens of degrees [13, 14, 76]. Such large angles lead to large losses using magnetic quadrupoles [199], complicate the beam transport and therefore trigger investigations on sophisticated transportation schemes such as pulsed solenoid[206] and laser driven micro lenses [28]. Meanwhile, shaped lens target [207], droplets [208] and curved target [72] have been used to manipulate the ions angular distribution. Those approaches were mostly based on TNSA mechanism (c.f. Sec. 2.4.1) with μm thick targets. Acceleration fields are built at the target rear by the hot electrons generated at the front side of the targets. The divergence of the ions strongly depends on the electron density and phase space distribution of the electrons behind the target, which is initially related to the laser profile and then disturbed during the transportation through the targets [209, 210].

The recent improvement on the laser temporal contrast allows the experimental investigation with ultra thin foils with thickness down to nm scale. As mentioned in Sec. 1.1, the maximum energy benefits from nm-thin foils [33–37], although based on different acceleration mechanisms at play (c.f. Sec. 2.4). Moreover, the experimental fundings imply that thinner foils can generate much more collimated ion emission as compared to μm thick targets [33, 38].

In this chapter, the first detailed study on the divergence of proton beams accelerated from 5-20 nm thick DLC foils (see Sec. 3.2.1) is presented. Divergences as low as 2° were observed for different foil thickness and irradiation conditions. In comparison with μm

thick targets, more than 10 times reduction in the divergence is observed. Moreover, the proton beams show a pronounced collimation over the whole energy range. Similar features are reproduced in 2D PIC simulations with parameters representing our experiments, suggesting that the small divergence is the result of a steep longitudinal electron density gradient that seems representative for nm thin foils. The high directionality is attributed to a transverse electron density distribution with similar function as in longitudinal. To explain the experimental observation, a simple analytical model is given, consisting with the simulation results. The results are published in [87].
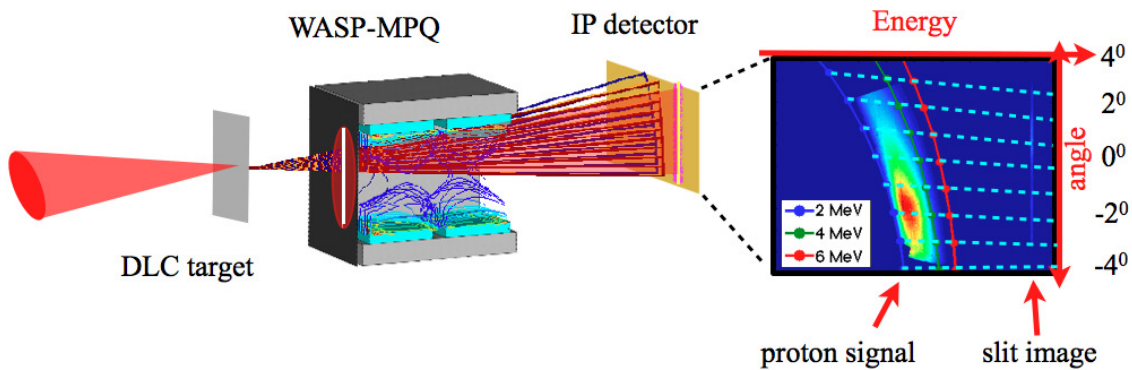
5.1   Experimental setup

Fig. 5.1 | Experimental setup. The divergence of protons characterized with the WASP-MPQ setup and IP detector (c.f. Sec. 3.3.1). The trajectory of protons through the magnetic field as well as the magnetic field structure was overlapped with the actual setup photograph. The resulted isoenergy contours of the WASP-MPQ setup superimposed with a raw image of proton energy-angular distribution is shown at the IP position. The raw image is obtained with a 10 nm target displaced by $100\,\mu$m from the laser focal plane, which is the identical image in Fig. 3.17 (d).

The experimental setup is shown in Fig. 5.1. The experiments were performed with the ATLAS laser system (see Sec. 3.1.1), providing an optimum laser focal spot with peak intensity of $8 \times 10^{19} W/cm^2$ and with energy of 400 mJ by using the DPM system. DLC foils (c.f. Sec. 3.2.1) of thickness 5, 10 and 20 nm have been irradiated under normal incidence for varying spot size, the actual spot size on target in the range of 3-19.2 μm has been adjusted by moving the target along the laser axis. The WASP-MPQ setup is used to determine the angularly-resolved energy distribution of protons. Details of this spectrometer are described in Sec. 3.3.2. A Layer of 45 μm Al foil was added in front of the IP to block heavy ions and to protect IP from direct and scattered laser light, allowing detection of protons with energies beyond 2 MeV. Exponentially decaying proton

energy distributions with cut-off energy between 3 and 6 MeV are observed throughout the experimental campaign.
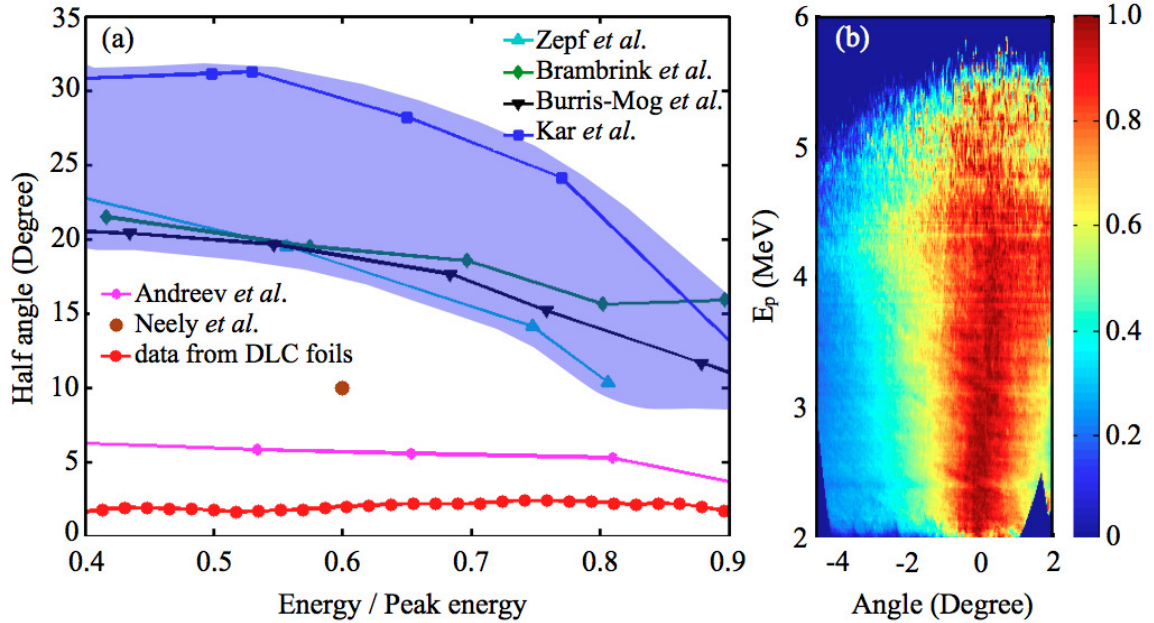
5.2 Experimental results

Fig. 5.2 | (a) Beam divergence (half angle) plotted as a function of proton energy that normalized to the maximum energy for the most collimated beam from DLC foils (red curve), along with other data published in the literature from μm thick targets (the light blue area, presented by blue, green, black and cyan curves) [13, 14, 76, 206] and from nm scale thin targets (brown dot and magenta curve) [33, 38]. (b) Experimentally processed result of the data presented in Fig. 5.2 (a) after normalization, where the color scale denotes the normalized fluence for given energy.

The smallest divergence was observed with a 10 nm target displaced by 100 μm from the laser focal plane. The corresponding raw image is shown in Fig. 5.1. In order to highlight the collimation over the complete energy range, the extracted energy-angular distribution of this example is normalized and shown in Fig. 5.2 (b). Interestingly, the divergence is almost constant over the whole detectable energy range, resembling a well-collimated feature. By fitting a Gaussian function to the angular distritbuion for each individual energy value, the divergence θ is thus defined by the half value of FWHM of the fitting profile. Fig. 5.2 (a) shows the divergence plotted as a function of normalized proton energy, allowing a comparison to established results [13, 14, 76, 206] which are represented in Fig. 5.2 (a) as well. Compared to μm thick targets, the half angle from 10 nm foil is reduced by a factor of 10. Moreover, the typical increasing of divergence with decreasing energy is not observed. The results from experiment with 50 nm [33] and

800 nm foils [38] are included as well, indicating an overall reduction of divergence with decreasing target thickness.
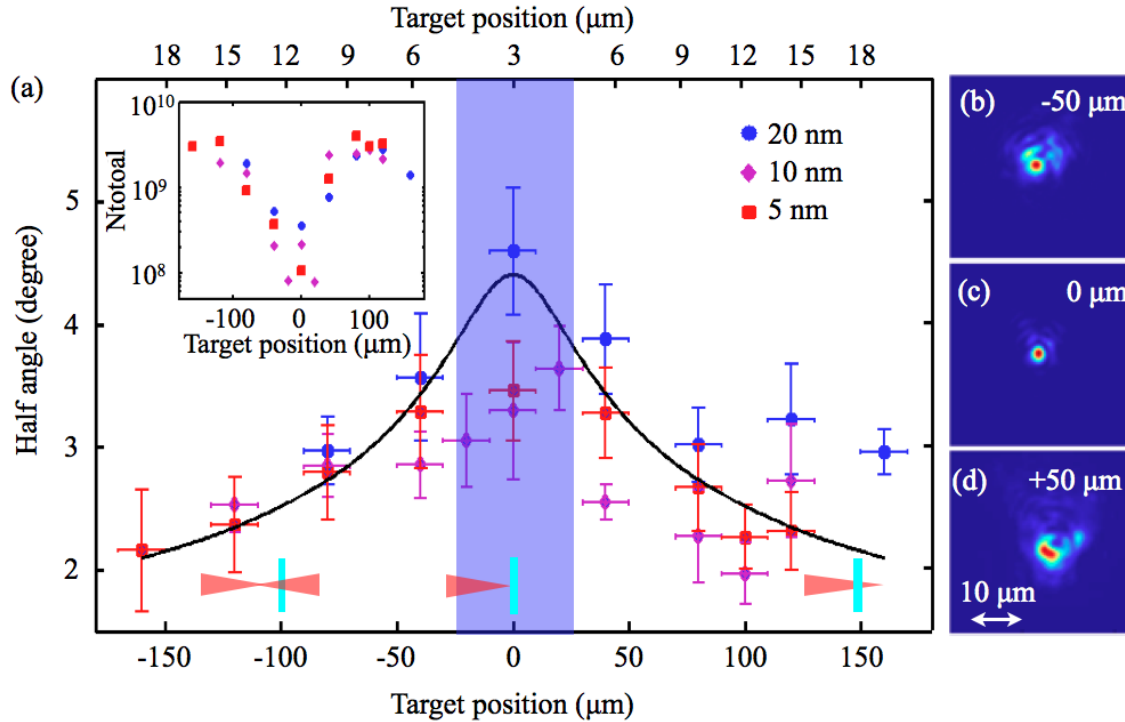

Fig. 5.3 | (a) Avaraged beam divergence (half angle) for varying thickness of DLC foils and target positions. The lower axis shows the target position, where +/- means the foils were placed before/after laser focal plane, as indicated by the small pictures. While the upper axis denotes the focal spot FWHM diameter D_L. The black curve is an empirical fitting curve showing the divergence scale with laser FWHM diameter $(D_L)^{-1/2}$. The inset presents the total number of protons for each shot. The Measured laser intensity distribution is shown at three target positions -50 μm (b), 0 μm (c) and 50 μm (d).

Further on, the thickness of the targets and their positions with respect to the focal plane of the laser were varied. As shown above, the divergence showed no noticeable dependence on energy. Therefore, we plotted the average value of the half angle as a function of the target position in Fig. 5.3 (a), the vertical error bar indicates the standard deviation for each shot while the horizontal error bar shows the positioning accuracy of about 10 μm, smaller than the Rayleigh length of 25 μm marked by the light blue area. The small divergence combined with the well-collimation feature are conserved during the whole parameter scan. The obtained divergences varied in the range of 2-4.6°, showing comparably small values. The divergence is maximized with a value of 4.6° in the focus plane for the thickest foil of 20 nm. For thinner foils (5 and 10 nm), these values are reduced to 3.3°, indicating a tendency of reducing divergence with decreasing of target thickness even in the nm scale.
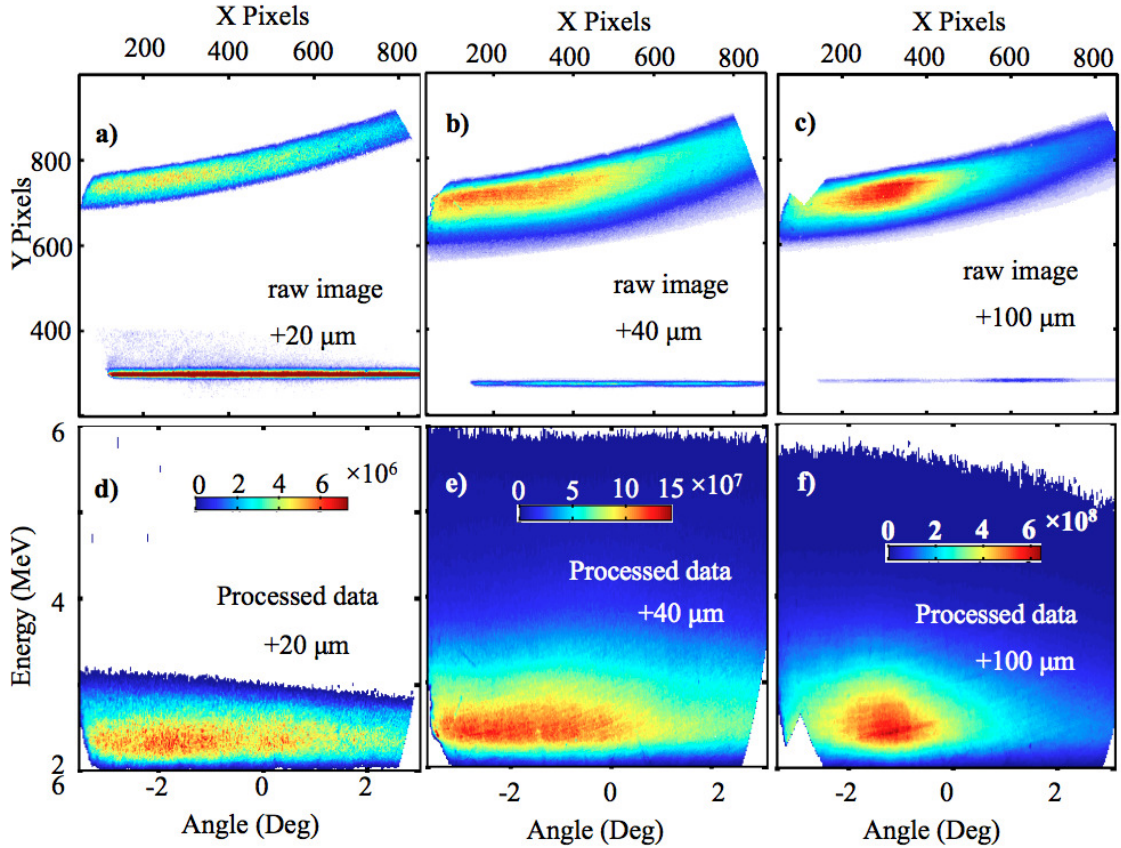
Fig. 5.4 | Measured raw images of beam divergence with 10 nm DLC foils for three different target positions 20 μm (a), 40 μm (b), and 100 μm (c), respectively. (d) - (f), the corresponding processed results from the raw images (same parameters as in (a) - (c)).

Moreover, the divergence of the protons can be further optimized by adjusting the focal spot size. Fig. 5.4 shows a series of raw images as well as the processed results of beam divergence obtained from 10 nm DLC foils at three different target positions. Clearly, the divergence decreases with increasing focal spot size on the target when moving the target out of focal plane beyond the Rayleigh length and indeed happened for both sides (c.f. Fig. 5.3 (a)). The smallest divergence was obtained in the target position of +100 μm, which is our example of Fig. 5.2.

Besides, the laser intensity distribution is single-peaked as shown for three exemplary positions in Fig. 5.3 (b), (c) and (d), which allows us defining a FWHM diameter D_L of the laser focal spot by fitting a Gaussian function. The measured D_L indeed scales as the classical prediction $D_L = D_{L0} \sqrt{1 + (z/z_R)^2}$ for different target positions with small deviation of $< 5\%$. Here D_{L0} is the minimum FWHM diameter, z is the target position and z_R is the Rayleigh length. An empirical scaling is found, showing that the divergence roughly scales with the laser FWHM diameter $(D_L)^{-1/2}$. Note that the maximum energy of protons is little influenced by the change of target position and varied between 3 and

6 MeV with the highest values preferably attained at $\pm$ 100 μm (see Chap. 7), which is the same position for minimum divergence. In addition, the measured total number of protons above 2 MeV is extracted from the measured proton spectrum and corresponding divergence from the parameter scan, as shown in the inset of Fig. 5.3(a). Interestingly, it increases when enlarging the target positions, i.e. when the divergence reduces.

5.3   PIC simulations

To get further qualitative insight, 2D PIC simulation were performed with the KLAP code [135]. Solid density ($n_0 = 350 n_c$) plasma slab was considered. The initial temperature of electrons is 1 keV. The simulation box is 60 λ in laser direction (x) and 20 λ in transverse direction (y) in 2D with a resolution of 200 cells/λ and 40 cells/λ, respectively. Each cell is filled with 400 quasiparticles. The spatial resolution and particle number are set to get sufficient resolution with a reasonable computational cost. A linearly polarized laser pulse with a Gaussian envelope in both the spatial and temporal distribution with a FWHM diameter D_L of 3 μm and a FWHM duration of 33 fs, is used to approximate the experiment conditions.
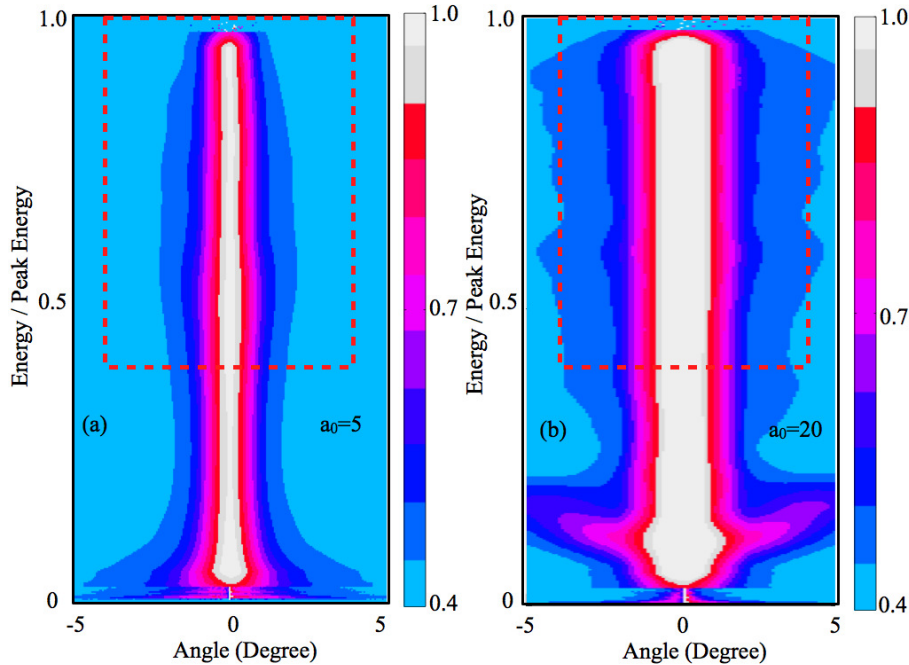

Fig. 5.5 | Simulation results for proton angular distribution at $t = 100T$ after normalization with $a_0 = 5$ (a) and $a_0 = 20$ (b). Here T corresponds to one laser cycle, the red rectangles mark the experimental observation window. The targets are irradiated with the laser at the best focal position. The same color scale is used in both graph.

Fig. 5.5 (a) shows the 2D simulation result of the energy-angular distribution of proton from a 40 nm foil with $a_0 = 5$ at the best focus position after normalization, proceeding in the same way as the experimental data. A well collimated proton beam is observed with a constant value of about 2° over the whole energy range, showing almost identical behaviors as the experimental observation (c.f. Fig. 5.2 (b)). Further simulation was carried out with identical parameters except for a large $a_0 = 20$ as compared to our experimental condition with $a_0 = 5$. The simulation result is shown in Fig. 5.5 (b). A larger divergence with a half angle value of about 4° is observed from simulation, which is a factor of two increase as compared with the simulated results with $a_0 = 5$ (see Fig. 5.5 (a)). Still, the proton beam exhibits a well collimated feature under higher intensity. Those interesting features, the small divergence and the well collimation, seem representative for nm ultrathin foils in a larger range of variation on laser intensity.

As discussed in Sec. 2.4, different mechanisms can be responsible for ion acceleration from nm thin foils. For the experimental parameters here, most likely a number of these mechanism coexist [211]. However, regardless of these different mechanisms, in a very simple picture, the divergence depends on the electric field direction during the acceleration phase. In turn, the electric field depends on the electron density distribution at a given time.

The corresponding electron density distributions are shown in Fig. 5.6. In Fig. 5.6 (a) the longitudinal electron density distributions for the cases $a_0 = 5$ and $a_0 = 20$ at $t = 30T$ (when the laser pulse has just left the target) from our simulations are presented. They are well represented by an exponential distribution with the longitudinal density scale length l_0 of $1/12$ μm and $1/7$ μm, respectively. Interestingly, both values are much smaller than the typical values of few μm for μm thick targets [212–214]. And l_0 increases roughly by a factor of 2 owing to the higher electron temperature under higher laser intensity, consistent with the increase in the divergence of protons (see Fig. 5.5).

5.4 Analytical model

Our results can be described by a simple self-developed quasi-stationary electrostatic analytical model. Substituting a Boltzmann distribution of the hot electrons into Eq. 2.2, the electric field strengths read as

$$
\begin{aligned}
E_y &\propto -\frac{k_B T_e}{e}\frac{\partial n_e}{\partial y} \\
E_z &\propto -\frac{k_B T_e}{e}\frac{\partial n_e}{\partial z}
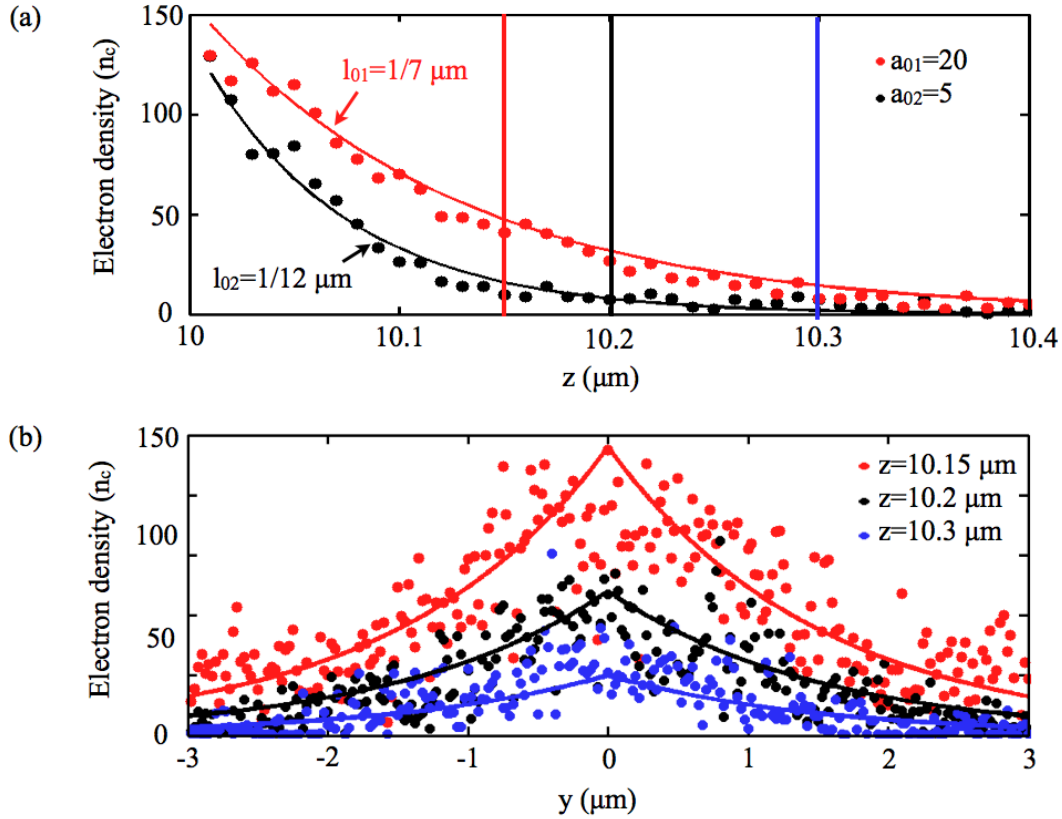\end{aligned}
\tag{5.1}
$$

Fig. 5.6 | (a) Longitudinal electron density distribution (z axis) at $y = 0$ at $t = 30T$ with laser intensities $a_{01} = 20$ (red) and $a_{02} = 5$ (black), respectively. The targets were initially located at $z = 10\ \mu$m. The dots denote the simulated results while the curves are the fitting functions. (b) Transverse electron density distribution (y axis) at three different z positions with $a_{02} = 5$ (as denoted by different color lines in (a)). The transverse density profiles are fitted by an exponential function with a scale length $l_y = 1.5\mu$m.

where n_e is the electron density, y and z are the transversal and the longitudinal dimension, respectively.

Defining local electric field direction as $\alpha = E_y/E_z$, one derives the emission angle of protons θ as

$$\theta = \arctan(\int_0^\infty \alpha E_z dt / \int_0^\infty E_z dt) \approx \arctan < \alpha >$$
$$= \arctan < \frac{\partial n_e}{\partial y} / \frac{\partial n_e}{\partial z} >,$$

(5.2)

where the angle bracket denotes the average along the ion trajectory. Importantly, this equation shows how the divergence relies on the electron density distribution.

Assuming a reasonable electron density distribution $n_e = n_0 \cdot \xi(y) \cdot exp[-\frac{z}{l_0}]$ with a transverse profile $\xi(y)$ and a longitudinal exponential distribution in Eq. 5.2, where n_0 is a constant denoting the electron density, one derives

$$\theta = \arctan < -\frac{\frac{\partial \xi(y)}{\partial y}}{\xi(y)} \cdot l_0 > \tag{5.3}$$

Obviously, the larger the longitudinal density gradient (i.e., the smaller the scale length l_0), the smaller the angle of divergence θ. Indeed, it is this steep longitudinal electron density gradient shown in the simulations (see Fig. 5.5) which tears the acceleration field forward, i.e., reduces the divergence with deceasing target thickness from μm to nm.

The reduction of scale length l_0 in the case of nm foils can be understood by the following simple picture. As mentioned in Sec. 2.4.1, l_0 is given by the local Debye length λ_D (c.f. Eq. 2.22). For a given electron mean energy $k_B T_e$, l_0 is inversely proportional to the square root of the electron density n_0. In the case of μm thick targets, due to the large angular spread of few 10s of degrees for hot electrons inside the target [215], n_0 drops significantly at the target rear, resulting in a typical l_0 of few μm [212–214]. When the target thickness is reduced from tens of μm to submicrometer, the influence from electron propagation through the target is suppressed and the angular spread of hot electrons is substantially reduced, altogether resulting in a higher n_0. Moreover, with the reduction of thickness, the recirculation of the hot electrons is enhanced [31], which can further increase n_0. Those arguments imply that a small l_0 exists at the rear side of thinner targets, which in turn resulting in a small divergence of ions.

Since the divergence is strongly depend on l_0, l_0 would increase when the hot electron temperature is higher. Higher electron temperature is typical for higher laser intensity, consistent with the PIC simulation results (see Fig. 5.5). Such observation indicates the divergence depends only weakly on the laser intensity with other parameters unchanged, i.e., $\theta \propto (I_0)^{1/4}$. This suggests that for future applications the influence of large laser systems on the divergence of ions should be taken into account, which from the perspective of small divergence would be counterproductive.

Furthermore, Eq. 5.2 does not only highlight the importance of longitudinal electron density distribution, but also predicts the influence of transverse electron density on the divergence of ions, similar to [209, 210]. In the following, Eq. 5.2 is used to describe the influence of transverse electron density on the divergence of ions at different parameters.

μm **thick targets**

In previous experiments, the transverse electron density was found to be well approximated by a bell shape profile $\xi(y) \propto exp(-4\ln 2\frac{y^2}{D^2})$ for μm thick target [56]. Noted that typically the FWHM diameter of the transverse Gaussian profile D is much bigger than the FWHM diameter of laser focal spot D_L due to the propagation through μm target with large angular spread (c.f. Eq. 2.52). In this case Eq. (5.2) reads as

$$\theta \propto \arctan < 8\ln 2\frac{y}{D^2} \cdot l_0 > \tag{5.4}$$

θ monotonically increases with transverse distance from the center as denoted by y. Since the high acceleration field appears in the centre, the high-energy ions originate from small y. This implies a reduction of divergence with increasing energy, consistent with [13, 14, 76, 206].

nm thin targets

Regarding Eq. (5.2), the collimation feature observed in our experiments can be explained by an exponentially decaying transverse density distribution $\xi(y) \propto exp[-\frac{|y|}{l_y}]$, where l_y is the transverse density scale length. With such a given transverse profile, a constant value of divergence θ, independent on the energy and the trajectory of ions, is given by

$$\theta \propto \arctan(l_0/l_y) \tag{5.5}$$

As one can see from Fig. 5.6 (b) where the transverse electron density profiles at three different z positions behind a 20 nm foil are shown, the results from PIC results are not contradicting this hypothesis. Indeed, the profiles are found to be well represented by an exponentially decaying profile with a scale length l_y, similar to the radius of laser spot $D_L/2$ of approximately 1.5 μm. Substituting l_0 and l_y obtained from simulations into Eq. (5.5), a constant value of $\theta \sim 3.2°$ is obtained.

It is worth mentioning that a uniform transverse density distribution $\xi(y) = n$ could be a solution for the collimation feature as well, where n is the density constant. In this case, a perfectly collimated beam with almost zero divergence $\theta \sim 0$ is predicted. Analogous behavior can be found in the interaction of laser pulse with nm-thin foil through RPA mechanism (c.f. Sec. 2.4.2) where a uniform transverse density distribution can be formed by steadily pushing by radiation pressure of the laser pulses. A reduction of the divergence might occur in conjunction with a peaked energy spectrum, as indicated in [42, 136]. However, in contrary to the presented experimental observation here.

5.5 Summary

In summary, the divergence of proton beams generated from ultrathin DLC foils is investigated in details. Well collimated proton beams with divergence half angle as low as 2° is demonstrated experimentally. This constitutes the smallest value reported so far and one order of magnitude lower than achieved with μm targets. Moreover, the proton beams are well-collimated over the complete energy range and can be further optimized by adjusting the focal spot size. Such observation indicates that the angle of emission of protons does not depend on the energy. It is an indirect proof that the transverse electron density distribution function is notably different between nm and μm targets.

The obtained experimental results indicate a reduction of divergence with foil thickness in the nm-range. As a consequence, 100 times increase in proton fluence is achieved (see Fig. 4.2 (b)), which is the key point that enables the single-shot, nanosecond, high dose radiobiological studies as presented in Chap. 4.

Understanding the exact mechanisms responsible for this beneficial behavior motivates future investigation. These observations are of particularly interest for applications. For example, investigations on the fundamental research in warm dense matter which request an intense and short ion bunch to heat solid dense material, can benefit from high flux due to the small divergence. The high flux could also be beneficial to fast ignition and neutron generation. Furthermore, a small angle of divergence relaxes the requirement of beam transportation which is essential in specific applications of ions. For example, with the smallest divergence obtained in the experiments, an almost lossless transportation is expected for the technical setup presented in Chap. 4.

Chapter 6

Exploiting relativistic nonlinearities in near-critical density plasmas for laser driven ion acceleration

To satisfy the necessary specifications of envisioned applications (see Sec. 1.2), two key areas are currently of most importance: the increase of maximum energy of ion beams and the reduction of their energy spread. The most relevant acceleration mechanisms are discussed in Sec. 2.4. As compared to TNSA mechanism, RPA is of particular interest and highly desirable because it can result in the formation of quasi-monoenergetic, peaked ion energy distribution and is effective at accelerating heavier species.

The difficulty is that ideal RPA requires laser pulses to interact with nm-scale targets that remain opaque throughout the pulse [139], while the high intensities of beyond 10^{20}W/cm^2 generally give rise to the production of a relativistic electron population that drives rapid expansion, decompression and transparency of the target. Significant decompression and high intensities may otherwise result in relativististic transparency and a transition to the BOA regime of ion acceleration, which allows high ion energies but with less control over the ion spectrum than promised by RPA (see Sec. 2.4.2).

Various schemes to prevent the production of hot electrons and decompression including using circularly polarized pulses to suppress electron heating [39] or by using heavy sacrifice ions [42, 144]. High intensities with spot sizes close to the laser wavelength can be achieved by strong focusing with normal optical components such as parabolic mirrors. While, unlike a ideally uniform beam profile (see Fig. 6.1 (b)), a strong focused finite spot gives rise to an inappropriate deformation on target surface owing to the spatial inhomogeneous of laser intensity distribution (c.f. Fig. 6.1 (a)). Therefore, in this strong focusing finite spot effects counteract the suppression of the hot electron production is

expected even using normal incidence and circular polarization [216]. For a given hot electron population, target expansion and decompression depend on the expansion time and therefore on the pulse shape. This implies an extremely rapid rise (within a few laser cycles) to the peak intensity. The steep rise time minimizes the premature decompression of the target due to the hot electrons and their associated dynamics.
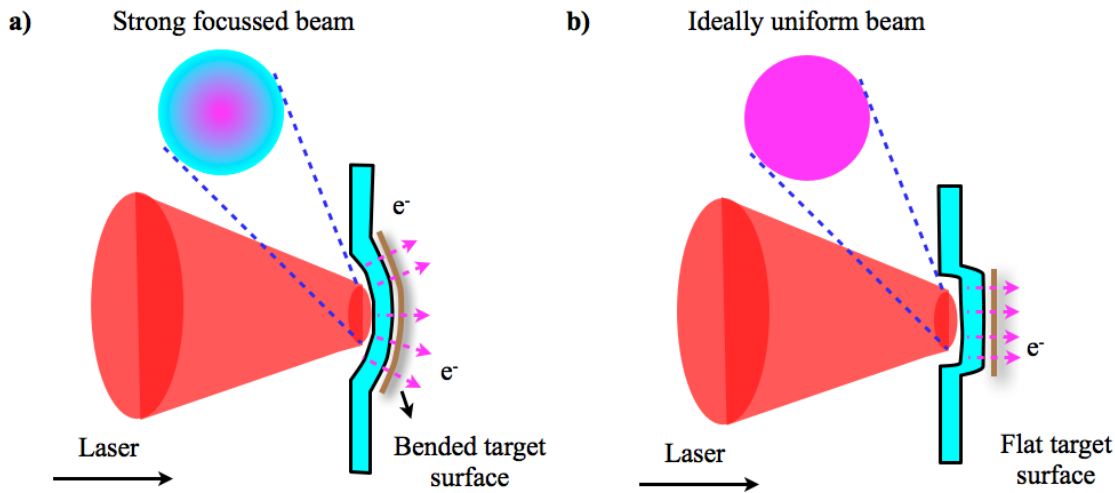

Fig. 6.1 | (a) Schematic of unwanted deformation of target surface owing to spatial inhomogeneous of laser intensity distribution, which give rise to undesired electron heating. (b) shows a flat target surface resulting from ideally uniform beam profile.

A route to achieving high intensity with a sufficiently steep rise is to shape laser pulses by virtue of relativistic nonlinearities in a plasma. With appropriate control of the interaction conditions, nonlinear processes (see Sec. 2.3.2) such as relativistic self-focusing and relativistic self-phase-modulation can be used to manipulate the laser pulse to a desired shape. Laser-driven electron acceleration in underdense plasmas, for example, has benefited from the fact that initially unsuitable, weakly focused laser pulses modify to the desired spatial and temporal shape to reach the bubble-regime [217–219], ultimately resulting in GeV-level electron bunches accelerated from centimeter-scale plasmas [220, 221]. Extending this technique to control most intense, strongly focused pulses currently achievable requires a much stronger non-linear effect than in electron acceleration scenarios and therefore densities close to the critical density at which the plasma becomes opaque. While the potential of using NCD targets as an active nonlinear optical element to control the most intense laser pulses by virtue of relativistic nonlinear effects has been noted in simulations [97], the practical implications are extremely challenging and have prevented their implementation to date.

In this chapter, the experimental results are presented demonstrating for the first time that ion acceleration can be enhanced by exploiting relativistic nonlinearities. The strongly

focused lasers used in laser driven ion acceleration is spatio-temporally compressed in a micrometer NCD plasma, resulting in substantially improved properties of ion bunch accelerated from a secondary DLC foil (see Sec. 3.2.1). 3D PIC simulations reveal that this improvement is primarily due to relativistic self-focusing. At the same time, the laser rise time is substantially reduced due to relativistic induced transparency and self-phase modulation. The combination of high intensity and steep rising edge are ideally suited to favor RPA and is consistent with the observation of non-exponential carbon-ion spectra with energies up to 200 MeV when using CP laser pulses. While with linearly polarized laser pulses, a preferable proton acceleration up to ~30 MeV is observed, yielding a substantial enhancement by a factor of 2.4. Parallel measurements of electron spectra show enhanced electron temperatures by a factor of ~2.4, consistent with the observed energy increase and indicating a significant laser intensity increase due to self-focusing in NCD plasmas.

6.1   Conceptual illustration

For better illustration, 3D PIC simulations are performed with the KLAP3D code [97, 135] to show how the intensity distribution of an initially 50 fs Astra Gemini pulse is modified when propagating through such a NCD plasma. The 3D simulation box size is $x \times y \times z = 20\mu m \times 20\mu m \times 40\mu m$, sampled by $200 \times 200 \times 1600$ cells with 27 particles in each cell. A CP laser pulse with a Gaussian temporal profile with an intensity-envelope FWHM duration of 50 fs (with a peak laser intensity of $2 \times 10^{20} \text{W/cm}^2$) and a transverse Gaussian profile with a FWHM diameter of 3.5 μm modeled the ASTRA Gemini laser pulse. A uniform carbon plasma layer with initial electron density of $2n_c$ resembling the CNF target is placed between 10 μm to 40 μm with initial electron temperature of 1 keV.

The results are shown in Fig. 6.2. Though classically overcritical, the laser pulse penetrates due to relativistically induced transparency and subsequently undergoes relativistic self-focusing. The latter is responsible for the significant increase of laser peak intensity by more than one order of magnitude at an optimum self-focusing length of 9 μm, in reasonable agreement with analytical estimation (c.f. Eq. 2.36). In addition, due to a combination of relativistically induced transparency and relativistic self-phase modulation, the pulse becomes gradually steeper leading to enhanced temporal contrast on a few cycle level. This steep rising edge suppresses the electron heating at early times and reduces the expansion of the target prior to the peak of the pulse (for details of these pulse shaping effects see Sec. 2.3.2). Consequently, the novel properties of high-intensity laser

pulses can be exploited to improve laser driven ion acceleration from nm-thin DLC foils, as shown in the inset.
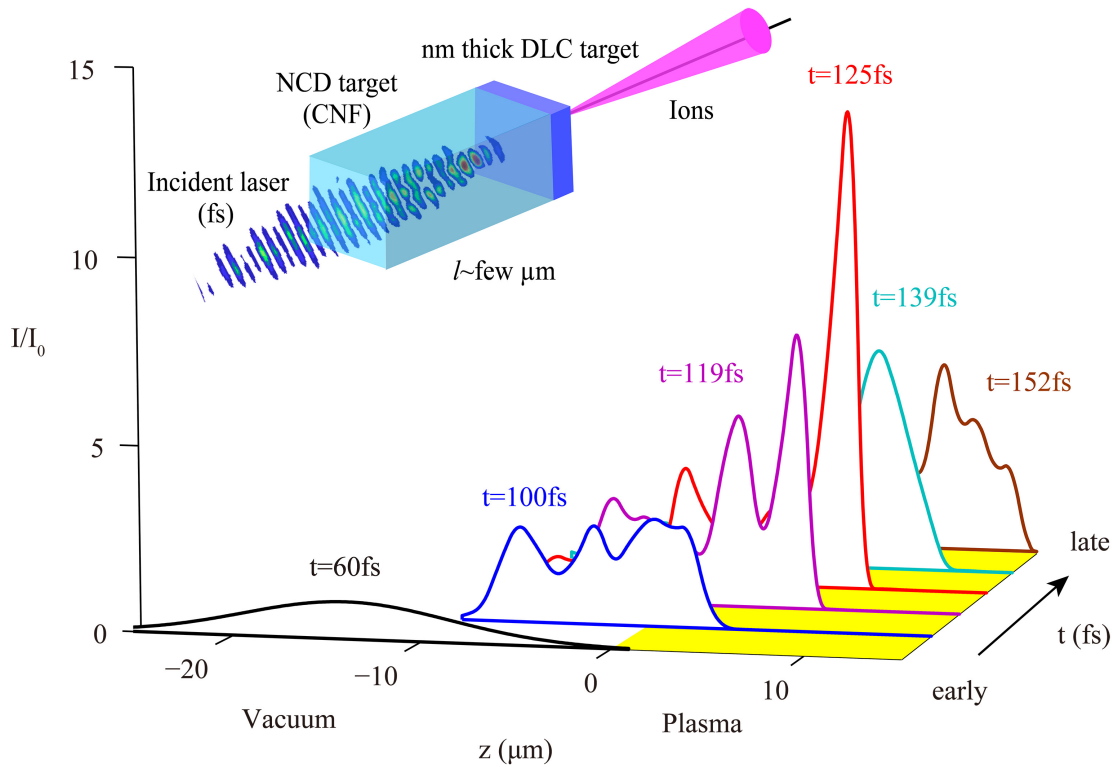

Fig. 6.2 | Laser intensity evolution in a NCD plasma similar to CNF targets. The main plot shows the on-axis intensity distribution of the circularly polarized ASTRA-Gemini laser pulse at various times during its propagation through the NCD plasma (yellow area). The peak intensity multiplies by a factor of 10 due to relativistic self-focusing as depicted in the inset and the pulse rise time steepens to a few fs. Placing a micron scale layer of NCD in front of a DLC-foil (inset) allows the enhanced pulse to be exploited for laser driven ion acceleration.

6.2   Experimental setup

The experiments were performed with the Astra Gemini laser system which delivers pulses containing energy of 4-5 J after contrast enhancement with DPM, yielding peak intensities of $2 \times 10^{20} W/cm^2$ (for details see Sec. 3.1.2). The experimental setup is shown in Fig. 6.3. The Astra Gemini laser pulse is normally incident on the target. WASP-Gemini setup (see Sec. 3.3.2) is placed after the target normal to deflect both electrons and ions with a slit entrance in front of it in the vertical dimension. The vertical entrance slit is designed to be adjustable in order to reduce the signal along zero line and distinguish the zero line. Electrons are deflected by the magnetic field to a scintillating

phosphor screen (see Sec. 3.3.1) located inside the dipole-magnet and are detected by a EMCCD camera (iXon EMCCD, Andor).

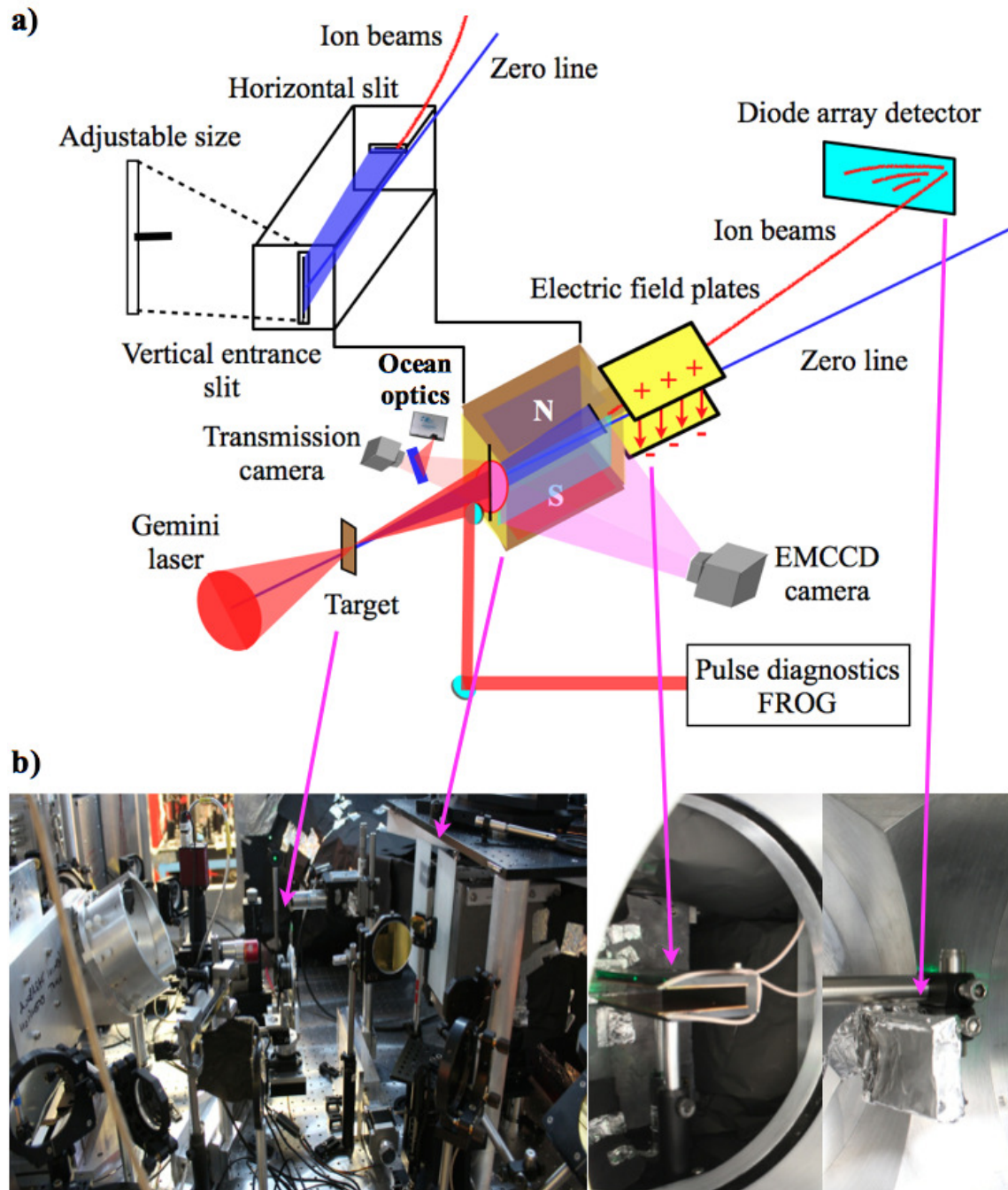**Fig. 6.3 |** (a) Schematic of the experimental setup. A series of diagnostics were fielded simultaneously to provide a comprehensively diagnosed interaction. (b) shows the actual photographs of the experimental setup.

A horizontal slit being oriented perpendicular to the vertical entrance slit was placed after the dipole-magnet. The electric field plates were located after the dipole magnets,

as shown in the upper inset. This configuration acts as a modified TP spectrometer (TP-Gemini, c.f. Sec. 3.3.2) with a RadEye^{TM} detector (see Sec. 3.3.1), allowing detection of ions under target normal. The time-integrated transmitted laser profile is detected with a scatter screen (Square glass diffuser, Thorlabs) placed in front of TP-Gemini and a 14-bit CCD camera (Pike, AVT). One FROG device is implemented to diagnose the laser pulse transmitted through the target, a detailed description can be found in [222].

As discussed above, the required NCD-plasmas must have a controllable density, must have a length controlled with micron accuracy and micron scale overall length. It must also be uniform on the scale of the laser wavelength and compatible with nm-thin target foils. These implications pose the major experimental challenge to create a complete controllable method to create (near-)uniform NCD targets with lengths on the μm-scale characteristic for the formation of the nonlinear response, i.e., the self-focusing length.
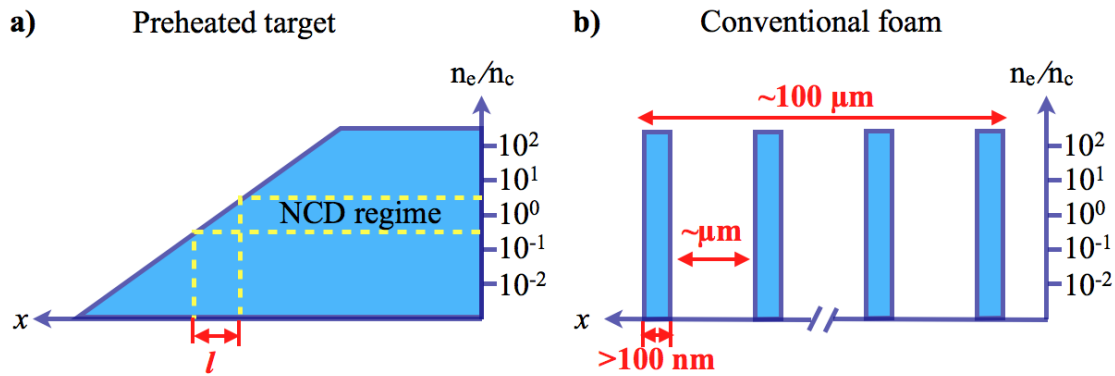

Fig. 6.4 | (a) NCD plasma with long scale-length and short NCD region typical for the production by pre-expansion of a solid density target. (b) Conventional foam targets are composed of high-density material interspersed by vacuum with a non-uniformity on length scales comparable or greater than the laser wavelength.

In previous experiments, the NCD plasmas were realized either by expanding a solid-density target with an artificial [213] or inherent prepulse of the laser [35]. The resulting plasma has only a small NCD region and will typically have much larger, lower density regions hindering a controlled exploitation of this interaction regime, as shown in Fig. 6.4 (a). Foam materials have been used but with thicknesses beyond 100 μm [223], much larger than the characteristic length scale of a few μm (see Fig. 6.4 (b)). Most importantly, the foams used to date are composed of high-density material interspersed by vacuum with a non-uniformity on length scales comparable or greater than the laser wavelength. This implies that a laser will either interact with a dense array of wavelength scale solid clusters in the case of a short, high contrast pulse, or in the case of a preheated target with long density gradients, even if they can reach the required densities in excess of 10^{21}

cm^{-3}. Both methods have severe limitations which are overcome by employing CNF (c.f. Sec. 3.2.2). CNF is an ideal candidate for these specifications, providing a homogenous NCD plasma slab with sharp boundaries and an average electron density of (2 ± 1) n_c, as detailed discussed in Sec. 3.2.2. In the presented experiments, CNF targets with thickness of 0-5 μm (corresponding to areal density of 0-3.75 μ g/cm^2) were directly grown onto DLC foils with thickness of 5-20 nm.

6.3   Signature of pulse steepening
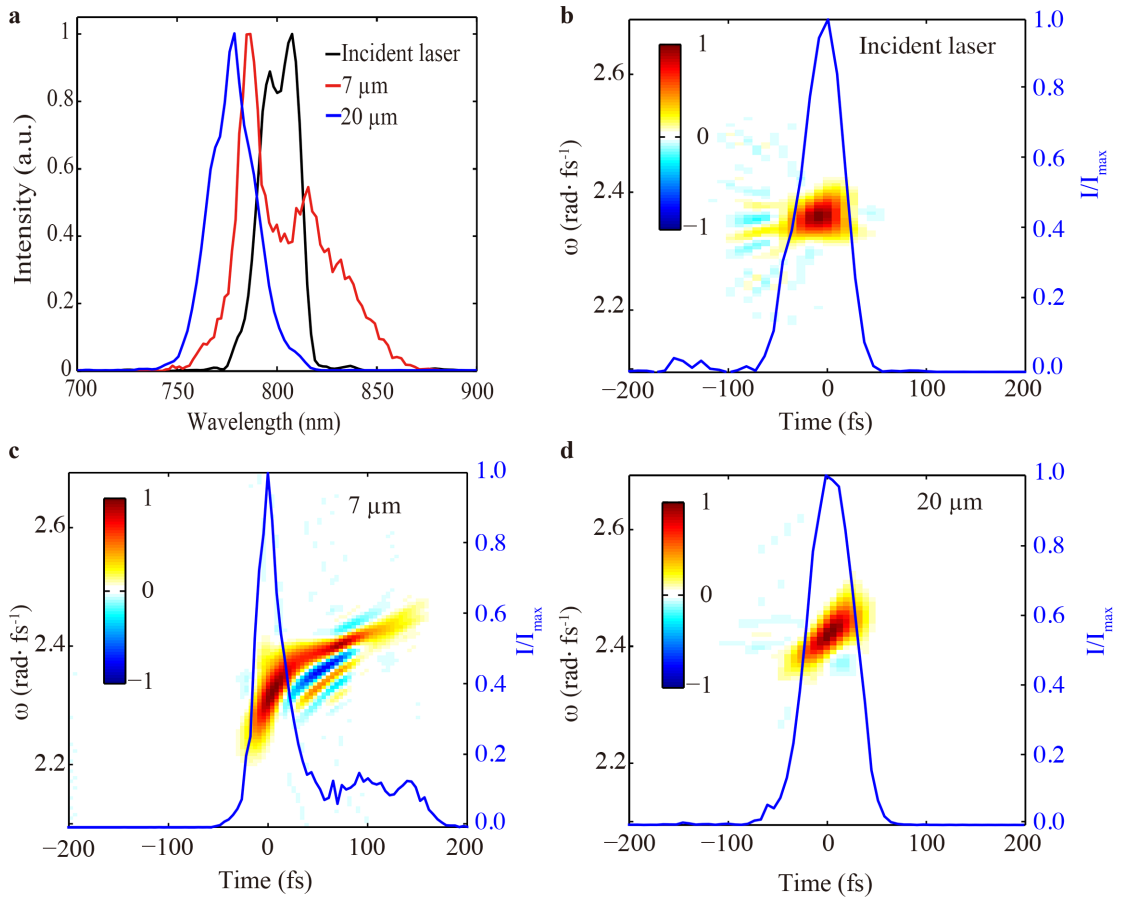
Fig. 6.5 | (a) Normalized laser spectra of incident laser (black line) compared to transmitted through CNF targets with thickness of 7 μm (red) and 20 μm (blue). (b) Wigner distribution of fields retrieved from the FROG-measurements for incident laser, (c) for the CNF targets with thickess of 7 μm, and (d) with thickness of 20 μm. The overlaid blue curves in b, c, and d represent the temporal intensity distribution where t<0 denotes early time.

To gain confidence in the pulse shaping effects and benchmark the 3D PIC simulations, the temporal shape of transmitted pulses through freestanding CNFs with various thicknesses are performed via a FROG device (c.f. Fig. 6.3). The spectrum of the incident

pulse, shown by the black curve in Fig. 6.5 (a), has a FWHM width of 23 nm corresponding to the nearly transform limited pulse duration of 50 fs (Fig. 6.5 (b)). After propagation through a freestanding CNF with a thickness of 7 μm, the spectral width is significantly broadened to 37 nm (red curve in Fig. 6.5 (c)). This broadening is required to support a steeper pulse. Further evidence can be inferred from the positive chirp which is observed in the Wigner distribution of the laser field in Fig. 6.5 (c). Indeed, the corresponding temporal profile shown by the overlaid blue curve is steepened. Moreover, the pulse front steepening observed in the 3D PIC simulation is in line with the measured profile, as shown in Fig. 6.6 (a). The experimental observations thus reproduce the main features expected from both the theoretical expectations (see Sec. 2.3.2) and the simulation results qualitatively: spectral broadening, positive chirp and pulse steepening.

Independent measurements of the overall transmitted laser spectrum are conducted where the complete beam is collected and measured by an ocean optics (USB2000+, Ocean optics), as shown in Fig. 6.3 (a). The results are very close to those spectra retrieved from the FROG measurements, as shown in Fig. 6.6 (b). This indicates that the measured pulse shapes from FROG measurements are representative of the whole beam though only performed with a small portion of the beam.
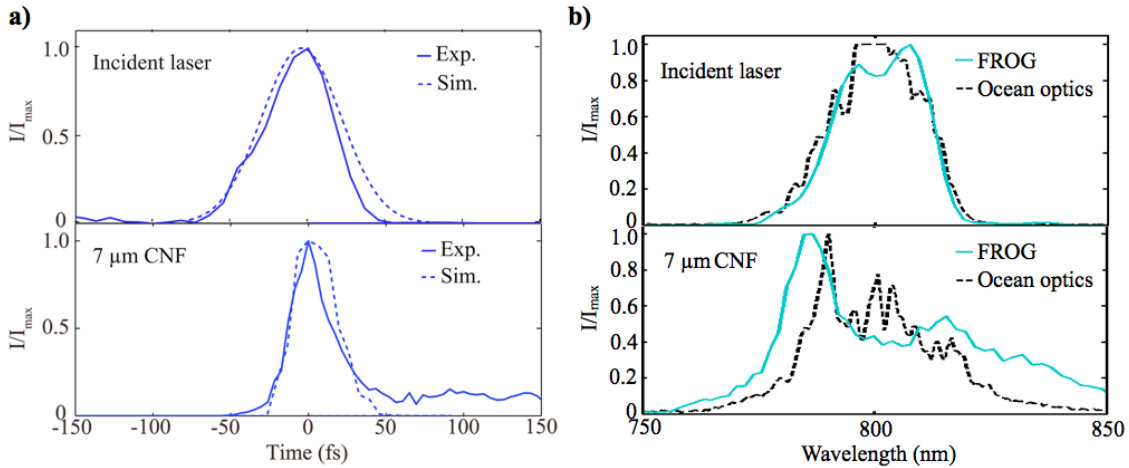
Fig. 6.6 | (a) shows the comparison of measured temporal intensity distributions (solid curves) with the extracted ones from PIC simulations (dashed curves). (b) shows the comparison of measured temporal shapes with FROG (solid cyan curves) and with an independent overall laser spectrum measured with an ocean optics (dashed black curves).

It is interesting to note that when using thicker CNF target, with thickness up to 20 μm, the temporal shape is almost unaltered (Fig. 6.5 (d)) but overall spectrally blue-shifted (Fig. 6.5 (a)), suggesting that in terms of pulse shaping the optimum thickness is around a few μm. For thicker targets, the pulse steepening is less efficient, in agreement with the theoretical predication [97].

6.4　Laser driven ion beams with CP pulses

6.4.1　Experimental results

Fig. 6.7 | Maximum energies of protons (a) and C^{6+}-ions (b) plotted as a function of the CNF-thickness. Different line colors correspond to different thickness of the secondary DLC foils. (c) The best results obtained with CP laser pulses when interacting with CNF attached to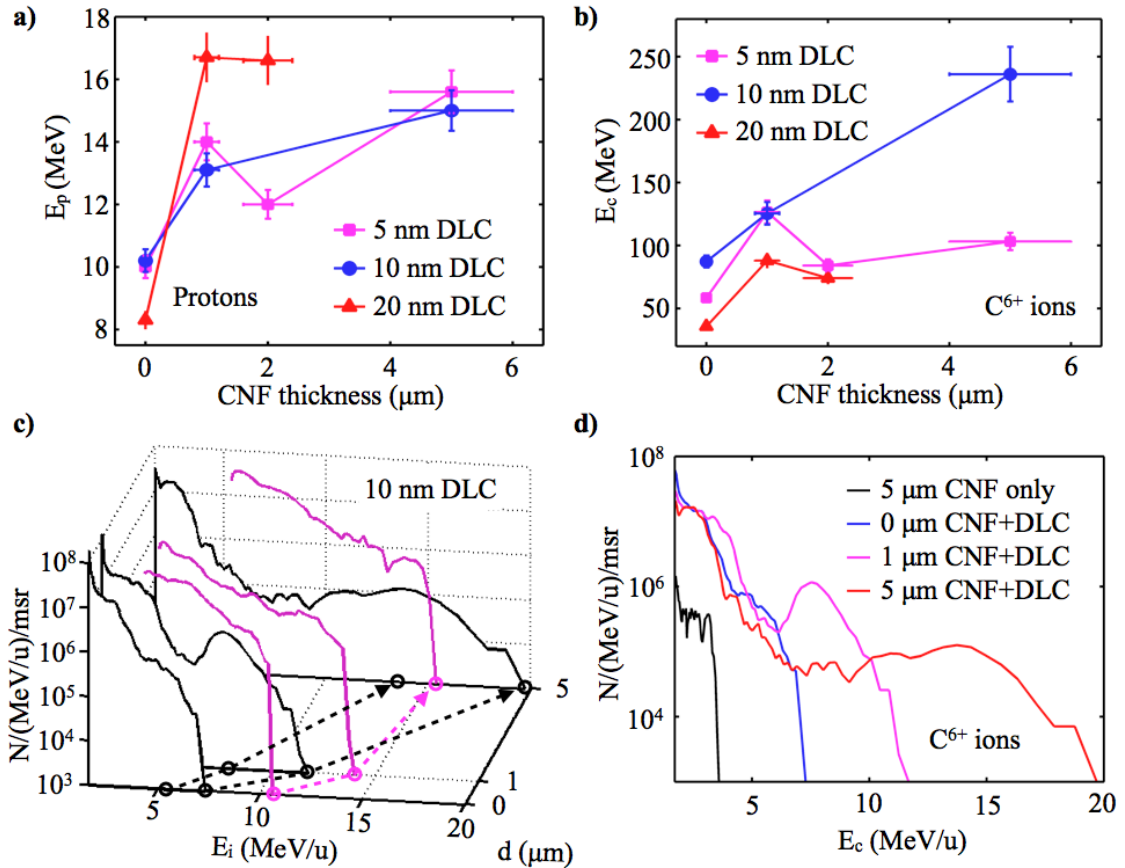 a 10 nm DLC foil. The magenta curves show the proton spectra, the black curves the C^{6+}-ion spectra from the same laser shot. The dashed lines visualize the dependence of representative energy parameters, in particular the maximum energy and the energy of the spectral peak on length of the CNF. The corresponding C^{6+}-ion spectra are shown as a side view of (c) in (d) along with the obtained spectrum from freestanding CNF target with thickness of 5 μm.

The most interesting results were obtained with circularly polarized laser pulses. Fig. 6.7 (a) and (b) show the maximum energies of protons and C^{6+}-ions extracted from the recorded Thomson parabola traces with circularly polarized laser pulses from the double-layer targets (i.e., CNF+DLC configuration). Regardless of DLC-thickness, the energies increase with increasing CNF-thickness. Best performance is observed for 10 nm DLC, as shown in Fig. 6.7 (c). The corresponding energy distributions of protons and C^{6+} ions reveal that carbon acceleration benefits most, their energies are increased by a factor of

2.7, while proton energies only increase by 1.5. Moreover, the shape of the carbon spectra deviates from monotonically decaying and are elevated at around 70% of the maximum energy (for a better view see Fig. 6.7 (d)). This observation had previously been associated with RPA [39]. Further evidence is that the energy per nucleon of the carbon ions increases more rapidly than the proton energy, and eventually become comparable, i.e. the fastest ions travel with similar velocities, as discussed in Sec. 2.4.2. The observed maximum carbon energy ~20 MeV/u is to the best of our knowledge, the highest value for carbon ions demonstrated from a Gemini-class laser system to date.

Freestanding CNF target with thickness of 5 μm was tested as well, although carbon ions were registered when irradiating freestanding CNF targets, their energy and number were insignificant. In the detectable spectra range of 2-50 MeV/u, no proton trace was observed and only carbon ions with lower maximum energy of about 3 MeV/u with more than two orders of magnitudes smaller particle numbers were observed (Fig. 6.7 (d)).

6.4.2   Discussion

Freestanding CNF-targets resulted in minimal ion emission (~10^3 less ions with lower maximum energy of about 3 MeV/u) suggesting that their role is indeed mainly to provide a medium for modifying the laser pulse to the desired shape. To validate this hypothesis further, we performed more detailed 3D PIC simulations. Due to the multi-scale nature of the problem, i.e. μm long plasma with low density and a nm-thin, high density foil, the problem is simplified by dividing the simulation into two steps. First, the propagation of the Gemini-laser pulse through a NCD-plasma with electron density of $2n_c$ (resembling the CNF-plasma) was simulated and the complete resulting electro-magnetic field was extracted at different depths within the NCD plasma. This field was then fed into a second simulation with a single DLC foil. A solid density plasma slab (60 nm, $100n_c$, C:H=9:1 in number density, initial temperature of 1 keV) was used to represent a DLC foil with the reduced density allowing for any initial decompression during the early stages of the interaction and also reduces the computational requirements. Here, the resolution of the simulation box is set to 100 cells/μm to resolve the DLC foil thickness. Noted that to account for the limited solid angle of the Thomson parabola spectrometer (~1×10^{-7} sr), only particles propagating in forward direction with a cone of half angle 0.15 rad was considered for the simulation results. The major limitation of this approach is that fast electrons produced within the NCD-plasma do not contribute to the ion acceleration at the DLC-foil. Consequently the sheath fields at the rear which would preferentially affect the protons maybe underestimated.

The simulation results are shown in Fig. 6.8. As in the experiments, a significant increase of the maximum carbon ion energy with increasing CNF-thickness is observed. The ratio of these energies to the energy obtained for a plain DLC-foil defines the enhancement factor and is plotted against CNF-thickness in Fig. 6.8 (a). The general trend of both the experiment and simulation results agrees very well and suggests that the capacity of the scheme in the parameter range accessed in the experiments is not fully explored. The specific simulation predicts a 4-fold increase in energy when using a plasma with 9 μm length.
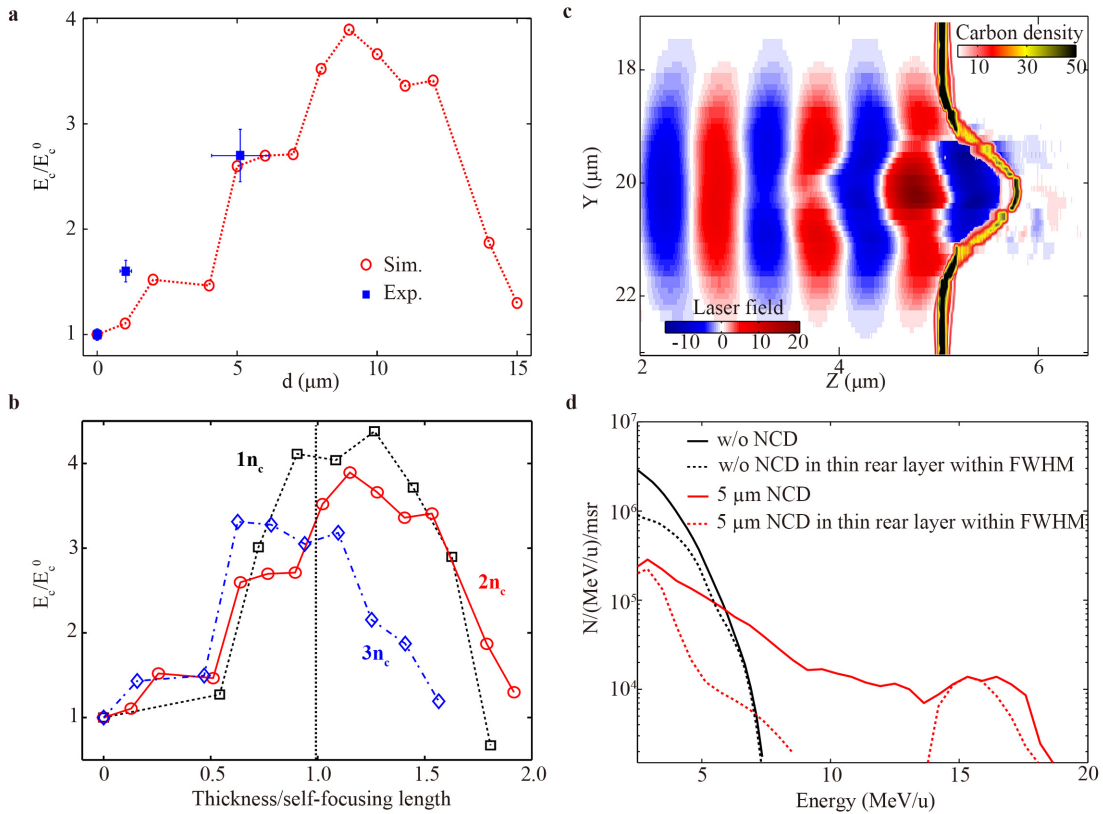
Fig. 6.8 | (a) Maximum energy of carbon ions extracted from the simulated C^{6+}-energy spectra at t=260 fs. The maximum energy gradually increases up to a maximum of 4× when the NCD-length reaches 9 μm. (b) Same plot as in (a), but now the NCD-thickness is normalized to the self-focusing length and 3D-simulations with three different electron densities ($1n_c$, $2n_c$ and $3n_c$) are compared. The general trend shows that ion acceleration is optimized when the NCD length approaches the self-focusing length. (c) 2D Density map of C^{6+} ions and laser field distribution obtained at t=100 fs in case of 5 μm NCD as in (a). (d) Energy spectrum of C^{6+} ions from simulation in case of 0 (plain DLC-foil only) and 5 μm NCD as in (a). The solid curves present the spectrum from the whole target (60 nm thick) while the dashed curves show the fraction of spectrum for ions in the focal volume (FWHM diameter of 3.5 μm for initial pulse and of 1.5 μm for modified pulse, respectively) and initially in a thin layer (20 nm, 1/3 of the target thickness) in the rear side.

After this distance, the laser has reached its highest intensity via self-focusing. The corresponding self-focusing length agrees well with the simple estimate based on Eq. 2.36. When performing the same set of simulations with NCD-plasma densities of $1n_c$ and $3n_c$ and identical parameters otherwise, ion acceleration is optimized when the NCD thickness corresponds to the respective self-focusing length (see Fig. 6.8 (b)). This suggests that the effect of the NCD plasma is robust to variation of the exact density and that the observed carbon energy increase is primarily due to the enhanced laser pulse interacting with the DLC foil. Even though the effects of the fast electrons generated in the CNF-plasma can not be excluded, they seem have minor impact.

It is interesting to discuss the results with respect to possible ion acceleration mechanisms which are at play under our conditions. The strong enhancement of carbon ion energies for circular polarization (which is not typical for TNSA for which protons are preferable accelerated), the significantly altered spectral shape, and the fact that protons and carbon ions reach similar velocities suggest that RPA is significantly contributing. The carbon spectra show a significant peak, which is not observed for linear polarization (see Sec. 6.5.1). The structure/width of this peak depends on the thickness of the NCD-plasma, and is wider when the intensity of the laser increases due to self-focusing. Numerical investigations (see Sec. 2.4.2) suggest that RPA is more likely to dominate over TNSA when circularly polarized laser pulses at normal incidence are used, electron heating required for TNSA is suppressed. In tight focusing experiments with thin foils however, this advantage is generally not observed due to strong radial intensity gradients which results in foil deformation and a comparable hot electron production regardless of polarization state [216]. For a given laser intensity and spot size this deformation can be reduced by using pulses with a steeper rising edge. In the presented situation, the steepened pulse front significantly reduces the time available for deformation to take place. This results in slower decompression of the foil and an increased RPA contribution.

Indeed, the above interpretation is confirmed by the 3D PIC simulation results. Fig. 6.8 (c) shows the 2D (Y-Z) density map of C^{6+} ions extracted from simulations. The carbon ions are accelerated in manner typical of RPA with the modified pulse: The foil is accelerated as a whole and remains highly overdense while its shape closely resembles the transverse laser profile. The target remains highly reflective with almost no transmitted laser energy, which is well in line with the measured overall few-percentage laser transmission. The resulting spectral shape presents a non-exponential distribution as shown in Fig. 6.8 (d), showing qualitatively agreement to the measured shape. In particular, the high-energy spectral peak can be seen to be formed by the ions in the focal volume in a thin layer in the rear side of the target. This is consistent with a previous theoretical investigation [140], which shows that only a thin layer at the target rear in the focal

volume forms the monoenergetic feature during RPA. By contrast, the C^{6+} ions spectra for a plain DLC-foil with the unmodified pulse presents more exponential-like spectra consistent with dominating TNSA.

6.5 Laser driven ion beams with LP pulses

6.5.1 Experimental results
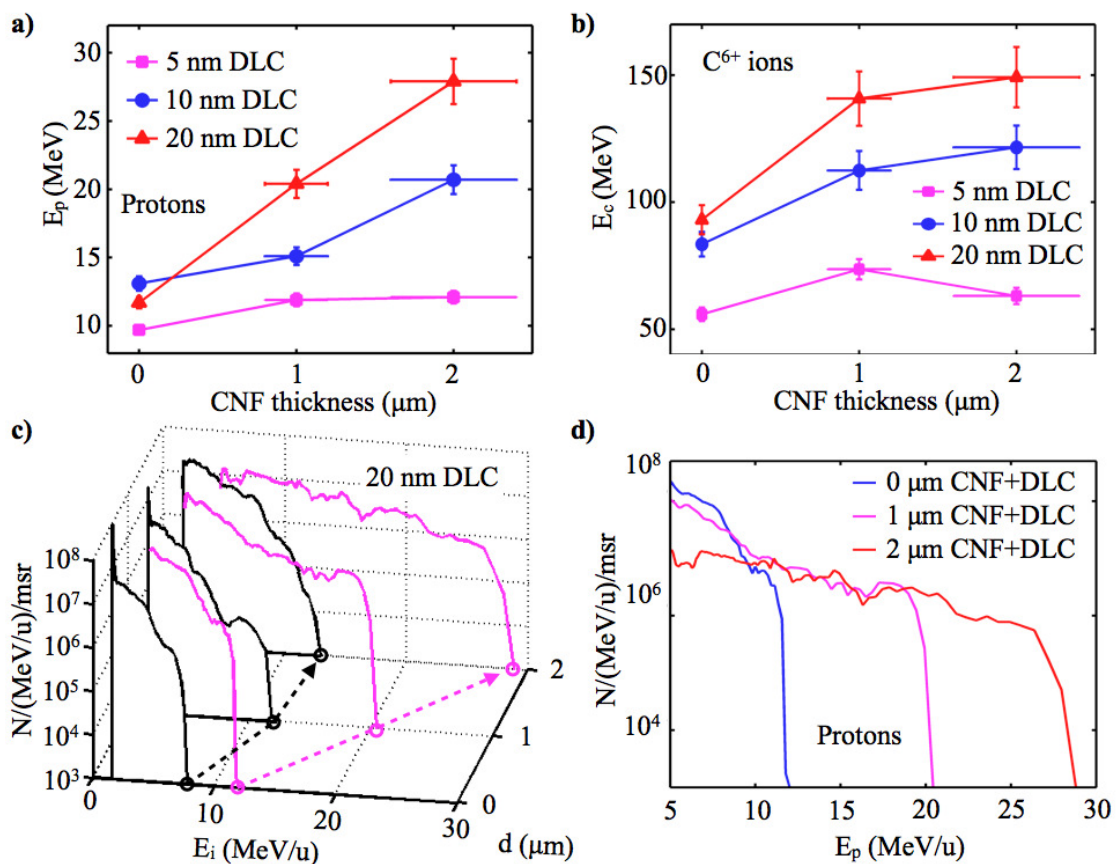
Fig. 6.9 | Maximum energies of protons (a) and C^{6+}-ions (b) plotted as a function of the CNF-thickness. Different line colors correspond to different thickness of the secondary DLC foils. (c) The best results obtained with CP laser pulses when interacting with CNF attached to a 20 nm DLC foil. The magenta curves show the proton spectra, the black curves the C^{6+}-ion spectra from the same laser shot. The dashed lines visualize the dependence of representative energy parameters. (d) presents the corresponding C^{6+}-ion spectra as a side view of (c).

The results are summarized in Fig. 6.9 (a) and (b). Again, the energies increased with increasing CNF thickness regardless of all presented target thicknesses. The best performance is obtained for 20 nm DLC (see Fig. 6.9 (c) and (d)). In contrast to circular polarization, linearly polarized laser pulses invariably resulted in monotonically decaying

spectra, both for protons and C^{6+}-ions. Proton energies were enhanced more strongly from 12 to 29 MeV, a factor of 2.4, while C^{6+} energies by a smaller factor of 1.7. In addition, similar behavior was observed with freestanding CNF target (no detectable protons and C^{6+}-ions with maximum energy of ~3 MeV/u).

6.5.2 Discussion

In the experiments, the energy distributions monotonically decay and terminate at a maximum energy value for linear polarization (c.f. Fig. 6.9 (c)), characteristic for ion acceleration dominated by expanding hot plasma, as discussed in Sec. 2.4.1. With increasing CNF layer thickness this maximum energy increases from 12 to 29 MeV - a factor of 2.4. At the same time, the maximum energy per nucleon of the C^{6+} ions increases by a factor of 1.7 (~$2.4/\sqrt{2}$), consisting with the fact that ion with higher charge-to-mass ratio are preferentially accelerated by plasma expansion. Also, this suggests that the acceleration potential ΔV is increased by a factor of 2.4 for both ion species. Since the ions are accelerated in an electric field set up by fast laser-accelerated electrons. The actual dynamics, i.e. dominated by plasma expansion or alternative schemes currently under investigation, plays a minor role for the discussion. Depending on the parameter range, in target normal sheath acceleration ΔV scales with the square-root (see Sec. 2.4.1) of or even linear with the laser intensity I_0 [224]. Thus, the CNF increases the laser intensity by a factor of 2.4-5.8. In the BOA regime [114–117], $\Delta V \propto I_0^{1/2} t_{FWHM}^{1/3}$ also depends weakly on the laser pulse duration t_{FWHM}, but as well on the square-root of the intensity [170]. Keeping in mind that the laser pulse is steepened in the CNF targets, this scaling would suggest a factor of slightly higher than 5.8 for the intensity increase. Also, as shown in the aforementioned 3D simulation (c.f. Fig. 6.2), the laser pulse needs some distance to reach an optimum, i.e., the maximum laser intensity with a significantly enhanced contrast. Hence, the intensity increases with increasing CNF thickness up to some optimum. Such an increase is then directly reflected in maximum energy of ions, as confirmed experimentally.

This interpretation is again supported by the measurements of the electron spectra. The on-axis electron spectrum can be seen in Fig. 6.10 (a), presenting a typical exponential distribution with hot electron temperature T_h of 3.4 ± 0.4 MeV, agreeing well with a theoretical T_h value of 3.1 MeV derived from the ponderomotive force scaling at solid-density targets for given Astra Gemini laser parameters (c.f. Eq. 2.46). It rises to a value of 8.3 ± 0.6 MeV by ~2.4 when adding 2 μm CNF layer. The observed increase is consistent with the expected increase in ΔV (~2.4). Moreover, Fig. 6.10 (b) and (c) show the maximum energies of protons and C^{6+} ions as a function of on-axis hot electron temperature T_h extracted from the measured electron spectra. The maximum energies of both

species increase with T_h. Also, the trend of increasing T_h with increasing length of propagation through the CNF-plasma is clearly evident in Fig. 6.10 (d). A number of different effects may attribute to the experimental observations. Theoretical investigations suggest that the presence of underdense or NCD plasmas in front of solid density targets can give rise to enhanced ion acceleration [97, 225, 226] for linear polarization via relativistic self-focusing effect (c.f Fig. 6.2) or directly electron acceleration (DLA) [227, 228]. Accordingly, the electron temperature is increased, leading to a strong accelerating electric field and consequently higher ion energy.
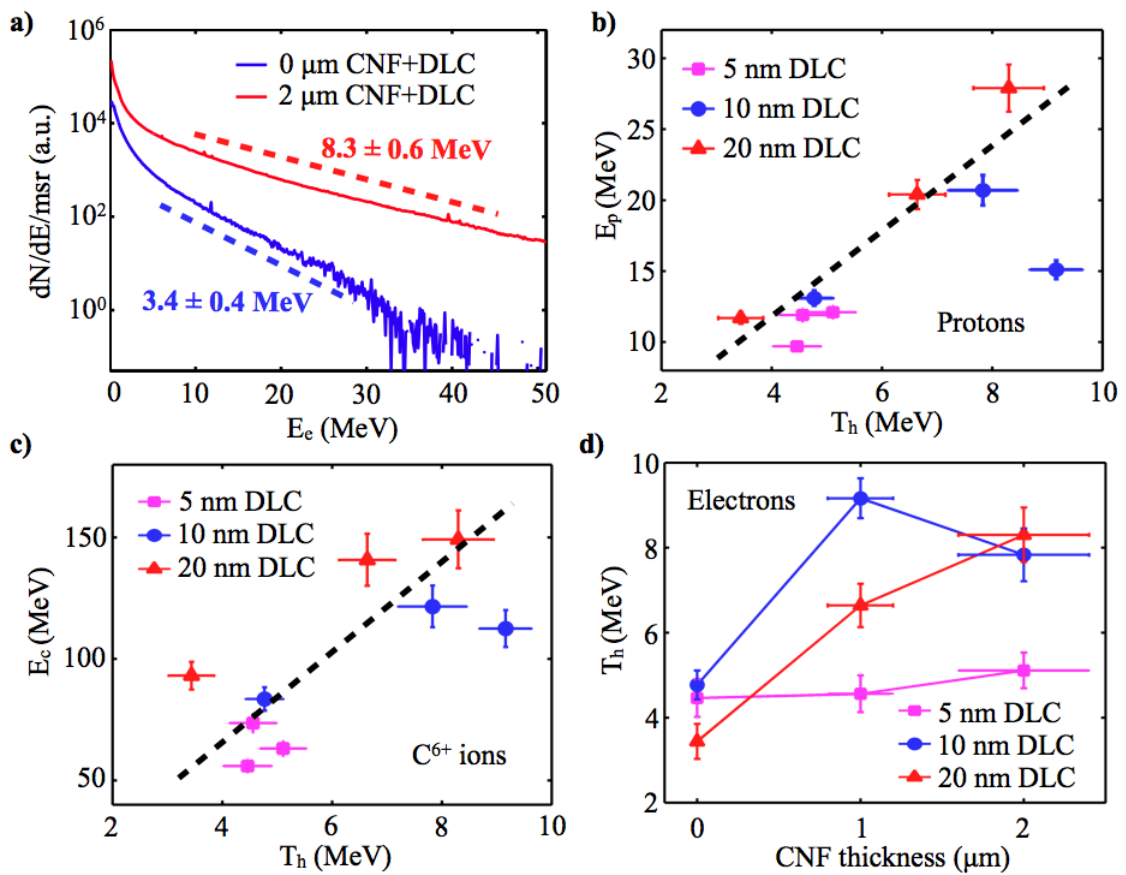
Fig. 6.10 | (a) Measured on-axis electron energy spectra with LP pulses interacting with CNF with thickness of 0 (blue) and 2 μm (red) attached to a 20 nm DLC foil. The maximum energies of protons (a) and C^{6+} ions (b) against measured on-axis hot electron temperature T_h for varying DLC-thickness. (d) T_h plotted as a function of the CNF-thickness. Different line colors correspond to different thickness of the secondary DLC foils.

6.6   Summary

In summary, the practical feasibility of using ultrathin CNF targets to realize relativistic self-focusing, self-phase modulation and relativistic induced transparency at the same

time has been demonstrated. This enabled acceleration of ions from nm-thin DLC targets to substantially higher energies, about a factor of 3, which would otherwise require much larger lasers. A preferable enhancement of the carbon energy for circular polarization is observed, consistent with a stronger RPA contribution to the overall acceleration. When using linearly polarized laser pulses, monotonically decaying energy spectra were observed both for protons and carbons. Protons gain the most pronounced energy enhancement by a factor of 2.4, consistent with parallel measurements of on-axis electron temperature.

Although this was a "proof-of-principle" experiment for the technique,this initial application to ion acceleration shows significant improvements of interest for future applications. Future research will focus on determining the ultimate range of enhancement and steepening that can be obtained with near critical plasmas and can be extended to high-intensity applications that request a desired pulse shape.

Chapter 7

Laser driven proton beams from nanometer thin foils: detailed experimental insights

Nanometer thin foils have proved their potential in recent experimental studies. In the framework of this thesis (c.f. Chap. 5), it is found that nm thick DLC foil provides superior properties in terms of divergence. The obtained small divergence along with the collimation feature is certainly benefitial for practical applications that require a subsequent transportation. In the first part of this chapter, detailed experimental studies of laser driven ion acceleration from 5 - 20 nm thin DLC foils (c.f. Sec. 3.2.1) are summarized. Interestingly, the highest energy of proton beams up to 6 MeV was obtained with a moderate laser intensity of only $5 \times 10^{18} W/cm^2$, appearing at the same position for minimum divergence (See Chap. 5), i.e., when moving the target out of focal plane by a distance as much as 4 times Rayleigh length to both sides ($\pm 100 \ \mu$m). Laser absorption to the target is determined by parallel measurements of laser transmission and reflection, evidencing a direct correlation to the observed maximum proton energy. Similar behavior was reproduced by applying the analytical model of Schreiber *et al* [130], indicating a more direct correlation between proton energy and absorbed laser energy rather than the incident laser intensity. The dependence of maximum energy on laser pulse duration is presented in the second part. Optimum results from nanometer thin foils were obtained with the shortest pulse duration ($\sim$ 30 fs), in contrast to μm thick targets where the optimum durations were observed to at larger values ($\sim$ 190 fs).

7.1   Experimental setup

The experiment was conducted with the ATLAS laser system with throughput energies of 400 mJ after DPM system, resulting in peak intensities of of 8×10^{19}W/cm^2. A detailed description is given in Sec. 3.1.1. Fig. 7.1 shows the experimental setup at MPQ. Identical to the setup described in Chap. 4, the ATLAS laser pulse is normally incident on nm-thin DLC foils (c.f. Sec. 3.2.1) with thickness of 5-20 nm. The actual spot size on target ranging from 3 to 22 μm was adjusted by moving the target along the laser axis. The WASP-MPQ setup (see Sec. 3.3.2) was employed for simultaneous detections of electrons and protons. Here, a Al foil with thickness of 45 μm was placed in front of IP ion detector. Protons with energies above 2 MeV can thus be recorded.
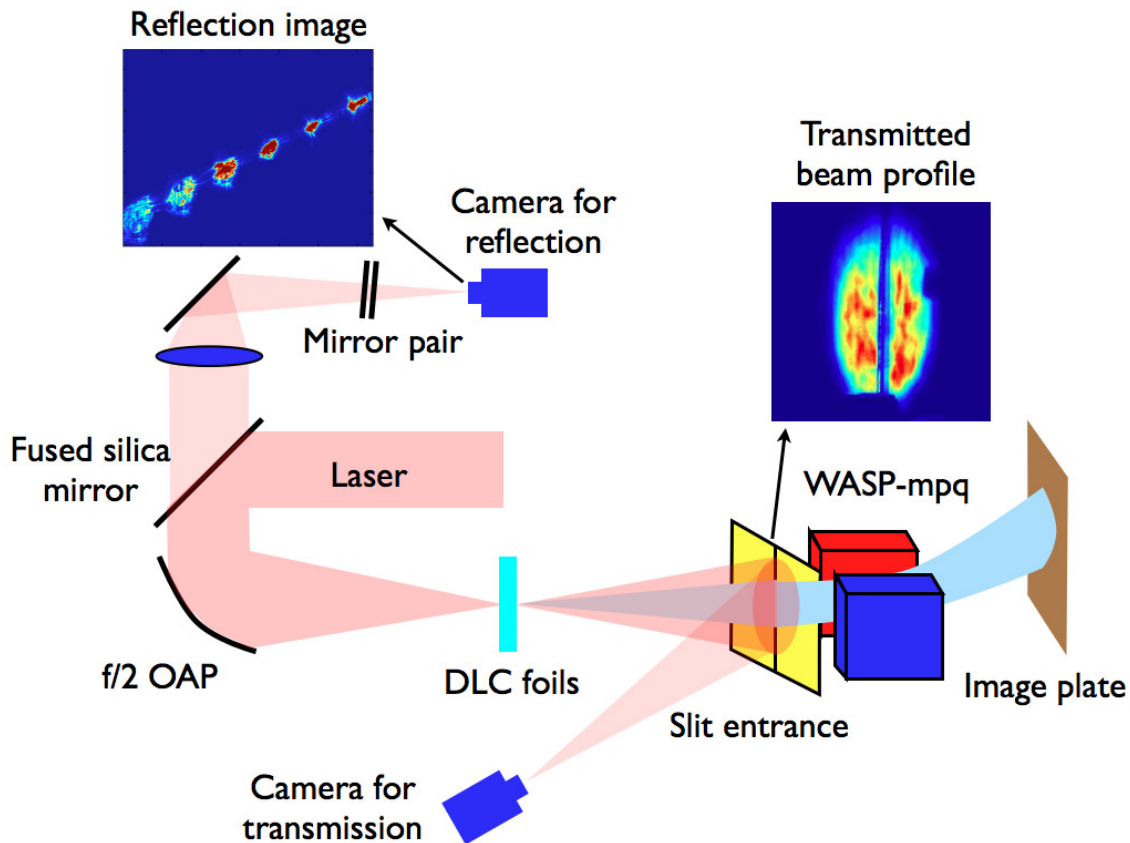
Fig. 7.1 | Schematic of experimental setup with ATLAS. The right inset presents a measured transmitted image in vacuum as the calibration shot, and the left inset shows a typical reflection image within a selected area. A series of reflected points can be seen in the image which is resulted from multi-reflection from a pair of aluminum mirrors located in front of the reflection camera.

In addition, the transmitted laser profile is measured by imaging a plastic foil in front of the slit entrance onto a CCD camera. The reflected laser light is re-collimated by the OAP and propagated through a specially designed high-transmission (1%) fused silica

based mirror with full aperture. A mirror pair separated with 1 mm (serving as a fabry-perot) is used to get multiple replica of the beam on a CCD camera. The images are used to determine the reflectivity of the laser pulse and the transmission is given by the integration of the recorded laser profiles. The laser absorption is thus determined by the parallel measurement of laser transmission and reflection assuming that no light is scattered in other angles which are not covered by the described diagnostics.

7.2   Experimental results

7.2.1   The relevance of laser absorption
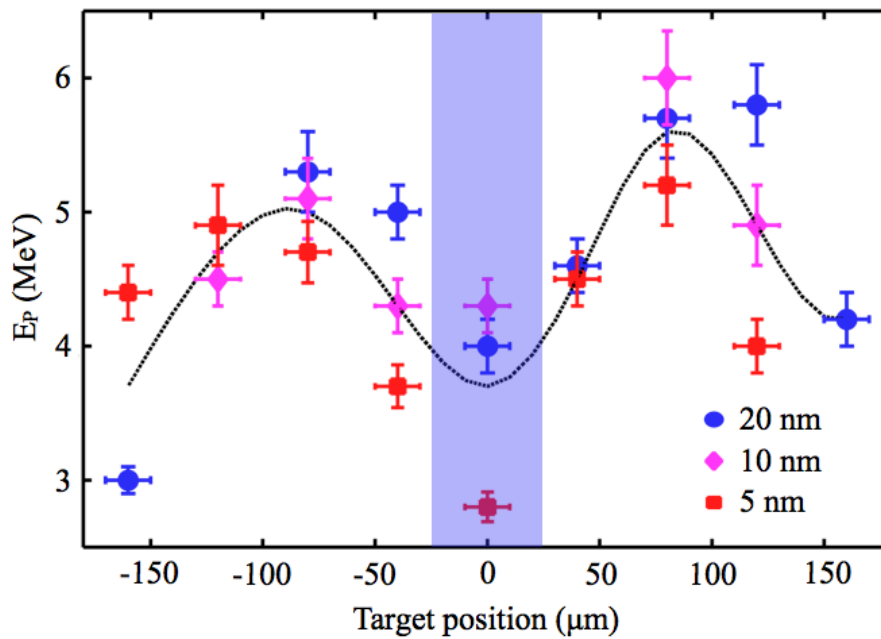
Fig. 7.2 | Maximum proton energy E_p for varying target positions, where +/- means the foils were placed before/after laser focal plane. Different colors correspond to different thickness of DLC foils. The dashed black curve is obtained by taking the average energy value at each target position, showing that the highest values are preferably attained at about $\pm 100\,\mu$m when moving the target out of the focal plane.

Fig. 7.2 shows the maximum energies of protons E_p for varying target thicknesses and their positions with respect to the focal plane. Here, the vertical error bars show the systematic uncertainty of the spectrometer for the maximum proton energy while the horizontal error bar shows the positioning accuracy of about 10 μm. The maximum energy of protons varied from 3 MeV to 6 MeV over the parameter scan. Most strikingly, regardless of the target thickness, the best performance is obtained when moving the target

out of focal plane to both side by about $\pm 100\,\mu$m, far beyond the Rayleigh length of 25 μm which is marked by the light blue area. Proton beams with energies up to 6 MeV are obtained at these positions with moderate intensities of about 5×10^{18}W/cm^2, slightly over the relativistic threshold (c.f. Sec. 2.2.1). While the observed energies at the best focus are considerably smaller ($\sim$ 4 MeV), even though the laser intensities of 8×10^{19}W/cm^2 is one order of magnitude higher.
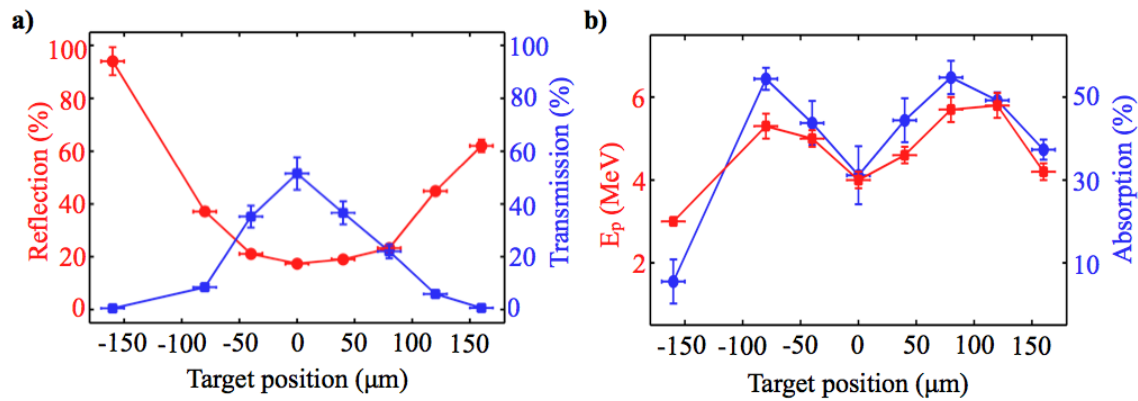

Fig. 7.3 | (a) Measured reflection R (red) and transmission R (blue) rates through 20 nm thick DLC foils with varying target positions. (b) Maximum proton energy (red) and estimated absorption (blue) as a function of target position. In all the graphs, the horizontal error bars show the positioning accuracy of 10 μm.

Additional information is given by the parallel measurements of laser reflection and transmission rates. Fig. 7.3 (a) shows the measured values from 20 nm DLC foils. Here the vertical error bar for the reflection rate indicates the standard deviation derived from the multiple replica of the reflected beam. A 12 % energy fluctuation depending on the laser performance on a daily basis is reflected in the vertical error bars for the transmission rate.

The transmission rate T is maximized at 50% when targets are at best focus. The values reduce with target positions to both sides and approach almost zero at target position $\approx 150\,\mu$m. A minimum reflection rate R of about 20% is observed at best focus. While the reflection rates increase when moving target out of focal plane. According to the measured values, laser absorption rate A is estimated as $A = 1 - T - R$ and plotted for varying target positions in Fig. 7.3 (b). Interestingly, the laser absorption rates A follow a dependence on the target positions similar as E_p. Optimum laser absorption rates were obtained at the same target positions of about $\pm 100\,\mu$m for maximum proton energy.

Similar behavior are observed for thinner target thicknesses (5 and 10 nm). Fig. 7.4 shows E_p as a function of the estimated laser absorption A for the obtained data set. A di-

rect correlation from laser absorption to maximum energy is clearly visible. E_p increases with increasing laser absorption regardless of target thickness and position.
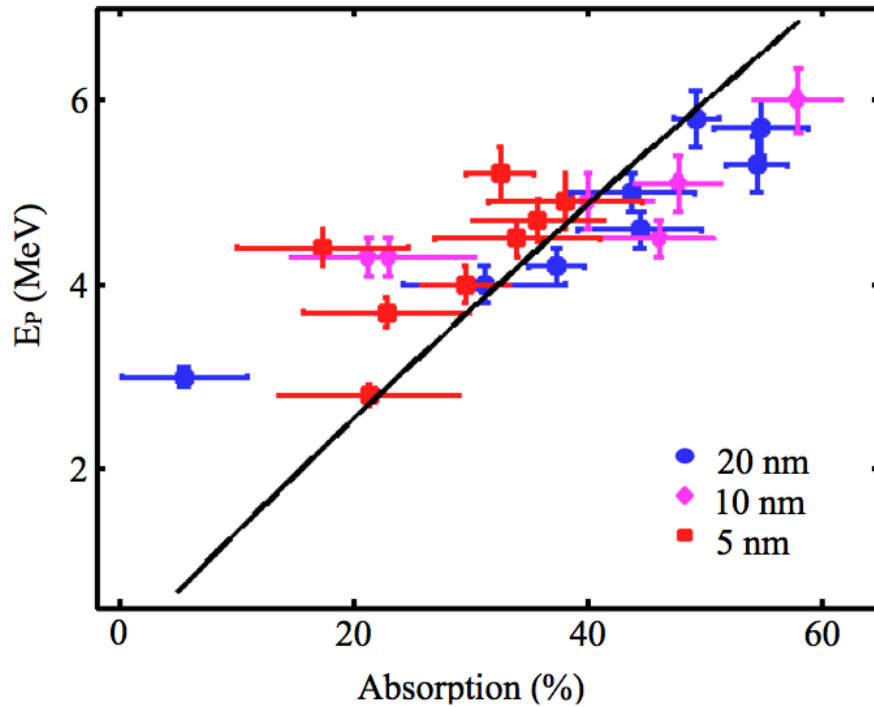

Fig. 7.4 | Measured maximum proton energy E_p plotted as a function of the estimated laser absorption $A = 1 - T - R$ based on the experimental results of the reflection and transmission rates for varying thickness of DLC foils. The black curve is obtained from Eq. 2.53 by applying the analytical model of Schreiber *et al* [130], consistent with the experimental data. Here, the transverse spread of the electrons is set to be $B = 2.2$ μm (c.f. Eq. 2.51).

To explain the experimental finding, the analytical model of Schreiber *et al* [130] was applied. As introduced in Sec. 2.4.1, this model shows an explicit dependence of accelerated ion energy on absorbed laser energy rather than incident laser intensity and has been successfully employed to explain previous experimental findings [130, 224]. Assuming a constant transverse spread of the electrons $B = 2.2$ μm, the black curve in Fig. 7.4 shows predicted maximum proton energies E_p of this model for the experimental parameters presented here, which are in well agreement with the experimental data. The only assumption that the unknown electron transverse spread B is constant and much smaller than the actual focal spot size at larger target positions would suggest that possibly more complicated laser plasma interaction processes are at play and require further investigation which is currently undergoing.

7.2.2   Dependence on pulse duration

The dependence of laser driven ion beams from μm targets has been investigated [130]. It is shown that the shortest pulse duration is not necessarily best for highest ion energies. Higher ion energies can be achieved by increasing the pulse duration for a given laser energy (i.e., reduced incident intensity) up to an optimum value. Typically, for μm targets, the optimum pulse duration is in the order of 100s femtoseconds. In a simple picture, this behavior can be understood as follows. Shorter pulse duration means higher laser intensity. It could yield higher ion energies provided an infinitely acceleration time (c.f. Eq. 2.52). While, the reduction of pulse duration also means a reduction of the acceleration time so that the ions can not reach the final energy $E_{i,\infty}$. On the other hand, a smaller intensity with a longer duration can result in higher ion energies, i.e., the optimum pulse duration for a given laser energy.

Here, the pulse dependence from nanometer thin foils is presented. By changing second order group delay dispersion GDD_2 of DAZZLER device in ATLAS laser system (see Sec. 3.1.1), the pulse duration τ_L was adjusted in the range of 30-300 fs. The relationship between modified GDD_2 and τ_L for a uncharted Gaussian pulse can be expressed as

$$\tau_L = \tau_{L0} \sqrt{1 + (4\ln 2 \frac{GDD_2}{\tau_0^2})^2} \qquad (7.1)$$

where $\tau_{L0} = 30$ fs corresponds to the initial laser pulse duration presented here.

The results from 7.5 nm DLC foils under normal incidence are shown in Fig. 7.5. As a comparison, the results from 5 μm thick titanium foils were shown as well, which were obtained with 45° incident angle and without the DPM setup (with a laser energy of 0.8 J). As shown in Fig. 7.5 (a), for 5 μm thick titanium foils, the minimum energy is obtained with the initial pulse duration ($GDD_2 = 0$ fs^2) and optimum proton energies were observed when changing GDD_2 to larger values (~ 2000 fs^2) in both polarities (positive and negative), in other words, with longer pulse durations as discussed above. While for 7.5 nm thin DLC foils, the obtained proton energy decreases with increasing GDD_2 values. The best performance is obtained with $GDD_2 = 0$ fs^2, i.e., with initial pulse duration $\tau_{L0} = 30$ fs.

Inserting the GDD_2 to Eq. 7.1, the corresponding pulse duration dependence is plotted in Fig. 7.5 (b). The optimum pulse duration for 5 μm thick titanium targets is $\sim$190 fs. While, for 7.5 nm DLC foils, the highest proton energy is obtained with the shortest pulse duration used in the experiment, the optimum pulse duration is therefore close to or even below 30 fs. The optimum duration is shifted to smaller values as compared to μm thick targets.

Based on the analytical model of Schreiber *et al* [130], one could combine Eq. 2.51 and Eq. 2.53 and obtains a corresponding optimum duration τ_L^{opt} for ion acceleration as [229]

$$\tau_L^{opt} \cong 2.55\tau_0 = \frac{2.55B}{v(\infty)} \qquad (7.2)$$

The reduction of the optimum pulse duration can be described by Eq. 7.2. The optimum pulse duration τ_L^{opt} scales linearly with the transverse size of electron cloud B. Our experimental results show that the optimum pulse duration τ_L^{opt} is reduced for thinner targets. The solid curves in Fig. 7.5 (b) show the predicted maximum proton energies for the two experimental cases and in reasonable agreement with the experimental data, presenting optimum pulse duration of 170 fs for 5 μm titanium targets and 80 fs for 7.5 nm DLC foils. These values suggest electron cloud radii of $B = 3.3$ μm and $B = 1.5$ μm for 5 μm and 7.5 nm targets, respectively.
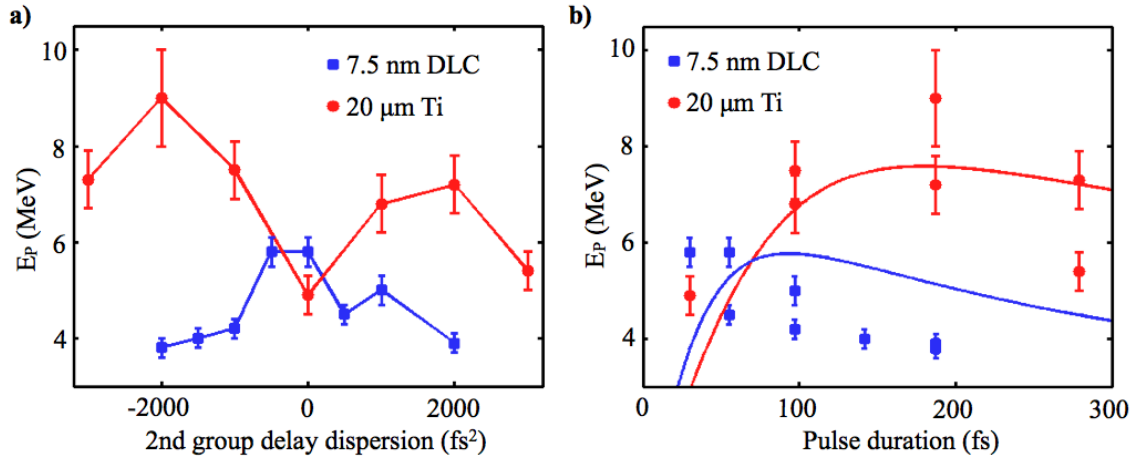
Fig. 7.5 | (a) Measured maximum proton energy E_p plotted as a function of adjusted second order group delay dispersion for 7.5 nm DLC foils and 5 μm thick titanium targets. (b) Dependence of E_p on corresponding pulse duration. The solid curves show the theoretical prediction of the analytical model [130]. The blue curve corresponds to $B = 1.5$ μm, $E_L = 0.4$ J and $f = 0.2$. The red curve corresponds to $B = 3.3$ μm, $E_L = 0.8$ J and $f = 0.25$ (c.f. Eq. 2.53). Both represent the experimental parameters for different targets. And the vertical errorbar denotes the systematic uncertainty of the spectrometer.

7.3   Summary

In summary, studying laser driven ion acceleration from nm thin foils with small scale lasers and in combination with complementary diagnostics enables access to the rich physics at play. The involved processes are certainly complicated than simple models that

are not capable of getting sufficiently details to grasp the required complexity. However, the dependence of proton energies on absorption and pulse duration in terms of general trend is reflected in experiments and model, allowing first conclusions:

1) The absorbed laser energy is more important than incident laser intensity alone.

2) The reduction of optimum pulse duration from nanometer thin foils is accompanied by the reduction of transverse spread of electrons. The presented experimental results are valuable for further optimization of laser driven ion acceleration.

Chapter 8

Summary and Outlook

8.1 Summary and Conclusions

In the framework of this thesis, laser driven ion acceleration from nano-targets has been investigated. A set of experiments have been discussed to advance the understanding of the fundamental physics of laser driven ion acceleration and also demonstrate the feasibility of a compact laser-driven beamline for radiobiological studies.

One important result of this thesis is the first demonstration of a compacts laser driven proton beamline based on a table-top laser system such as the ATLAS laser system in Garching. The experiment has been presented in Chap. 4. By combining nanometer thin targets and advanced beam optics, laser driven proton bunches with single shot ns duration and high single shot pulse dose of few Gy have been achieved experimentally for the first time. The obtained RBE in the experiments are compared to established data using conventional beams at comparable proton energies, showing no noticeable difference in biological effects even with the extremely single shot dose rates of 10^9-10^{10} Gy/s. The experimental results are published in [86].

The observed high single shot dose motivates the investigation on the underlying physics. The relevant experiment has been presented in Chap. 5. Here, a detailed experimental investigation on the divergence of laser driven proton beams from nanometer thin targets is conducted using the ATLAS laser system. A novel WASP setup is employed, enabling detection of the angularly-resolved energy distribution of protons. Well-collimated proton beams with extremely small divergence of 2° has been demonstrated experimentally for the first time. The obtained divergence values are found to be one order of magnitude smaller than reported values from μm targets, showing a tendency of reducing divergence with decreasing of target thickness from μm to nm scale. Moreover, the divergence can be further optimized by adjusting the focal spot size. 2D PIC simu-

lations were performed with the KLAP code, showing that the small divergence results from a steep longitudinal density gradient which seems representative for nm thin foils. This hypothesis is supported by an analytical model. Furthermore, the analytical model suggests that the collimation feature may arise from an exponentially decaying transverse profile at the rear side of the targets. The experimental results and interpretations are published in [87].

The third experiment presented in this thesis (Chap. 6) was conducted with the Astra Gemini laser system at the RAL in the UK addressing an advanced method for laser driven ion acceleration. The presented experiment has demonstrated for the first time that ion acceleration can be improved by exploiting relativistic nonlinearities in a controlled NCD plasma that constituted by micrometer thick CNF targets. 3D PIC simulation reveal that the incident laser pulse undergoes strong relativistic self-focusing, self-phase-modulation and relativistic induced transparency in the NCD plasma, yielding a significantly increased peak intensity with a steep rise edge. These superior pulse properties are ideally suitable to favor RPA and is further supported by the experimental measurements of transmitted pulse profiles from freestanding CNF targets. By attaching a CNF target onto a nm thin DLC foil, a significant enhancement of carbon energy up to threefold is observed experimentally for circular polarization. To date, the observed maximum carbon energy of ~20 MeV/u is the highest value demonstrated for a Gemini-class laser system. Also, the carbon ions are found to be preferentially accelerated with non-exponential spectral shape, consisting with an increased RPA contribution to the overall acceleration. This interpretation is confirmed by 3D PIC simulations. With parameters representing the experimental ones, the simulation results show that the observed enhancement of the carbon energy is primarily due to relativistic self-focusing. Meanwhile, the steep rise edge give rise to a slower decompression of the foil and therefore an increased RPA contribution. When applying this method with linearly polarized laser pulses, significant enhanced proton energy (up to 2.4×) as compared to single DLC foils was observed along with increased electron temperature. This indicates a strong enhancement on the accelerating field resulting from relativistic self-focusing in the NCD plasma and is consistent with the measurements of electron energy distribution.

In the last part of this thesis (Chap. 7), the experimental results from nanometer thin foils were summarized. The first set of experiments were conducted with the ATLAS laser system. Enhanced proton acceleration with energies up to 6 MeV from nanometer thin DLC foils were observed with a moderate laser intensity of $5 \times 10^{18} W/cm^2$. The measurements show that there is a direct correlation between laser absorption to the observed proton energy. Here, the laser absorption is determined by parallel measurements of laser transmission and reflection rates. The second part of this chapter is devoted to the inves-

tigation on the dependence of pulse duration of nanometer thin foils. An optimum pulse duration of ~ 30 fs was observed with a given energy of ATLAS laser system as compared to μm thick titanium targets (190 fs). The experimental observation is attributed to a reduced transverse electron spread owing to the reduction on the target thickness.

8.2 Outlook and Future Perspectives

8.2.1 Exploiting relativistic nonlinearities for ion acceleration and potential pulse cleaning technique

The current beam qualities of laser driven ion beams are not yet in the necessary range for medical applications. The experimental results presented in Chap. 6 suggest that exploiting relativistic nonlinearities in NCD plasmas is one promising route towards high energetic ion beams. The preliminary experimental investigations have shown significant energy enhancement for both circular and linear polarizations. The possibility of producing peaked ion spectra has been verified experimentally. Moreover, the experiments imply that the ultimate energy enhancement, as indicated by PIC simulations (c.f. Fig. 6.6), was not yet achieved. In the near future, further studies will be performed in an experiment with upgraded ATLAS 300 laser system (6 J, 25 fs, 240TW).

The potential use of improving laser contrast by exploiting relativistic nonlinearities in NCD plasmas could be another interesting prospect. The temporal contrast of laser pulses is one of the most relevant parameters for laser-plasma experiments, especially for nanometer thin foils. In fact, large efforts have been dedicated to various techniques to achieve a clean laser pulse, such as cross-polarized wave generation (XPW) [230], optical parametric amplification (OPA) [231], and plasma mirror (PM) (see Sec. 3.1.1). None of these techniques has capability of providing a high contrast in the temporal region within ~1 ps before the main pulse. As shown in Chap. 6, the introduction of CNF targets resulted in a substantially steepened laser rising edge, i.e., an improved laser contrast on a few-cycle level. Future experimental investigation along such direction might establish a fantastic pulse cleaning technology which allows providing ultra-contrast high-intensity laser pulses.

8.2.2 NCD nano-targets for ion acceleration

Another promising route to improve ion acceleration would be the use of NCD targets. As shown in Sec. 1.1, enhanced ion acceleration has been reported with NCD targets. For instance, 160 MeV proton beam was observed with NCD CH_2 targets [47]. Quasi-

monoenergetic ion beams have been demonstrated with CO_2 laser pulses interacting with NCD gas-jet [48, 49]. The nano-target introduced in this thesis, CNF targets, is one perfect NCD candidate for this purpose with laser centre wavelength at 800 nm.

8.2.3 Foreseen high-quality ion beams from upgraded ATLAS laser

The ATLAS laser system is completely reconstructed and upgraded along in the past few years with the construction of new research infrastructure laboratory for extreme (LEX) photonics in Garching [232]. In the current stage, the ATLAS laser system is upgraded to a final energy of 6 J before compression and a pulse duration of 25 fs (ATLAS 300). And the next upgrade aims at the final energy of 60 J before compression and a pulse duration of ~25 fs (ATLAS 3000) with the centre for advanced laser applications (CALA) [233].

	E_L (on target)	τ_L	I_0 (W/cm^2)	d (nm)	E_p (MeV)	θ_{mod}	θ_{pic}
ATLAS 100	0.4 J	30 fs	8×10^{19}	10	6	3.3°	\
ATLAS 300	4 J	25 fs	1×10^{21}	35	35	6°	4°
ATLAS 3000	40 J	25 fs	1×10^{22}	110	165	11°	4°

Tab. 8.1 | Laser parameters and predicted ion beam outcomes for different ATLAS stages is listed. For ATLAS 100, the laser parameters and the values of maximum proton energy E_p, half angle of divergence θ and target thickness d are extracted from the experimental results in Chap. 5. For ATLAS 300 and ATLAS 3000, E_p is obtained from Eq. 2.53 with a constant laser absorption rate $f = 25\%$, θ_{mod} is obtained based on the analytical model described in Sec. 5.4, θ_{pic} is extracted from PIC simulations (c.f. Fig. 8.1) and d is estimated from Eq. 2.57. The total transmission of the compressor plus the beamline to target chamber is assumed to be 67% provided that no DPM is used.

Assuming the laser pulse is focused by a F2 OAP parabola, and the quality of the focal spot remains similar as shown in Fig. 3.3, one obtains the laser intensities yielded by the upgraded ATLAS system as shown in Tab. 8.1. The theoretical predictions of ion beams accelerated with these laser parameters are presented as well. Proton beams with energy up to 35 MeV and with a small divergence half angle of $\theta = 6°$ is predicted with ATLAS 300, and with ATLAS 3000 much higher energetic proton beam up to 165 MeV with $\theta = 11°$ can be expected.

Taking the laser and target parameters listed in Tab. 8.1 as the inputs, 2D PIC simulations predict a maximum proton energy up to 45 MeV and 180 MeV for ATLAS 300 and ATLAS 3000 respectively (see Fig. 8.1 (a)), agreeing well with the ones derived from the analytical model presented above. Moreover, Fig. 8.1 (b) shows the corresponding angular distribution of proton beams from the simulations. With ATLAS 300, a well collimated proton beam with a constant divergence half angle of about 4° is observed with energy beyond 20 MeV. Interestingly, a small divergence of 4°, comparable to the ALTAS

300, is obtained with ATLAS 3000, which is much smaller than the expected θ_{mod} from the analytical model in Tab. 8.1. As discussed in Sec. 5.4, along with the impact of the hot electrons, a perfect divergence close to zero can be resulted from a sufficiently strong radiation pressure of the laser pulses. The incredible small divergence may assemble a result of these two process, especially when the laser intensity reaching 10^{22}W/cm^2. Further supports can be found in Fig. 8.1 (a) and (c), they show a more dominant contribution of RPA process is clearly evidenced in the peaked proton spectra and the complete separation of C^{6+} ions and protons where the fastest carbo ions indeed follow the slowest protons in the spectra peak owing to leaky light-sail regime [144].
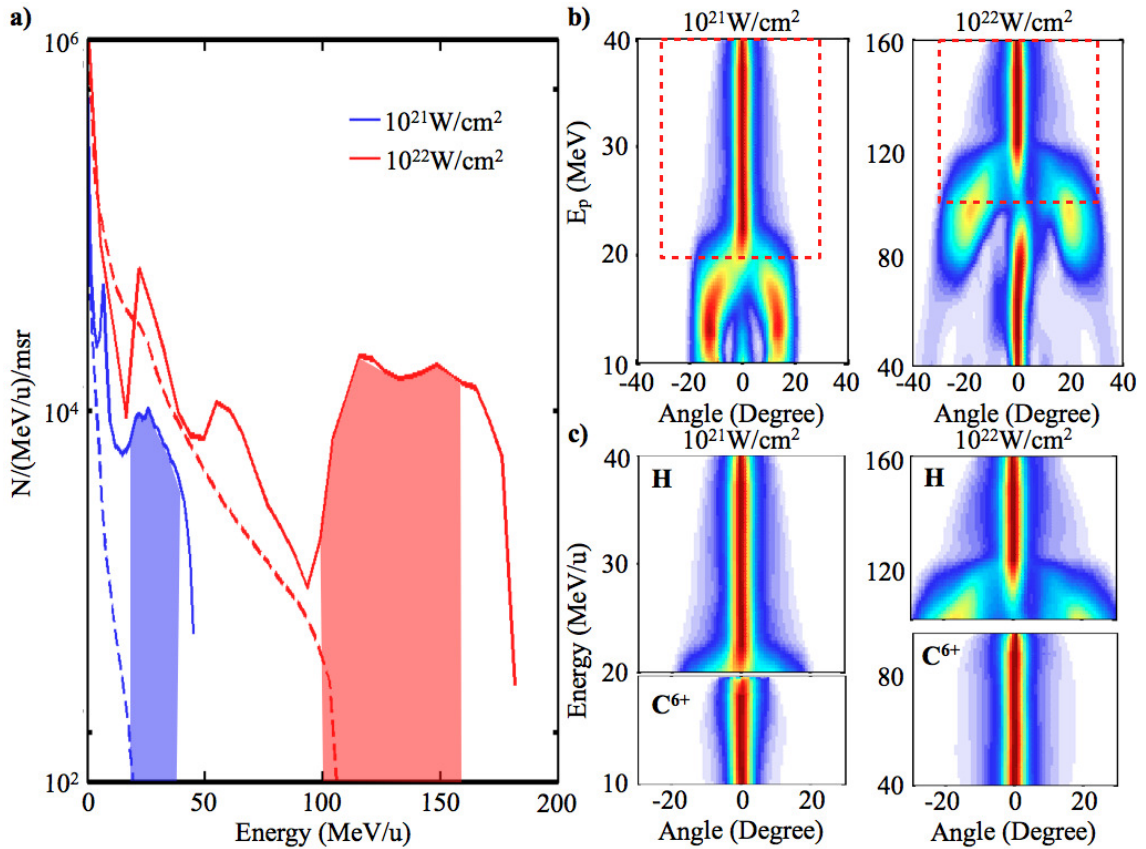

Fig. 8.1 | (a) shows proton (solid curves) and C^{6+} ions (dashed curves) spectra at $t = 80T$ from 2D PIC simulations for ATLAS 300 and ATLAS 3000, Here T corresponds to one laser cycle. Input laser and target parameters are identical to the values listed in Tab. 8.1. (b) shows the corresponding angular distribution of protons after normalization, presenting collimated beam features in different energy ranges as marked by red rectangles. The energy range is indicated by the colored areas in (a) as well. Furthermore, the angular distribution of protons and carbon ions were plotted with same energy unit MeV per nucleon in (c). Courtesy of H. Wang, Helmoholtz Institute Jena.

Furthermore, one could estimate CNF thickness for double-layer target configuration (CNF + DLC) for the upgraded laser system, which would be very useful for the future

studies presented in Sec. 8.2.1. According to Eq. 2.36, CNF targets with thickness $d = 10$ μm and $d = 18$ μm would be appropriate for ATLAS 300 and ATLAS 3000, respectively. The corresponding simulations are shown in Fig. 8.2. A significant enhancement of maximum energy by a factor of ~2 both for protons and carbon ions is clearly shown with ATLAS 300 and with ATLAS 3000 as well. Quasi-monoenergetic proton beams with maximum energy up to 370 MeV are expected and an ultimate maximum carbon energy of 2.5 GeV is predicted with the aid of double-layer target configuration with future ATLAS 3000. These values could be in principle satisfy the requirements for most of the applications (e.g., ~200 MeV proton beam for deep-seated ion beam therapy) and encourage the investigation in further application stages. For example, considering the fist biomedical studies with the ATLAS Laser as illustrated in Chap. 4, the next step would be to adapt the prototype system to the studies of *in vivo* experiments (i.e., animal irradiation) with the upgraded laser. However, these predictions are very advisable but they must be treated with case, as simulations require experimental verifications. In any case, we are expecting very interesting times in future.
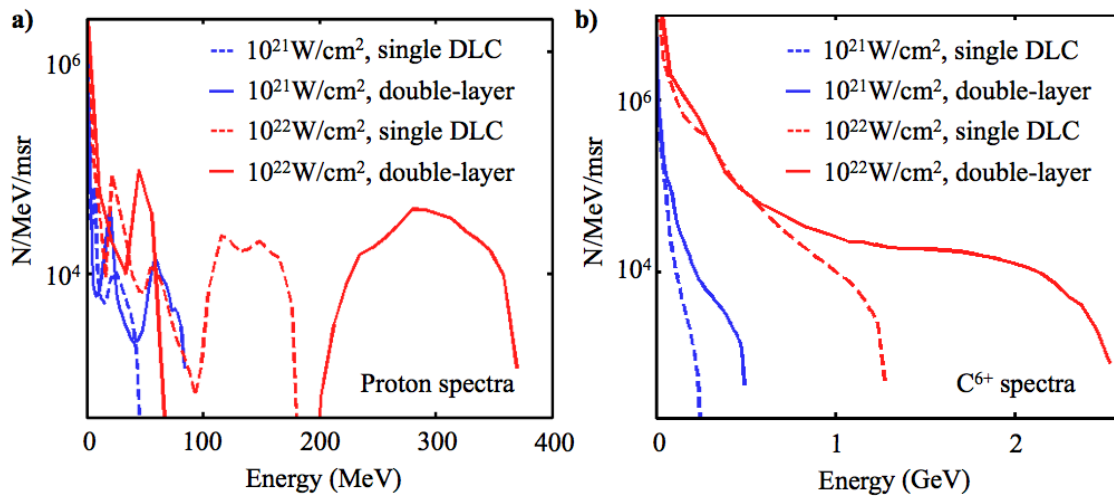

Fig. 8.2 | 2D PIC simulation results of proton (a) and C^{6+} spectra (b) at $t = 80T$ for ATLAS 300 and ATLAS 3000 with identical laser and target parameters from Tab. 8.1. Here T corresponds to one laser cycle. As a comparison, the results from single DLC foils are plotted in the dashed curves as well. Courtesy of H. Wang, Helmoholtz Institute Jena.

Bibliography

[1] T. H. Maiman. Stimulated Optical Radiation in Ruby. *Nature*, 187(4736):493–494, 1960.

[2] JOHN NUCKOLLS, LOWELL WOOD, ALBERT THIESSEN, and GEORGE ZIMMERMAN. Laser Compression of Matter to Super-High Densities: Thermonuclear (CTR) Applications. *Nature*, 239(5368):139–142, 1972.

[3] D. W. Forslund and J. U. Brackbill. Magnetic-field-induced surface transport on laser-irradiated foils. *Phys. Rev. Lett.*, 48:1614–1617, 1982.

[4] S. J. Gitomer, R. D. Jones, F. Begay, A. W. Ehler, J. F. Kephart, and R. Kristal. Fast ions and hot electrons in the laser-plasma interaction. *Physics of Fluids (1958-1988)*, 29(8):2679–2688, 1986.

[5] Donna Strickland and Gerard Mourou. Compression of amplified chirped optical pulses. *Optics Communications*, 55(6):447 – 449, 1985.

[6] ELI. URL `http://www.eli-beams.eu/`.

[7] Gerard A. Mourou, Toshiki Tajima, and Sergei V. Bulanov. Optics in the relativistic regime. *Rev. Mod. Phys.*, 78:309–371, 2006.

[8] A. P. Fews, P. A. Norreys, F. N. Beg, A. R. Bell, A. E. Dangor, C. N. Danson, P. Lee, and S. J. Rose. Plasma ion emission from high intensity picosecond laser pulse interactions with solid targets. *Phys. Rev. Lett.*, 73:1801–1804, 1994.

[9] E. L. Clark, K. Krushelnick, J. R. Davies, M. Zepf, M. Tatarakis, F. N. Beg, A. Machacek, P. A. Norreys, M. I. K. Santala, I. Watts, and A. E. Dangor. Measurements of energetic proton transport through magnetized plasma from intense laser interactions with solids. *Phys. Rev. Lett.*, 84:670–673, 2000.

[10] R. A. Snavely, M. H. Key, S. P. Hatchett, T. E. Cowan, M. Roth, T. W. Phillips, M. A. Stoyer, E. A. Henry, T. C. Sangster, M. S. Singh, S. C. Wilks, A. MacKinnon,

A. Offenberger, D. M. Pennington, K. Yasuike, A. B. Langdon, B. F. Lasinski, J. Johnson, M. D. Perry, and E. M. Campbell. Intense high-energy proton beams from petawatt-laser irradiation of solids. *Phys. Rev. Lett.*, 85:2945–2948, 2000.

[11] A. Maksimchuk, S. Gu, K. Flippo, D. Umstadter, and V. Yu. Bychenkov. Forward ion acceleration in thin films driven by a high-intensity laser. *Phys. Rev. Lett.*, 84: 4108–4111, 2000.

[12] K Krushelnick, E L Clark, M Zepf, J R Davies, F N Beg, A Machacek, M I K Santala, M Tatarakis, I Watts, P A Norreys, and A E Dangor. Energetic proton production from relativistic laser interaction with high density plasmas. *Physics of Plasmas (1994-present)*, 7(5), 2000.

[13] M. Zepf, E. L. Clark, F. N. Beg, R. J. Clarke, A. E. Dangor, A. Gopal, K. Krushelnick, P. A. Norreys, M. Tatarakis, U. Wagner, and M. S. Wei. Proton acceleration from high-intensity laser interactions with thin foil targets. *Phys. Rev. Lett.*, 90: 064801, 2003.

[14] E. Brambrink, J. Schreiber, T. Schlegel, P. Audebert, J. Cobble, J. Fuchs, M. Hegelich, and M. Roth. Transverse characteristics of short-pulse laser-produced ion beams: A study of the acceleration dynamics. *Phys. Rev. Lett.*, 96:154801, 2006.

[15] M. Borghesi, A. J. Mackinnon, D. H. Campbell, D. G. Hicks, S. Kar, P. K. Patel, D. Price, L. Romagnani, A. Schiavi, and O. Willi. Multi-mev proton source investigations in ultraintense laser-foil interactions. *Phys. Rev. Lett.*, 92:055003, 2004.

[16] J. Schreiber, M. Kaluza, F. Grüner, U. Schramm, B.M. Hegelich, J. Cobble, M. Geissler, E. Brambrink, J. Fuchs, P. Audebert, D. Habs, and K. Witte. Source-size measurements and charge distributions of ions accelerated from thin foils irradiated by high-intensity laser pulses. *Applied Physics B*, 79(8):1041–1045, 2004.

[17] T. E. Cowan, J. Fuchs, H. Ruhl, A. Kemp, P. Audebert, M. Roth, R. Stephens, I. Barton, A. Blazevic, E. Brambrink, J. Cobble, J. Fernández, J.-C. Gauthier, M. Geissel, M. Hegelich, J. Kaae, S. Karsch, G. P. Le Sage, S. Letzring, M. Manclossi, S. Meyroneinc, A. Newkirk, H. Pépin, and N. Renard-LeGalloudec. Ultralow emittance, multi-mev proton beams from a laser virtual-cathode plasma accelerator. *Phys. Rev. Lett.*, 92:204801, 2004.

[18] M Borghesi, J Fuchs, SV Bulanov, AJ Mackinnon, PK Patel, and M Roth. Fast ion generation by high-intensity laser irradiation of solid targets and applications. *Fusion Science and Technology*, 49(3):412–439, 2006.

[19] Hiroyuki Daido, Mamiko Nishiuchi, and Alexander S Pirozhkov. Review of laser-driven ion sources and their applications. *Reports on Progress in Physics*, 75(5): 056401, 2012.

[20] Andrea Macchi, Marco Borghesi, and Matteo Passoni. Ion acceleration by super-intense laser-plasma interaction. *Rev. Mod. Phys.*, 85:751–793, 2013.

[21] M. Hegelich, S. Karsch, G. Pretzler, D. Habs, K. Witte, W. Guenther, M. Allen, A. Blazevic, J. Fuchs, J. C. Gauthier, M. Geissel, P. Audebert, T. Cowan, and M. Roth. Mev ion jets from short-pulse-laser interaction with thin foils. *Phys. Rev. Lett.*, 89:085002, 2002.

[22] Matthew Allen, Pravesh K. Patel, Andrew Mackinnon, Dwight Price, Scott Wilks, and Edward Morse. Direct experimental evidence of back-surface ion acceleration from laser-irradiated gold foils. *Phys. Rev. Lett.*, 93:265004, 2004.

[23] S. A. Gaillard, T. Kluge, K. A. Flippo, M. Bussmann, B. Gall, T. Lockard, M. Geissel, D. T. Offermann, M. Schollmeier, Y. Sentoku, and T. E. Cowan. Increased laser-accelerated proton energies via direct laser-light-pressure acceleration of electrons in microcone targetsa). *Physics of Plasmas (1994-present)*, 18(5): 056710, 2011.

[24] J Fuchs, P Antici, E D'Humieres, E Lefebvre, M Borghesi, E Brambrink, C A Cecchetti, M Kaluza, V Malka, M Manclossi, S Meyroneinc, P Mora, J Schreiber, T Toncian, H Pepin, and P Audebert. Laser-driven proton scaling laws and new paths towards energy increase. *Nat Phys*, 2(1):48–54, 2006.

[25] E. L. Clark, K. Krushelnick, M. Zepf, F. N. Beg, M. Tatarakis, A. Machacek, M. I. K. Santala, I. Watts, P. A. Norreys, and A. E. Dangor. Energetic heavy-ion and proton generation from ultraintense laser-plasma interactions with solids. *Phys. Rev. Lett.*, 85:1654–1657, 2000.

[26] P. McKenna, K. W. D. Ledingham, J. M. Yang, L. Robson, T. McCanny, S. Shimizu, R. J. Clarke, D. Neely, K. Spohr, R. Chapman, R. P. Singhal, K. Krushelnick, M. S. Wei, and P. A. Norreys. Characterization of proton and heavier ion acceleration in ultrahigh-intensity laser interactions with heated target foils. *Phys. Rev. E*, 70:036405, 2004.

[27] H Schwoerer, S Pfotenhauer, O Jackel, K.-U. Amthor, B Liesfeld, W Ziegler, R Sauerbrey, K W D Ledingham, and T Esirkepov. Laser-plasma acceleration of quasi-monoenergetic protons from microstructured targets. *Nature*, 439(7075): 445–448, 2006.

[28] Toma Toncian, Marco Borghesi, Julien Fuchs, Emmanuel d'Humières, Patrizio Antici, Patrick Audebert, Erik Brambrink, Carlo Alberto Cecchetti, Ariane Pipahl, Lorenzo Romagnani, and Oswald Willi. Ultrafast laser-driven microlens to focus and energy-select mega-electron volt protons. *Science*, 312(5772):410–413, 2006.

[29] B M Hegelich, B J Albright, J Cobble, K Flippo, S Letzring, M Paffett, H Ruhl, J Schreiber, R K Schulze, and J C Fernández. Laser acceleration of quasi-monoenergetic MeV ion beams. *Nature*, 439(7075):441–444, 2006.

[30] L Robson, P T Simpson, R J Clarke, K W D Ledingham, F Lindau, O Lundh, T McCanny, P Mora, D Neely, C.-G. Wahlstrom, M Zepf, and P McKenna. Scaling of proton acceleration driven by petawatt-laser-plasma interactions. *Nat Phys*, 3(1): 58–62, 2007.

[31] A. J. Mackinnon, Y. Sentoku, P. K. Patel, D. W. Price, S. Hatchett, M. H. Key, C. Andersen, R. Snavely, and R. R. Freeman. Enhancement of proton acceleration by hot-electron recirculation in thin foils irradiated by ultraintense laser pulses. *Phys. Rev. Lett.*, 88:215006, 2002.

[32] M. Kaluza, J. Schreiber, M. I. K. Santala, G. D. Tsakiris, K. Eidmann, J. Meyer-ter Vehn, and K. J. Witte. Influence of the laser prepulse on proton acceleration in thin-foil experiments. *Phys. Rev. Lett.*, 93:045003, 2004.

[33] D. Neely, P. Foster, A. Robinson, F. Lindau, O. Lundh, A. Persson, C.-G. Wahlstrom, and P. McKenna. Enhanced proton beams from ultrathin targets driven by high contrast laser pulses. *Applied Physics Letters*, 89(2):021502, 2006.

[34] P. Antici, J. Fuchs, E. d'Humières, E. Lefebvre, M. Borghesi, E. Brambrink, C. A. Cecchetti, S. Gaillard, L. Romagnani, Y. Sentoku, T. Toncian, O. Willi, P. Audebert, and H. Pépin. Energetic protons generated by ultrahigh contrast laser pulses interacting with ultrathin targets. *Physics of Plasmas (1994-present)*, 14 (3):030701, 2007.

[35] A. Henig, D. Kiefer, K. Markey, D. C. Gautier, K. A. Flippo, S. Letzring, R. P. Johnson, T. Shimada, L. Yin, B. J. Albright, K. J. Bowers, J. C. Fernández,

S. G. Rykovanov, H.-C. Wu, M. Zepf, D. Jung, V. Kh. Liechtenstein, J. Schreiber, D. Habs, and B. M. Hegelich. Enhanced laser-driven ion acceleration in the relativistic transparency regime. *Phys. Rev. Lett.*, 103:045002, 2009.

[36] S. Steinke, A. Henig, M. Schnürer, T. Sokollik, P.V. Nickles, D. Jung, D. Kiefer, R. Hörlein, J. Schreiber, T. Tajima, X.Q. Yan, M. Hegelich, J. Meyer-ter Vehn, W. Sandner, and D. Habs. Efficient ion acceleration by collective laser-driven electron dynamics with ultra-thin foil targets. *Laser and Particle Beams*, 28:215–221, 2010.

[37] D. Jung, L. Yin, D. C. Gautier, H.-C. Wu, S. Letzring, B. Dromey, R. Shah, S. Palaniyappan, T. Shimada, R. P. Johnson, J. Schreiber, D. Habs, J. C. Fernández, B. M. Hegelich, and B. J. Albright. Laser-driven 1gev carbon ions from preheated diamond targets in the break-out afterburner regime. *Physics of Plasmas (1994-present)*, 20(8):083103, 2013.

[38] A Andreev, T Ceccotti, A Levy, K Platonov, and Ph Martin. Divergence of fast ions generated by interaction of intense ultra-high contrast laser pulses with thin foils. *New Journal of Physics*, 12(4):045007, 2010.

[39] A. Henig, S. Steinke, M. Schnürer, T. Sokollik, R. Hörlein, D. Kiefer, D. Jung, J. Schreiber, B. M. Hegelich, X. Q. Yan, J. Meyer-ter Vehn, T. Tajima, P. V. Nickles, W. Sandner, and D. Habs. Radiation-pressure acceleration of ion beams driven by circularly polarized laser pulses. *Phys. Rev. Lett.*, 103:245003, 2009.

[40] D. Jung, L. Yin, B. J. Albright, D. C. Gautier, R. Hörlein, D. Kiefer, A. Henig, R. Johnson, S. Letzring, S. Palaniyappan, R. Shah, T. Shimada, X. Q. Yan, K. J. Bowers, T. Tajima, J. C. Fernández, D. Habs, and B. M. Hegelich. Monoenergetic ion beam generation by driving ion solitary waves with circularly polarized laser light. *Phys. Rev. Lett.*, 107:115002, 2011.

[41] S. Steinke, P. Hilz, M. Schnürer, G. Priebe, J. Bränzel, F. Abicht, D. Kiefer, C. Kreuzer, T. Ostermayr, J. Schreiber, A. A. Andreev, T. P. Yu, A. Pukhov, and W. Sandner. Stable laser-ion acceleration in the light sail regime. *Phys. Rev. ST Accel. Beams*, 16:011303, 2013.

[42] S. Kar, K. F. Kakolee, B. Qiao, A. Macchi, M. Cerchez, D. Doria, M. Geissler, P. McKenna, D. Neely, J. Osterholz, R. Prasad, K. Quinn, B. Ramakrishna, G. Sarri, O. Willi, X. Y. Yuan, M. Zepf, and M. Borghesi. Ion acceleration in multispecies

targets driven by intense laser radiation pressure. *Phys. Rev. Lett.*, 109:185006, 2012.

[43] K. Krushelnick, E. L. Clark, Z. Najmudin, M. Salvati, M. I. K. Santala, M. Tatarakis, A. E. Dangor, V. Malka, D. Neely, R. Allott, and C. Danson. Multi-mev ion production from high-intensity laser interactions with underdense plasmas. *Phys. Rev. Lett.*, 83:737–740, 1999.

[44] M. S. Wei, S. P. D. Mangles, Z. Najmudin, B. Walton, A. Gopal, M. Tatarakis, A. E. Dangor, E. L. Clark, R. G. Evans, S. Fritzler, R. J. Clarke, C. Hernandez-Gomez, D. Neely, W. Mori, M. Tzoufras, and K. Krushelnick. Ion acceleration by collisionless shocks in high-intensity-laserÐunderdense-plasma interaction. *Phys. Rev. Lett.*, 93:155003, 2004.

[45] L. Willingale, S. P. D. Mangles, P. M. Nilson, R. J. Clarke, A. E. Dangor, M. C. Kaluza, S. Karsch, K. L. Lancaster, W. B. Mori, Z. Najmudin, J. Schreiber, A. G. R. Thomas, M. S. Wei, and K. Krushelnick. Collimated multi-mev ion beams from high-intensity laser interactions with underdense plasma. *Phys. Rev. Lett.*, 96: 245002, 2006.

[46] Y. Fukuda, A. Ya. Faenov, M. Tampo, T. A. Pikuz, T. Nakamura, M. Kando, Y. Hayashi, A. Yogo, H. Sakaki, T. Kameshima, A. S. Pirozhkov, K. Ogura, M. Mori, T. Zh. Esirkepov, J. Koga, A. S. Boldarev, V. A. Gasilov, A. I. Magunov, T. Yamauchi, R. Kodama, P. R. Bolton, Y. Kato, T. Tajima, H. Daido, and S. V. Bulanov. Energy increase in multi-mev ion acceleration in the interaction of a short pulse laser with a cluster-gas target. *Phys. Rev. Lett.*, 103:165002, 2009.

[47] B. M. Hegelich, D. Jung, B. J. Albright, M. Cheung, B. Dromey, D. C. Gautier, C. Hamilton, S. Letzring, R. Munchhausen, S. Palaniyappan, R. Shah, H. C. Wu, L. Yin, and J. C. Fernández. 160 mev laser-accelerated protons from ch2 nano-targets for proton cancer therapy. *arXiv preprint arXiv:1310.8650*, 2013.

[48] Charlotte A. J. Palmer, N. P. Dover, I. Pogorelsky, M. Babzien, G. I. Dudnikova, M. Ispiriyan, M. N. Polyanskiy, J. Schreiber, P. Shkolnikov, V. Yakimenko, and Z. Najmudin. Monoenergetic proton beams accelerated by a radiation pressure driven shock. *Phys. Rev. Lett.*, 106:014801, 2011.

[49] Dan Haberberger, Sergei Tochitsky, Frederico Fiuza, Chao Gong, Ricardo A Fonseca, Luis O Silva, Warren B Mori, and Chan Joshi. Collisionless shocks in laser-

produced plasma generate monoenergetic high-energy proton beams. *Nat Phys*, 8 (1):95–99, 2012.

[50] M. Borghesi, D. H. Campbell, A. Schiavi, M. G. Haines, O. Willi, A. J. MacKinnon, P. Patel, L. A. Gizzi, M. Galimberti, R. J. Clarke, F. Pegoraro, H. Ruhl, and S. Bulanov. Electric field detection in laser-plasma interaction experiments via the proton imaging technique. *Physics of Plasmas (1994-present)*, 9(5):2214–2220, 2002.

[51] M. Roth, A. Blazevic, M. Geissel, T. Schlegel, T. E. Cowan, M. Allen, J.-C. Gauthier, P. Audebert, J. Fuchs, J. Meyer-ter Vehn, M. Hegelich, S. Karsch, and A. Pukhov. Energetic ions generated by laser pulses: A detailed study on target properties. *Phys. Rev. ST Accel. Beams*, 5:061301, 2002.

[52] J. A. Cobble, R. P. Johnson, T. E. Cowan, N. Renard-Le Galloudec, and M. Allen. High resolution laser-driven proton radiography. *Journal of Applied Physics*, 92 (4):1775–1779, 2002.

[53] M. Borghesi, S. Bulanov, D. H. Campbell, R. J. Clarke, T. Zh. Esirkepov, M. Galimberti, L. A. Gizzi, A. J. MacKinnon, N. M. Naumova, F. Pegoraro, H. Ruhl, A. Schiavi, and O. Willi. Macroscopic evidence of soliton formation in multiterawatt laser-plasma interaction. *Phys. Rev. Lett.*, 88:135002, 2002.

[54] L. Romagnani, S. V. Bulanov, M. Borghesi, P. Audebert, J. C. Gauthier, K. Löwenbrück, A. J. Mackinnon, P. Patel, G. Pretzler, T. Toncian, and O. Willi. Observation of collisionless shocks in laser-plasma experiments. *Phys. Rev. Lett.*, 101:025004, 2008.

[55] M. Borghesi, L. Romagnani, A. Schiavi, D. H. Campbell, M. G. Haines, O. Willi, A. J. Mackinnon, M. Galimberti, L. Gizzi, R. J. Clarke, and S. Hawkes. Measurement of highly transient electrical charging following high-intensity laser-solid interaction. *Applied Physics Letters*, 82(10):1529–1531, 2003.

[56] L. Romagnani, J. Fuchs, M. Borghesi, P. Antici, P. Audebert, F. Ceccherini, T. Cowan, T. Grismayer, S. Kar, A. Macchi, P. Mora, G. Pretzler, A. Schiavi, T. Toncian, and O. Willi. Dynamics of electric fields driving the laser acceleration of multi-mev protons. *Phys. Rev. Lett.*, 95:195001, 2005.

[57] P. M. Nilson, L. Willingale, M. C. Kaluza, C. Kamperidis, S. Minardi, M. S. Wei, P. Fernandes, M. Notley, S. Bandyopadhyay, M. Sherlock, R. J. Kingham,

M. Tatarakis, Z. Najmudin, W. Rozmus, R. G. Evans, M. G. Haines, A. E. Dangor, and K. Krushelnick. Magnetic reconnection and plasma dynamics in two-beam laser-solid interactions. *Phys. Rev. Lett.*, 97:255001, 2006.

[58] C. A. Cecchetti, M. Borghesi, J. Fuchs, G. Schurtz, S. Kar, A. Macchi, L. Romagnani, P. A. Wilson, P. Antici, R. Jung, J. Osterholtz, C. A. Pipahl, O. Willi, A. Schiavi, M. Notley, and D. Neely. Magnetic field measurements in laser-produced plasmas via proton deflectometry. *Physics of Plasmas (1994-present)*, 16(4):043102, 2009.

[59] C. A. J. Palmer, J. Schreiber, S. R. Nagel, N. P. Dover, C. Bellei, F. N. Beg, S. Bott, R. J. Clarke, A. E. Dangor, S. M. Hassan, P. Hilz, D. Jung, S. Kneip, S. P. D. Mangles, K. L. Lancaster, A. Rehman, A. P. L. Robinson, C. Spindloe, J. Szerypo, M. Tatarakis, M. Yeung, M. Zepf, and Z. Najmudin. Rayleigh-taylor instability of an ultrathin foil accelerated by the radiation pressure of an intense laser. *Phys. Rev. Lett.*, 108:225002, 2012.

[60] A. J. Mackinnon, P. K. Patel, M. Borghesi, R. C. Clarke, R. R. Freeman, H. Habara, S. P. Hatchett, D. Hey, D. G. Hicks, S. Kar, M. H. Key, J. A. King, K. Lancaster, D. Neely, A. Nikkro, P. A. Norreys, M. M. Notley, T. W. Phillips, L. Romagnani, R. A. Snavely, R. B. Stephens, and R. P. J. Town. Proton radiography of a laser-driven implosion. *Phys. Rev. Lett.*, 97:045001, 2006.

[61] J. R. Rygg, F. H. Séguin, C. K. Li, J. A. Frenje, M. J.-E. Manuel, R. D. Petrasso, R. Betti, J. A. Delettrez, O. V. Gotchev, J. P. Knauer, D. D. Meyerhofer, F. J. Marshall, C. Stoeckl, and W. Theobald. Proton radiography of inertial fusion implosions. *Science*, 319(5867):1223–1225, 2008.

[62] C. K. Li, F. H. Séguin, J. R. Rygg, J. A. Frenje, M. Manuel, R. D. Petrasso, R. Betti, J. Delettrez, J. P. Knauer, F. Marshall, D. D. Meyerhofer, D. Shvarts, V. A. Smalyuk, C. Stoeckl, O. L. Landen, R. P. J. Town, C. A. Back, and J. D. Kilkenny. Monoenergetic-proton-radiography measurements of implosion dynamics in direct-drive inertial-confinement fusion. *Phys. Rev. Lett.*, 100:225001, 2008.

[63] Stephen E. Bodner, Denis G. Colombant, John H. Gardner, Robert H. Lehmberg, Stephen P. Obenschain, Lee Phillips, Andrew J. Schmitt, John D. Sethian, Robert L. McCrory, Wolf Seka, Charles P. Verdon, James P. Knauer, Bedros B. Afeyan, and Howard T. Powell. Direct-drive laser fusion: Status and prospects. *Physics of Plasmas (1994-present)*, 5(5):1901–1918, 1998.

[64] R. L. McCrory, D. D. Meyerhofer, R. Betti, R. S. Craxton, J. A. Delettrez, D. H. Edgell, V. Yu. Glebov, V. N. Goncharov, D. R. Harding, D. W. Jacobs-Perkins, J. P. Knauer, F. J. Marshall, P. W. McKenty, P. B. Radha, S. P. Regan, T. C. Sangster, W. Seka, R. W. Short, S. Skupsky, V. A. Smalyuk, J. M. Soures, C. Stoeckl, B. Yaakobi, D. Shvarts, J. A. Frenje, C. K. Li, R. D. Petrasso, and F. H. Séguin. Progress in direct-drive inertial confinement fusion). *Physics of Plasmas (1994-present)*, 15(5):055503, 2008.

[65] John Lindl. Development of the indirect-drive approach to inertial confinement fusion and the target physics basis for ignition and gain. *Physics of Plasmas (1994-present)*, 2(11):3933–4024, 1995.

[66] John D. Lindl, Peter Amendt, Richard L. Berger, S. Gail Glendinning, Siegfried H. Glenzer, Steven W. Haan, Robert L. Kauffman, Otto L. Landen, and Laurence J. Suter. The physics basis for ignition using indirect-drive targets on the national ignition facility. *Physics of Plasmas (1994-present)*, 11(2):339–491, 2004.

[67] NIF. URL `https://lasers.llnl.gov/`.

[68] O A Hurricane, D A Callahan, D T Casey, P M Celliers, C Cerjan, E L Dewald, T R Dittrich, T Doppner, D E Hinkel, L F Berzak Hopkins, J L Kline, S Le Pape, T Ma, A G MacPhee, J L Milovich, A Pak, H.-S. Park, P K Patel, B A Remington, J D Salmonson, P T Springer, and R Tommasini. Fuel gain exceeding unity in an inertially confined fusion implosion. *Nature*, 506(7488):343–348, 2014.

[69] Max Tabak, James Hammer, Michael E. Glinsky, William L. Kruer, Scott C. Wilks, John Woodworth, E. Michael Campbell, Michael D. Perry, and Rodney J. Mason. Ignition and high gain with ultrapowerful lasers. *Physics of Plasmas (1994-present)*, 1(5):1626–1634, 1994.

[70] M. Roth, T. E. Cowan, M. H. Key, S. P. Hatchett, C. Brown, W. Fountain, J. Johnson, D. M. Pennington, R. A. Snavely, S. C. Wilks, K. Yasuike, H. Ruhl, F. Pegoraro, S. V. Bulanov, E. M. Campbell, M. D. Perry, and H. Powell. Fast ignition by intense laser-accelerated proton beams. *Phys. Rev. Lett.*, 86:436–439, 2001.

[71] Juan C. Fernández, J.J. Honrubia, Brian J. Albright, Kirk A. Flippo, D. Cort Gautier, Björn M. Hegelich, Mark J. Schmitt, M. Temporal, and Lin Yin. Progress and prospects of ion-driven fast ignition. *Nuclear Fusion*, 49(6):065004, 2009.

[72] P. K. Patel, A. J. Mackinnon, M. H. Key, T. E. Cowan, M. E. Foord, M. Allen, D. F. Price, H. Ruhl, P. T. Springer, and R. Stephens. Isochoric heating of solid-density matter with an ultrafast proton beam. *Phys. Rev. Lett.*, 91:125004, 2003.

[73] G. M. Dyer, A. C. Bernstein, B. I. Cho, J. Osterholz, W. Grigsby, A. Dalton, R. Shepherd, Y. Ping, H. Chen, K. Widmann, and T. Ditmire. Equation-of-state measurement of dense plasmas heated with fast protons. *Phys. Rev. Lett.*, 101: 015002, 2008.

[74] A. Pelka, G. Gregori, D. O. Gericke, J. Vorberger, S. H. Glenzer, M. M. Günther, K. Harres, R. Heathcote, A. L. Kritcher, N. L. Kugland, B. Li, M. Makita, J. Mithen, D. Neely, C. Niemann, A. Otten, D. Riley, G. Schaumann, M. Schollmeier, An. Tauschwitz, and M. Roth. Ultrafast melting of carbon induced by intense proton beams. *Phys. Rev. Lett.*, 105:265701, 2010.

[75] A. Maněić, A. Lévy, M. Harmand, M. Nakatsutsumi, P. Antici, P. Audebert, P. Combis, S. Fourmaux, S. Mazevet, O. Peyrusse, V. Recoules, P. Renaudin, J. Robiche, F. Dorchies, and J. Fuchs. Picosecond short-range disordering in isochorically heated aluminum at solid density. *Phys. Rev. Lett.*, 104:035002, 2010.

[76] S. Kar, K. Markey, M. Borghesi, D. C Carroll, P. McKenna, D. Neely, M. N. Quinn, and M. Zepf. Ballistic focusing of polyenergetic protons driven by petawatt laser pulses. *Phys. Rev. Lett.*, 106:225003, 2011.

[77] Teresa Bartal, Mark E Foord, Claudio Bellei, Michael H Key, Kirk A Flippo, Sandrine A Gaillard, Dustin T Offermann, Pravesh K Patel, Leonard C Jarrott, Drew P Higginson, Markus Roth, Anke Otten, Dominik Kraus, Richard B Stephens, Harry S McLean, Emilio M Giraldez, Mingsheng S Wei, Donald C Gautier, and Farhat N Beg. Focusing of short-pulse high-intensity laser-accelerated proton beams. *Nat Phys*, 8(2):139–142, 2012.

[78] Robert R. Wilson. Radiological use of fast protons. *Radiology*, 47(5):487–491, 1946.

[79] Ugo Amaldi and Gerhard Kraft. Radiotherapy with beams of carbon ions. *Reports on Progress in Physics*, 68(8):1861, 2005.

[80] W. T. Chu, B. A. Ludewigt, and T. R. Renner. Instrumentation for treatment of cancer using proton and light-ion beams. *Review of Scientific Instruments*, 64(8): 2055–2122, 1993.

[81] G Kraft. Tumortherapy with ion beams. *Nuclear Instruments and Methods in Physics Research Section A: Accelerators, Spectrometers, Detectors and Associated Equipment*, 454(1):1 – 10, 2000.

[82] HIT. URL `http://www.klinikum.uni-heidelberg.de/index.php?id=113005&L=1/`.

[83] S.V. Bulanov and V.S. Khoroshkov. Feasibility of using laser ion accelerators in proton therapy. *Plasma Physics Reports*, 28(5):453–456, 2002.

[84] Victor Malka, Sven Fritzler, Erik Lefebvre, Emmanuel d'Humières, Régis Ferrand, Georges Grillon, Claude Albaret, Samuel Meyroneinc, Jean-Paul Chambaret, Andre Antonetti, and Danièle Hulin. Practicability of protontherapy using compact laser systems. *Medical Physics*, 31(6):1587–1592, 2004.

[85] Ute Linz and Jose Alonso. What will it take for laser driven proton accelerators to be applied to tumor therapy? *Phys. Rev. ST Accel. Beams*, 10:094801, 2007.

[86] Jianhui Bin, Klaus Allinger, Walter Assmann, Günther Dollinger, Guido A. Drexler, Anna A. Friedl, Dieter Habs, Peter Hilz, Rainer Hoerlein, Nicole Humble, Stefan Karsch, Konstantin Khrennikov, Daniel Kiefer, Ferenc Krausz, Wenjun Ma, Dörte Michalski, Michael Molls, Sebastian Raith, Sabine Reinhardt, Barbara Röper, Thomas E. Schmid, Toshiki Tajima, Johannes Wenz, Olga Zlobinskaya, Joerg Schreiber, and Jan J. Wilkens. A laser-driven nanosecond proton source for radiobiological studies. *Applied Physics Letters*, 101(24):243701, 2012.

[87] J. H. Bin, W. J. Ma, K. Allinger, H. Y. Wang, D. Kiefer, S. Reinhardt, P. Hilz, K. Khrennikov, S. Karsch, X. Q. Yan, F. Krausz, T. Tajima, D. Habs, and J. Schreiber. On the small divergence of laser-driven ion beams from nanometer thick foils. *Physics of Plasmas (1994-present)*, 20(7):073113, 2013.

[88] William L Kruer. *The physics of laser plasma interactions*. New York: Addison-Wesley, 1988.

[89] J. Meyer-ter Vehn, A. Pukhov, and Zh.-M. Sheng. Relativistic laser plasma interaction. In Dimitri Batani, CharlesJ. Joachain, Sergio Martellucci, and ArthurN. Chester, editors, *Atoms, Solids, and Plasmas in Super-Intense Laser Fields*, pages 167–192. Springer US, 2001.

[90] Paul Gibbon. *Short pulse laser interactions with matter*. Imperial College Press London, 2005.

[91] John David Jackson. *Classical electrodynamics Third Edition*. Wiley, 1998.

[92] J. D. Lawson. Lasers and accelerators. *Nuclear Science, IEEE Transactions on*, 26 (3):4217–4219, 1979.

[93] P.M. Woodward. A method of calculating the field over a plane aperture required to produce a given polar diagram. *Journal of the Institution of Electrical Engineers - Part IIIA: Radiolocation*, 93:1554–1558(4), 1946.

[94] Brice Quesnel and Patrick Mora. Theory and simulation of the interaction of ultraintense laser pulses with electrons in vacuum. *Phys. Rev. E*, 58:3719–3732, 1998.

[95] A. Pukhov and J. Meyer-ter Vehn. Relativistic magnetic self-channeling of light in near-critical plasma: Three-dimensional particle-in-cell simulation. *Phys. Rev. Lett.*, 76:3975–3978, 1996.

[96] W. Lu, M. Tzoufras, C. Joshi, F. S. Tsung, W. B. Mori, J. Vieira, R. A. Fonseca, and L. O. Silva. Generating multi-gev electron bunches using single stage laser wakefield acceleration in a 3d nonlinear regime. *Phys. Rev. ST Accel. Beams*, 10: 061301, 2007.

[97] H. Y. Wang, C. Lin, Z. M. Sheng, B. Liu, S. Zhao, Z. Y. Guo, Y. R. Lu, X. T. He, J. E. Chen, and X. Q. Yan. Laser shaping of a relativistic intense, short gaussian pulse by a plasma lens. *Phys. Rev. Lett.*, 107:265002, 2011.

[98] D. F. Gordon, B. Hafizi, R. F. Hubbard, J. R. Peñano, P. Sprangle, and A. Ting. Asymmetric self-phase modulation and compression of short laser pulses in plasma channels. *Phys. Rev. Lett.*, 90:215001, 2003.

[99] J. Faure, Y. Glinec, J. J. Santos, F. Ewald, J.-P. Rousseau, S. Kiselev, A. Pukhov, T. Hosokai, and V. Malka. Observation of laser-pulse shortening in nonlinear plasma waves. *Phys. Rev. Lett.*, 95:205003, 2005.

[100] J. Schreiber, C. Bellei, S. P. D. Mangles, C. Kamperidis, S. Kneip, S. R. Nagel, C. A. J. Palmer, P. P. Rajeev, M. J. V. Streeter, and Z. Najmudin. Complete temporal characterization of asymmetric pulse compression in a laser wakefield. *Phys. Rev. Lett.*, 105:235003, 2010.

[101] Sasi Palaniyappan, B Manuel Hegelich, Hui-Chun Wu, Daniel Jung, Donald C Gautier, Lin Yin, Brian J Albright, Randall P Johnson, Tsutomu Shimada, Samuel

Letzring, Dustin T Offermann, Jun Ren, Chengkun Huang, Rainer Horlein, Brendan Dromey, Juan C Fernandez, and Rahul C Shah. Dynamics of relativistic transparency and optical shuttering in expanding overdense plasmas. *Nat Phys*, 8(10): 763–769, 2012.

[102] Scott C. Wilks and W.L. Kruer. Absorption of ultrashort, ultra-intense laser light by solids and overdense plasmas. *Quantum Electronics, IEEE Journal of*, 33(11): 1954–1968, 1997.

[103] E. J. Valeo and K. G. Estabrook. Stability of the critical surface in irradiated plasma. *Phys. Rev. Lett.*, 34:1008–1011, 1975.

[104] F. Brunel. Not-so-resonant, resonant absorption. *Phys. Rev. Lett.*, 59:52–55, 1987.

[105] W. L. Kruer and Kent Estabrook. J×b heating by very intense laser light. *Physics of Fluids (1958-1988)*, 28(1):430–432, 1985.

[106] S. C. Wilks, W. L. Kruer, M. Tabak, and A. B. Langdon. Absorption of ultra-intense laser pulses. *Phys. Rev. Lett.*, 69:1383–1386, 1992.

[107] J. Denavit. Absorption of high-intensity subpicosecond lasers on solid density targets. *Phys. Rev. Lett.*, 69:3052–3055, 1992.

[108] G. Malka and J. L. Miquel. Experimental confirmation of ponderomotive-force electrons produced by an ultrarelativistic laser pulse on a solid target. *Phys. Rev. Lett.*, 77:75–78, 1996.

[109] D. W. Forslund and C. R. Shonk. Formation and structure of electrostatic collisionless shocks. *Phys. Rev. Lett.*, 25:1699–1702, 1970.

[110] D. W. Forslund and J. P. Freidberg. Theory of laminar collisionless shocks. *Phys. Rev. Lett.*, 27:1189–1192, 1971.

[111] Luís O. Silva, Michael Marti, Jonathan R. Davies, Ricardo A. Fonseca, Chuang Ren, Frank S. Tsung, and Warren B. Mori. Proton shock acceleration in laser-plasma interactions. *Phys. Rev. Lett.*, 92:015002, 2004.

[112] S.V. Bulanov, D.V. Dylov, T.Zh. Esirkepov, F.F. Kamenets, and D.V. Sokolov. Ion acceleration in a dipole vortex in a laser plasma corona. *Plasma Physics Reports*, 31(5):369–381, 2005.

[113] S. V. Bulanov and T. Zh. Esirkepov. Comment on "collimated multi-mev ion beams from high-intensity laser interactions with underdense plasma". *Phys. Rev. Lett.*, 98:049503, 2007.

[114] L. YIN, B. J. ALBRIGHT, B. M. HEGELICH, and J. C. FERNÁNDEZ. Gev laser ion acceleration from ultrathin targets: The laser break-out afterburner. *Laser and Particle Beams*, 24:291–298, 2006.

[115] L. Yin, B. J. Albright, B. M. Hegelich, K. J. Bowers, K. A. Flippo, T. J. T. Kwan, and J. C. Fernández. Monoenergetic and gev ion acceleration from the laser break-out afterburner using ultrathin targetsa). *Physics of Plasmas (1994-present)*, 14(5): 056706, 2007.

[116] B. J. Albright, L. Yin, Kevin J. Bowers, B. M. Hegelich, K. A. Flippo, T. J. T. Kwan, and J. C. Fernández. Relativistic buneman instability in the laser breakout afterburner. *Physics of Plasmas (1994-present)*, 14(9):094502, 2007.

[117] L. Yin, B. J. Albright, K. J. Bowers, D. Jung, J. C. Fernández, and B. M. Hegelich. Three-dimensional dynamics of breakout afterburner ion acceleration using high-contrast short-pulse laser and nanoscale targets. *Phys. Rev. Lett.*, 107:045003, 2011.

[118] Stephen P. Hatchett, Curtis G. Brown, Thomas E. Cowan, Eugene A. Henry, Joy S. Johnson, Michael H. Key, Jeffrey A. Koch, A. Bruce Langdon, Barbara F. Lasinski, Richard W. Lee, Andrew J. Mackinnon, Deanna M. Pennington, Michael D. Perry, Thomas W. Phillips, Markus Roth, T. Craig Sangster, Mike S. Singh, Richard A. Snavely, Mark A. Stoyer, Scott C. Wilks, and Kazuhito Yasuike. Electron, photon, and ion beams from the relativistic interaction of petawatt laser pulses with solid targets. *Physics of Plasmas (1994-present)*, 7(5):2076–2082, 2000.

[119] S. C. Wilks, A. B. Langdon, T. E. Cowan, M. Roth, M. Singh, S. Hatchett, M. H. Key, D. Pennington, A. MacKinnon, and R. A. Snavely. Energetic proton generation in ultra-intense laser-solid interactions. *Physics of Plasmas (1994-present)*, 8 (2):542–549, 2001.

[120] URL https://www.llnl.gov/str//MPerry.html/.

[121] J. S. Pearlman and R. L. Morse. Maximum expansion velocities of laser-produced plasmas. *Phys. Rev. Lett.*, 40:1652–1655, 1978.

[122] J. Denavit. Collisionless plasma expansion into a vacuum. *Physics of Fluids (1958-1988)*, 22(7):1384–1392, 1979.

[123] Patrick Mora and R. Pellat. Self-similar expansion of a plasma into a vacuum. *Physics of Fluids (1958-1988)*, 22(12):2300–2304, 1979.

[124] M. A. True, James R. Albritton, and E. A. Williams. Fast ion production by suprathermal electrons in laser fusion plasmas. *Physics of Fluids (1958-1988)*, 24(10):1885–1893, 1981.

[125] Yasuaki Kishimoto, Kunioki Mima, Tsuguhiro Watanabe, and Kyoji Nishikawa. Analysis of fast-ion velocity distributions in laser plasmas with a truncated maxwellian velocity distribution of hot electrons. *Physics of Fluids (1958-1988)*, 26(8):2308–2315, 1983.

[126] P. Mora. Plasma expansion into a vacuum. *Phys. Rev. Lett.*, 90:185002, 2003.

[127] M. Passoni, V. T. Tikhonchuk, M. Lontano, and V. Yu. Bychenkov. Charge separation effects in solid targets and ion acceleration with a two-temperature electron distribution. *Phys. Rev. E*, 69:026411, 2004.

[128] V T Tikhonchuk, A A Andreev, S G Bochkarev, and V Yu Bychenkov. Ion acceleration in short-laser-pulse interaction with solid foils. *Plasma Physics and Controlled Fusion*, 47(12B):B869, 2005.

[129] P. Mora. Thin-foil expansion into a vacuum. *Phys. Rev. E*, 72:056401, 2005.

[130] J. Schreiber, F. Bell, F. Grüner, U. Schramm, M. Geissler, M. Schnürer, S. Ter-Avetisyan, B. M. Hegelich, J. Cobble, E. Brambrink, J. Fuchs, P. Audebert, and D. Habs. Analytical model for ion acceleration by high-intensity laser pulses. *Phys. Rev. Lett.*, 97:045005, 2006.

[131] T. Esirkepov, M. Borghesi, S. V. Bulanov, G. Mourou, and T. Tajima. Highly efficient relativistic-ion generation in the laser-piston regime. *Phys. Rev. Lett.*, 92:175003, 2004.

[132] Y. Sentoku, T. E. Cowan, A. Kemp, and H. Ruhl. High energy proton acceleration in interaction of short laser pulse with dense plasma target. *Physics of Plasmas (1994-present)*, 10(5):2009–2015, 2003.

[133] Andrea Macchi, Federica Cattani, Tatiana V. Liseykina, and Fulvio Cornolti. Laser acceleration of ion bunches at the front surface of overdense plasmas. *Phys. Rev. Lett.*, 94:165003, 2005.

[134] O. Klimo, J. Psikal, J. Limpouch, and V. T. Tikhonchuk. Monoenergetic ion beams from ultrathin foils irradiated by ultrahigh-contrast circularly polarized laser pulses. *Phys. Rev. ST Accel. Beams*, 11:031301, 2008.

[135] X. Q. Yan, C. Lin, Z. M. Sheng, Z. Y. Guo, B. C. Liu, Y. R. Lu, J. X. Fang, and J. E. Chen. Generating high-current monoenergetic proton beams by a circularly-polarized laser pulse in the phase-stableacceleration regime. *Phys. Rev. Lett.*, 100: 135003, 2008.

[136] A P L Robinson, M Zepf, S Kar, R G Evans, and C Bellei. Radiation pressure acceleration of thin foils with circularly polarized laser pulses. *New Journal of Physics*, 10(1):013021, 2008.

[137] A P L Robinson, P Gibbon, M Zepf, S Kar, R G Evans, and C Bellei. Relativistically correct hole-boring and ion acceleration by circularly polarized laser pulses. *Plasma Physics and Controlled Fusion*, 51(2):024004, 2009.

[138] X. Q. Yan, H. C. Wu, Z. M. Sheng, J. E. Chen, and J. Meyer-ter Vehn. Self-organizing gev, nanocoulomb, collimated proton beam from laser foil interaction at 7×10^{21} $\mathbf{W}$/cm^2. *Phys. Rev. Lett.*, 103:135001, 2009.

[139] B. Qiao, M. Zepf, M. Borghesi, and M. Geissler. Stable gev ion-beam acceleration from thin foils by circularly polarized laser pulses. *Phys. Rev. Lett.*, 102:145002, 2009.

[140] Andrea Macchi, Silvia Veghini, and Francesco Pegoraro. "light sail" acceleration reexamined. *Phys. Rev. Lett.*, 103:085003, 2009.

[141] Liangliang Ji, Baifei Shen, Xiaomei Zhang, Fengchao Wang, Zhangyin Jin, Xuemei Li, Meng Wen, and John R. Cary. Generating monoenergetic heavy-ion bunches with laser-induced electrostatic shocks. *Phys. Rev. Lett.*, 101:164802, 2008.

[142] Xiaomei Zhang, Baifei Shen, Liangliang Ji, Fengchao Wang, Zhangying Jin, Xuemei Li, Meng Wen, and John R. Cary. Ion acceleration with mixed solid targets interacting with circularly polarized lasers. *Phys. Rev. ST Accel. Beams*, 12:021301, 2009.

[143] M. Chen, A. Pukhov, T. P. Yu, and Z. M. Sheng. Enhanced collimated gev monoenergetic ion acceleration from a shaped foil target irradiated by a circularly polarized laser pulse. *Phys. Rev. Lett.*, 103:024801, 2009.

[144] B. Qiao, M. Zepf, M. Borghesi, B. Dromey, M. Geissler, A. Karmakar, and P. Gibbon. Radiation-pressure acceleration of ion beams from nanofoil targets: The leaky light-sail regime. *Phys. Rev. Lett.*, 105:155002, 2010.

[145] Tong-Pu Yu, Alexander Pukhov, Gennady Shvets, and Min Chen. Stable laser-driven proton beam acceleration from a two-ion-species ultrathin foil. *Phys. Rev. Lett.*, 105:065002, 2010.

[146] G MARX. Interstellar Vehicle Propelled By Terrestrial Laser Beam. *Nature*, 211 (5044):22–23, 1966.

[147] D. Kiefer, A. Henig, D. Jung, D. C. Gautier, K. A. Flippo, S. A. Gaillard, S. Letzring, R. P. Johnson, R. C. Shah, T. Shimada, J. C. Fernández, V. Kh. Liechtenstein, J. Schreiber, B. M. Hegelich, and D. Habs. First observation of quasi-monoenergetic electron bunches driven out of ultra-thin diamond-like carbon (dlc) foils. *The European Physical Journal D*, 55(2):427–432, 2009.

[148] H Baumhacker, A Böswald, H Haas, M Fischer, W Fölsner, G Keller, U Andiel, X Dong, M Dreher, K Eidmann, et al. Advanced titanium sapphire laser atlas mpq-report 272. Technical report, Technical Report, Max-Planck-Institut für Quantenoptik, 2001.

[149] T. Fuji, A. Unterhuber, V.S. Yakovlev, G. Tempea, A. Stingl, F. Krausz, and W. Drexler. Generation of smooth, ultra-broadband spectra directly from a prismless ti:sapphire laser. *Applied Physics B*, 77(1):125–128, 2003.

[150] Jens Osterhoff. *Stable, ultra-relativistic electron beams by laser-wakefield acceleration*. PhD thesis, LMU, 2009.

[151] O.E. Martinez. Design of high-power ultrashort pulse amplifiers by expansion and recompression. *Quantum Electronics, IEEE Journal of*, 23(8):1385–1387, 1987.

[152] F. Verluise, V. Laude, Z. Cheng, Ch. Spielmann, and P. Tournois. Amplitude and phase control of ultrashort pulses by use of an acousto-optic programmable dispersive filter: pulse compression and shaping. *Opt. Lett.*, 25(8):575–577, 2000.

[153] J. E. Murray and W. H. Lowdermilk. Nd:yag regenerative amplifier. *Journal of Applied Physics*, 51(7):3548–3556, 1980.

[154] T. Oksenhendler, D. Kaplan, P. Tournois, G.M. Greetham, and F. Estable. Intracavity acousto-optic programmable gain control for ultra-wide-band regenerative amplifiers. *Applied Physics B*, 83(4):491–494, 2006.

[155] H. Baumhacker, G. Pretzler, K. J. Witte, M. Hegelich, M. Kaluza, S. Karsch, A. Kudryashov, V. Samarkin, and A. Roukossouev. Correction of strong phase and amplitude modulations by two deformable mirrors in a multistaged ti:sapphire laser. *Opt. Lett.*, 27(17):1570–1572, 2002.

[156] Patrick O'Shea, Mark Kimmel, Xun Gu, and Rick Trebino. Highly simplified device for ultrashort-pulse measurement. *Opt. Lett.*, 26(12):932–934, 2001.

[157] Daniel J. Kane and Rick Trebino. Single-shot measurement of the intensity and phase of an arbitrary ultrashort pulse by using frequency-resolved optical gating. *Opt. Lett.*, 18(10):823–825, 1993.

[158] G. Doumy, F. Quéré, O. Gobert, M. Perdrix, Ph. Martin, P. Audebert, J. C. Gauthier, J.-P. Geindre, and T. Wittmann. Complete characterization of a plasma mirror for the production of high-contrast ultraintense laser pulses. *Phys. Rev. E*, 69:026402, 2004.

[159] C Thaury, F Quere, J.-P. Geindre, A Levy, T Ceccotti, P Monot, M Bougeard, F Reau, P d'Oliveira, P Audebert, R Marjoribanks, and Ph. Martin. Plasma mirrors for ultrahigh-intensity optics. *Nat Phys*, 3(6):424–429, 2007.

[160] Daniel Kiefer. *Relativistic electron mirrors from high intensity laser nanofoil interactions*. PhD thesis, LMU, 2012.

[161] Hakan Urey. Spot size, depth-of-focus, and diffraction ring intensity formulas for truncated gaussian beams. *Appl. Opt.*, 43(3):620–625, 2004.

[162] Chris Hooker, Yunxin Tang, Oleg Chekhlov, John Collier, Edwin Divall, Klaus Ertel, Steve Hawkes, Bryn Parry, and P. P. Rajeev. Improving coherent contrast of petawatt laser pulses. *Opt. Express*, 19(3):2193–2203, 2011.

[163] C.J. Hooker, S. Blake, O. Chekhlov, R.J. Clarke, J.L. Collier, E.J. Divall, K. Ertel, P. S. Foster, S.J. Hawkes, P. Holligan, B. Landowski, W. J. Lester, D. Neely, B. Parry, R. Pattathil, M. Streeter, and B. E. Wyborn. Commissioning the astra gemini petawatt ti:sapphire laser system. In *Lasers and Electro-Optics, 2008 and 2008 Conference on Quantum Electronics and Laser Science. CLEO/QELS 2008. Conference on*, pages 1–2, 2008.

[164] MJV Streeter, PS Foster, FH Cameron, R Bickerton, S Blake, P Brummit, B Costello, E Divall, C Hooker, P Holligan, et al. Astra gemini compact plasma mirror system. *Central Laser Facility Annual Report*, 2009.

[165] J.H. Bin, W.J. Ma, C. Kreuzer, D. Kiefer, J. Meyer-ter Vehn, J. Schreiber, M.J.V. Streeter, Z. Najmudin, M. Yeung, S. Cousens, B. Dromey, M. Zepf, P.S. Foster, C. Spindloe, and R. Pattathil. The intensity of contrast enhanced astra gemini laser. *Central Laser Facility Annual Report*, 2012.

[166] Ian G. Brown. Cathodic arc deposition of films. *Annual Review of Materials Science*, 28(1):243–269, 1998.

[167] A Anders, S Anders, and I G Brown. Transport of vacuum arc plasmas through magnetic macroparticle filters. *Plasma Sources Science and Technology*, 4(1):1, 1995.

[168] Wenjun Ma, V.Kh. Liechtenstein, J. Szerypo, D. Jung, P. Hilz, B.M. Hegelich, H.J. Maier, J. Schreiber, and D. Habs. Preparation of self-supporting diamond-like carbon nanofoils with thickness less than 5 nm for laser-driven ion acceleration. *Nuclear Instruments and Methods in Physics Research Section A: Accelerators, Spectrometers, Detectors and Associated Equipment*, 655(1):53 – 56, 2011.

[169] Andreas Henig. *Advanced approaches to high intensity laser-driven ion acceleration*. PhD thesis, LMU, 2010.

[170] Daniel Jung. *Ion acceleration from relativistic laser nano-target interaction*. PhD thesis, LMU, 2012.

[171] R Hoerlein, S Steinke, A Henig, SG Rykovanov, M Schnürer, T Sokollik, D Kiefer, D Jung, XQ Yan, T Tajima, et al. Dynamics of nanometer-scale foil targets irradiated with relativistically intense laser pulses. *Laser and Particle Beams*, 29: 383–388, 2011.

[172] Wenjun Ma, Li Song, Rong Yang, Taihua Zhang, Yuanchun Zhao, Lianfeng Sun, Yan Ren, Dongfang Liu, Lifeng Liu, Jun Shen, Zhengxing Zhang, Yanjuan Xiang, Weiya Zhou, and SiShen Xie. Directly synthesized strong, highly conducting, transparent single-walled carbon nanotube films. *Nano Letters*, 7(8):2307–2311, 2007.

[173] R. Ramis, K. Eidmann, J. Meyer ter Vehn, and S. Hüller. Multi-fs - a computer code for laser-plasma interaction in the femtosecond regime. *Computer Physics Communications*, 183(3):637 – 655, 2012.

[174] G. Rusch, E. Winkel, A. Noll, and W. Heinrich. The siegen automatic measuring system for track detectors: New developments. *International Journal of Radiation Applications and Instrumentation. Part D. Nuclear Tracks and Radiation Measurements*, 19(1):261 – 266, 1991.

[175] Azam Niroomand-Rad, Charles Robert Blackwell, Bert M. Coursey, Kenneth P. Gall, James M. Galvin, William L. McLaughlin, Ali S. Meigooni, Ravinder Nath, James E. Rodgers, and Christopher G. Soares. Radiochromic film dosimetry: Recommendations of aapm radiation therapy committee task group 55. *Medical Physics*, 25(11):2093–2115, 1998.

[176] Li Zhao and Indra J Das. Gafchromic ebt film dosimetry in proton beams. *Physics in Medicine and Biology*, 55(10):N291, 2010.

[177] Daniel Kirby, Stuart Green, Hugo Palmans, Richard Hugtenburg, Cecile Wojnecki, and David Parker. Let dependence of gafchromic films and an ion chamber in low-energy proton dosimetry. *Physics in Medicine and Biology*, 55(2):417, 2010.

[178] Stopping Powers ICRU. Ranges for protons and alpha particles. *International Commission on Radiation Units and Measurements. Report*, 49, 1993.

[179] URL `https://www.srim.org/`.

[180] Sabine Reinhardt. *Detection of laser-accelerated protons*. PhD thesis, LMU, 2012.

[181] Kenji Takahashi, Katsuhiro Kohda, Junji Miyahara, Yoshihiko Kanemitsu, Koji Amitani, and Shigeo Shionoya. Mechanism of photostimulated luminescence in BaFX:Eu^{2+} (X=Cl,Br) phosphors. *Journal of Luminescence*, 31-32, Part 1(0):266 – 268, 1984.

[182] Junji Miyahara, Kenji Takahashi, Yoshiyuki Amemiya, Nobuo Kamiya, and Yoshinori Satow. A new type of x-ray area detector utilizing laser stimulated luminescence. *Nuclear Instruments and Methods in Physics Research Section A: Accelerators, Spectrometers, Detectors and Associated Equipment*, 246(1-3):572 – 578, 1986.

[183] Yasuo Iwabuchi, Nobufumi Mori, Kenji Takahashi, Terumi Matsuda, and Shigeo Shionoya. Mechanism of photostimulated luminescence process in BaFBr:Eu^{2+} phosphors. *Japanese Journal of Applied Physics*, 33(1R):178, 1994.

[184] A. Buck, K. Zeil, A. Popp, K. Schmid, A. Jochmann, S. D. Kraft, B. Hidding, T. Kudyakov, C. M. S. Sears, L. Veisz, S. Karsch, J. Pawelke, R. Sauerbrey, T. Cowan, F. Krausz, and U. Schramm. Absolute charge calibration of scintillating screens for relativistic electron detection. *Review of Scientific Instruments*, 81(3):033301, 2010.

[185] Joseph John Thomson. Bakerian lecture: Rays of positive electricity. *Proceedings of the Royal Society of London. Series A*, 89(607):1–20, 1913.

[186] Joerg Schreiber. *Ion acceleration driven by high-intensity laser pulses*. PhD thesis, LMU, 2006.

[187] Hui Chen, A. U. Hazi, R. van Maren, S. N. Chen, J. Fuchs, M. Gauthier, S. Le Pape, J. R. Rygg, and R. Shepherd. An imaging proton spectrometer for short-pulse laser plasma experimentsa). *Review of Scientific Instruments*, 81(10):–, 2010.

[188] D. Jung, R. Hörlein, D. C. Gautier, S. Letzring, D. Kiefer, K. Allinger, B. J. Albright, R. Shah, S. Palaniyappan, L. Yin, J. C. Fernández, D. Habs, and B. M. Hegelich. A novel high resolution ion wide angle spectrometer. *Review of Scientific Instruments*, 82(4):–, 2011.

[189] C.-M. Ma, I. Veltchev, E. Fourkal, J.S. Li, W. Luo, J. Fan, T. Lin, and A. Pollack. Development of a laser-driven proton accelerator for cancer therapy. *Laser Physics*, 16(4):639–646, 2006.

[190] Toshiki Tajima, Dietrich Habs, and Xueqing Yan. Laser acceleration of ions for radiation therapy. *Reviews of Accelerator Science and Technology*, 02(01):201–228, 2009.

[191] S. Fritzler, V. Malka, G. Grillon, J. P. Rousseau, F. Burgy, E. Lefebvre, E. d'Humières, P. McKenna, and K. W. D. Ledingham. Proton beams generated with high-intensity lasers: Applications to medical isotope production. *Applied Physics Letters*, 83(15):3039–3041, 2003.

[192] S D Kraft, C Richter, K Zeil, M Baumann, E Beyreuther, S Bock, M Bussmann, T E Cowan, Y Dammene, W Enghardt, U Helbig, L Karsch, T Kluge, L Laschinsky, E Lessmann, J Metzkes, D Naumburger, R Sauerbrey, M. Schürer, M Sobiella, J Woithe, U Schramm, and J Pawelke. Dose-dependent biological damage of tumour cells by laser-accelerated proton beams. *New Journal of Physics*, 12(8): 085003, 2010.

[193] Koichi Ogura, Mamiko Nishiuchi, Alexander S. Pirozhkov, Tsuyoshi Tanimoto, Akito Sagisaka, Timur Zh. Esirkepov, Masaki Kando, Toshiyuki Shizuma, Takehito Hayakawa, Hiromitsu Kiriyama, Takuya Shimomura, Shyuji Kondo, Shuhei Kanazawa, Yoshiki Nakai, Hajime Sasao, Fumitaka Sasao, Yuji Fukuda, Hironao Sakaki, Masato Kanasaki, Akifumi Yogo, Sergei V. Bulanov, Paul R. Bolton, and Kiminori Kondo. Proton acceleration to 40 mev using a high intensity, high contrast optical parametric chirped-pulse amplification/ti:sapphire hybrid laser system. *Opt. Lett.*, 37(14):2868–2870, 2012.

[194] Michael Baumann, Sã¸ren M Bentzen, Wolfgang Doerr, Michael C Joiner, Michele Saunders, Ian F Tannock, and Howard D Thames. The translational research chain: is it delivering the goods? *International Journal of Radiation Oncology Biology Physics*, 49(2):345 – 351, 2001.

[195] A. Yogo, K. Sato, M. Nishikino, M. Mori, T. Teshima, H. Numasaki, M. Murakami, Y. Demizu, S. Akagi, S. Nagayama, K. Ogura, A. Sagisaka, S. Orimo, M. Nishiuchi, A. S. Pirozhkov, M. Ikegami, M. Tampo, H. Sakaki, M. Suzuki, I. Daito, Y. Oishi, H. Sugiyama, H. Kiriyama, H. Okada, S. Kanazawa, S. Kondo, T. Shimomura, Y. Nakai, M. Tanoue, H. Sasao, D. Wakai, P. R. Bolton, and H. Daido. Application of laser-accelerated protons to the demonstration of dna double-strand breaks in human cancer cells. *Applied Physics Letters*, 94(18):181502, 2009.

[196] A. Yogo, T. Maeda, T. Hori, H. Sakaki, K. Ogura, M. Nishiuchi, A. Sagisaka, H. Kiriyama, H. Okada, S. Kanazawa, T. Shimomura, Y. Nakai, M. Tanoue, F. Sasao, P. R. Bolton, M. Murakami, T. Nomura, S. Kawanishi, and K. Kondo. Measurement of relative biological effectiveness of protons in human cancer cells using a laser-driven quasimonoenergetic proton beamline. *Applied Physics Letters*, 98(5):053701, 2011.

[197] D. Doria, K. F. Kakolee, S. Kar, S. K. Litt, F. Fiorini, H. Ahmed, S. Green, J. C. G. Jeynes, J. Kavanagh, D. Kirby, K. J. Kirkby, C. L. Lewis, M. J. Merchant, G. Nersisyan, R. Prasad, K. M. Prise, G. Schettino, M. Zepf, and M. Borghesi. Biological effectiveness on live cells of laser driven protons at dose rates exceeding 109 gy/s. *AIP Advances*, 2(1):011209, 2012.

[198] Victor Malka, Jérôme Faure, and Yann A. Gauduel. Ultra-short electron beams based spatio-temporal radiation biology and radiotherapy. *Mutation Research/Reviews in Mutation Research*, 704(1-3):142 – 151, 2010.

[199] M. Schollmeier, S. Becker, M. Geißel, K. A. Flippo, A. Blažević, S. A. Gaillard, D. C. Gautier, F. Grüner, K. Harres, M. Kimmel, F. Nürnberg, P. Rambo, U. Schramm, J. Schreiber, J. Schütrumpf, J. Schwarz, N. A. Tahir, B. Atherton, D. Habs, B. M. Hegelich, and M. Roth. Controlled transport and focusing of laser-accelerated protons with miniature magnetic devices. *Phys. Rev. Lett.*, 101:055004, 2008.

[200] Nicole Humble. *Investigative methods adapted to assess the biological properties of laser-driven protons*. PhD thesis, TUM, 2014.

[201] O. Zlobinskaya, G. Dollinger, D. Michalski, V. Hable, C. Greubel, G. Du, G. Multhoff, B. Röper, M. Molls, and T.E. Schmid. Induction and repair of dna double-strand breaks assessed by gamma-h2ax foci after irradiation with pulsed or continuous proton beams. *Radiation and Environmental Biophysics*, 51(1):23–32, 2012.

[202] Nicolaas Franken, Rosemarie ten Cate, Przemek Krawczyk, Jan Stap, Jaap Haveman, Jacob Aten, and Gerrit Barendsen. Comparison of rbe values of high- let alpha-particles for the induction of dna-dsbs, chromosome aberrations and cell reproductive death. *Radiation Oncology*, 6(1):64, 2011.

[203] M. BELLI F. CERA R. CHERUBINI M. DALLA VECCHIA A. M. I. HAQUE F. IANZINI G. MOSCHINI O. SAPORA G. SIMONE M. A. TABOCCHINI P. TIVERON. Rbe-let relationships for cell inactivation and mutation induced by low energy protons in v79 cells: further results at the lnl facility. *International Journal of Radiation Biology*, 74(4):501–509, 1998.

[204] T E Schmid, G Dollinger, A Hauptner, V Hable, C Greubel, S Auer, A A Friedl, M Molls, and B Röper. No Evidence for a Different RBE between Pulsed and Continuous 20 MeV Protons. *Radiation Research*, 172(5):567–574, 2009.

[205] Susanne Auer, Volker Hable, Christoph Greubel, Guido Drexler, Thomas Schmid, Claus Belka, Gunther Dollinger, and Anna Friedl. Survival of tumor cells after proton irradiation with ultra-high dose rates. *Radiation Oncology*, 6(1):139, 2011.

[206] T. Burris-Mog, K. Harres, F. Nürnberg, S. Busold, M. Bussmann, O. Deppert, G. Hoffmeister, M. Joost, M. Sobiella, A. Tauschwitz, B. Zielbauer, V. Bagnoud, T. Herrmannsdoerfer, M. Roth, and T. E. Cowan. Laser accelerated protons captured and transported by a pulse power solenoid. *Phys. Rev. ST Accel. Beams*, 14: 121301, 2011.

[207] S. Kar, K. Markey, P. T. Simpson, C. Bellei, J. S. Green, S. R. Nagel, S. Kneip, D. C. Carroll, B. Dromey, L. Willingale, E. L. Clark, P. McKenna, Z. Najmudin, K. Krushelnick, P. Norreys, R. J. Clarke, D. Neely, M. Borghesi, and M. Zepf. Dynamic control of laser-produced proton beams. *Phys. Rev. Lett.*, 100:105004, 2008.

[208] T. Sokollik, M. Schnürer, S. Steinke, P. V. Nickles, W. Sandner, M. Amin, T. Toncian, O. Willi, and A. A. Andreev. Directional laser-driven ion acceleration from microspheres. *Phys. Rev. Lett.*, 103:135003, 2009.

[209] J. Fuchs, T. E. Cowan, P. Audebert, H. Ruhl, L. Gremillet, A. Kemp, M. Allen, A. Blazevic, J.-C. Gauthier, M. Geissel, M. Hegelich, S. Karsch, P. Parks, M. Roth, Y. Sentoku, R. Stephens, and E. M. Campbell. Spatial uniformity of laser-accelerated ultrahigh-current mev electron propagation in metals and insulators. *Phys. Rev. Lett.*, 91:255002, 2003.

[210] K Zeil, J Metzkes, T Kluge, M Bussmann, T E Cowan, S D Kraft, R Sauerbrey, and U Schramm. Direct observation of prompt pre-thermal laser ion sheath acceleration. *Nat Commun*, 3:874, 2012.

[211] A. A. Andreev, S. Steinke, M. Schnuerer, A. Henig, P. V. Nickles, K. Y. Platonov, T. Sokollik, and W. Sandner. Hybrid ion acceleration with ultrathin composite foils irradiated by high intensity circularly-polarized laser light. *Physics of Plasmas (1994-present)*, 17(12):123111, 2010.

[212] A. J. Mackinnon, M. Borghesi, S. Hatchett, M. H. Key, P. K. Patel, H. Campbell, A. Schiavi, R. Snavely, S. C. Wilks, and O. Willi. Effect of plasma scale length on multi-mev proton production by intense laser pulses. *Phys. Rev. Lett.*, 86:1769–1772, 2001.

[213] J. Fuchs, C. A. Cecchetti, M. Borghesi, T. Grismayer, E. d'Humières, P. Antici, S. Atzeni, P. Mora, A. Pipahl, L. Romagnani, A. Schiavi, Y. Sentoku, T. Toncian, P. Audebert, and O. Willi. Laser-foil acceleration of high-energy protons in small-scale plasma gradients. *Phys. Rev. Lett.*, 99:015002, 2007.

[214] O Jöckel, J Polz, S M Pfotenhauer, H-P Schlenvoigt, H Schwoerer, and M C Kaluza. All-optical measurement of the hot electron sheath driving laser ion acceleration from thin foils. *New Journal of Physics*, 12(10):103027, 2010.

[215] J. J. Santos, F. Amiranoff, S. D. Baton, L. Gremillet, M. Koenig, E. Martinolli, M. Rabec Le Gloahec, C. Rousseaux, D. Batani, A. Bernardinello, G. Greison, and

T. Hall. Fast electron transport in ultraintense laser pulse interaction with solid targets by rear-side self-radiation diagnostics. *Phys. Rev. Lett.*, 89:025001, 2002.

[216] F. Dollar, C. Zulick, A. G. R. Thomas, V. Chvykov, J. Davis, G. Kalinchenko, T. Matsuoka, C. McGuffey, G. M. Petrov, L. Willingale, V. Yanovsky, A. Maksimchuk, and K. Krushelnick. Finite spot effects on radiation pressure acceleration from intense high-contrast laser interactions with thin targets. *Phys. Rev. Lett.*, 108: 175005, 2012.

[217] C G R Geddes, Cs. Toth, J van Tilborg, E Esarey, C B Schroeder, D Bruhwiler, C Nieter, J Cary, and W P Leemans. High-quality electron beams from a laser wakefield accelerator using plasma-channel guiding. *Nature*, 431(7008):538–541, 2004.

[218] J Faure, Y Glinec, A Pukhov, S Kiselev, S Gordienko, E Lefebvre, J.-P. Rousseau, F Burgy, and V Malka. A laser-plasma accelerator producing monoenergetic electron beams. *Nature*, 431(7008):541–544, 2004.

[219] S P D Mangles, C D Murphy, Z Najmudin, A G R Thomas, J L Collier, A E Dangor, E J Divall, P S Foster, J G Gallacher, C J Hooker, D A Jaroszynski, A J Langley, W B Mori, P A Norreys, F S Tsung, R Viskup, B R Walton, and K Krushelnick. Monoenergetic beams of relativistic electrons from intense laser-plasma interactions. *Nature*, 431(7008):535–538, 2004.

[220] W P Leemans, B Nagler, A J Gonsalves, Cs. Toth, K Nakamura, C G R Geddes, E Esarey, C B Schroeder, and S M Hooker. GeV electron beams from a centimetre-scale accelerator. *Nat Phys*, 2(10):696–699, 2006.

[221] Xiaoming Wang, Rafal Zgadzaj, Neil Fazel, Zhengyan Li, S A Yi, Xi Zhang, Watson Henderson, Y.-Y. Chang, R Korzekwa, H.-E. Tsai, C.-H. Pai, H Quevedo, G Dyer, E Gaul, M Martinez, A C Bernstein, T Borger, M Spinks, M Donovan, V Khudik, G Shvets, T Ditmire, and M C Downer. Quasi-monoenergetic laser-plasma acceleration of electrons to 2 GeV. *Nat Commun*, 4, 2013.

[222] Matthew Streeter. *Ultrafast dynamics of relativistic laser plasma interactions*. PhD thesis, Imperial College London, 2013.

[223] L. Willingale, S. R. Nagel, A. G. R. Thomas, C. Bellei, R. J. Clarke, A. E. Dangor, R. Heathcote, M. C. Kaluza, C. Kamperidis, S. Kneip, K. Krushelnick, N. Lopes, S. P. D. Mangles, W. Nazarov, P. M. Nilson, and Z. Najmudin. Characterization

of high-intensity laser propagation in the relativistic transparent regime through measurements of energetic proton beams. *Phys. Rev. Lett.*, 102:125002, 2009.

[224] K Zeil, S D Kraft, S Bock, M Bussmann, T E Cowan, T Kluge, J Metzkes, T Richter, R Sauerbrey, and U Schramm. The scaling of proton energies in ultrashort pulse laser plasma acceleration. *New Journal of Physics*, 12(4):045015, 2010.

[225] H. Y. Wang, X. Q. Yan, J. E. Chen, X. T. He, W. J. Ma, J. H. Bin, J. Schreiber, T. Tajima, and D. Habs. Efficient and stable proton acceleration by irradiating a two-layer target with a linearly polarized laser pulse. *Physics of Plasmas (1994-present)*, 20(1):013101, 2013.

[226] D. B. Zou, H. B. Zhuo, X. H. Yang, F. Q. Shao, Y. Y. Ma, T. P. Yu, H. C. Wu, Y. Yin, Z. Y. Ge, and X. H. Li. Enhanced target normal sheath acceleration based on the laser relativistic self-focusing. *Physics of Plasmas (1994-present)*, 21(6): 063103, 2014.

[227] A. Pukhov, Z.-M. Sheng, and J. Meyer-ter Vehn. Particle acceleration in relativistic laser channels. *Physics of Plasmas (1994-present)*, 6(7):2847–2854, 1999.

[228] C. Gahn, G. D. Tsakiris, A. Pukhov, J. Meyer-ter Vehn, G. Pretzler, P. Thirolf, D. Habs, and K. J. Witte. Multi-mev electron beam generation by direct laser acceleration in high-density plasma channels. *Phys. Rev. Lett.*, 83:4772–4775, 1999.

[229] J. Schreiber, F. Bell, and Z. Najmudin. Optimization of relativistic laser-ion acceleration. *High Power Laser Science and Engineering*, 2, 2014.

[230] Aurélie Jullien, Olivier Albert, Frédéric Burgy, Guy Hamoniaux, Jean-Philippe Rousseau, Jean-Paul Chambaret, Frédérika Augé-Rochereau, Gilles Chériaux, Jean Etchepare, Nikolay Minkovski, and Solomon M. Saltiel. 10^{-10} temporal contrast for femtosecond ultraintense lasers by cross-polarized wave generation. *Opt. Lett.*, 30(8):920–922, 2005.

[231] Rahul C. Shah, Randall P. Johnson, Tsutomu Shimada, Kirk A. Flippo, Juan C. Fernandez, and B. M. Hegelich. High-temporal contrast using low-gain optical parametric amplification. *Opt. Lett.*, 34(15):2273–2275, 2009.

[232] LEX. URL `http://www.lex.physik.uni-muenchen.de/`.

[233] CALA. URL `http://www.lex.physik.uni-muenchen.de/cala/index.html/`.

Publications

Peer reviewed publications

2015

- **J. H. Bin**, W. J. Ma, H. Y. Wang, M. J. V. Streeter, C. Kreuzer, D. Kiefer, M. Yeung, S. Cousens, P. S. Foster, B. Dromey, X. Q. Yan, R. Ramis, J. Meyer-ter-Vehn, M. Zepf, and J. Schreiber, Ion acceleration using relativistic pulse shaping in near-critical-density plasmas. *Phys. Rev. Lett.*, 115:064801 (2015).

2014

- W. J. Ma, **J. H. Bin**, H. Y. Wang, M. Yeung, C. Kreuzer, M. Streeter, P. S. Foster, S. Cousens, D. Kiefer, B. Dromey, X. Q. Yan, J. Meyer-ter-Vehn, M. Zepf, and J. Schreiber, Bright subcycle extreme ultraviolet bursts from a single dense relativistic electron sheet. *Phys. Rev. Lett.*, 113:235002 (2014).

- M. Yeung, B. Dromey, S. Cousens, T. Dzelzainis, D. Kiefer, J. Schreiber, **J. H. Bin**, W. Ma, C. Kreuzer, J. Meyer-ter-Vehn, M. J. V. Streeter, P. S. Foster, S. Rykovanov, and M. Zepf, Dependence of laser-driven coherent synchrotron emission efficiency on pulse ellipticity and implications for polarization gating. *Phys. Rev. Lett.*, 112:123902 (2014).

- H. Y. Wang, C. Lin, B. Liu, Z. M. Sheng, H. Y. Lu, W. J. Ma, **J. H. Bin**, J. Schreiber, X. T. He, J. E. Chen, M. Zepf, and X. Q. Yan, Laser-driven three-stage heavy-ion acceleration from relativistic laser-plasma interaction. *Phys. Rev. E*, 89:013107 (2014).

2013

- **J. H. Bin**, W. J. Ma, K. Allinger, H. Y. Wang, D. Kiefer, S. Reinhardt, P. Hilz, K. Khrennikov, S. Karsch, X. Q. Yan, F. Krausz, T. Tajima, D. Habs, and J. Schreiber,

On the small divergence of laser-driven ion beams from nanometer thick foils. *Physics of Plasmas*, 20(7):073113 (2013).

- H. Y. Wang, X. Q. Yan, J. E. Chen, X. T. He, W. J. Ma, **J. H. Bin**, J. Schreiber, T. Tajima, and D. Habs, Efficient and stable proton acceleration by irradiating a two-layer target with a linearly polarized laser pulse. *Physics of Plasmas*, 20(1):013101 (2013).

2012

- **J.H. Bin**, K. Allinger, W. Assmann, G. Dollinger, G. A. Drexler, A. A. Friedl, D. Habs, P. Hilz, R. Hoerlein, N. Humble, S. Karsch, K. Khrennikov, D. Kiefer, F. Krausz, W. Ma, D. Michalski, M. Molls, S. Raith, S. Reinhardt, B. Röper, T. E. Schmid, T. Tajima, J. Wenz, O. Zlobinskaya, J. Schreiber, and J. J. Wilkens, A laser-driven nanosecond proton source for radiobiological studies. *Appl. Phys. Lett.*, 101(24):243701 (2012).

2011

- P. G. Thirolf, D. Habs, M. Gross, K. Allinger, **J.H. Bin**, A. Henig, D. Kiefer, W. Ma, J. Schreiber, Laser particle acceleration: status and perspectives for nuclear physics. *Acta Physica Polonica B*, 42:843 (2011).

- D. Habs, P. G. Thirolf, M. Gross, K. Allinger, **J.H. Bin**, A. Henig, D. Kiefer, W. Ma, J. Schreiber, Introducing the fissionÐfusion reaction process: using a laser-accelerated th beam to produce neutron-rich nuclei towards the N = 126 waiting point of the r-process. *Appl. Phys. B*, 103:471-484 (2011).

2010

- L. G. Huang, A. L. Lei, **J. H. Bin**, Y. Bai, W. Yu, M. Y. Yu, T. E. Cowan, Improving proton acceleration with circularly polarized intense laser pulse by radial confinement with heavy ions. *Physics of Plasmas*, 17(1):013106 (2010).

2009

- **J. H. Bin**, A. L. Lei, L. H. Cao, X. Q. Yang, L. G. Huang, M. Y. Yu, and W. Yu, Influence of the target front-surface curvature on proton acceleration in laser-foil interaction. *Physics of Plasmas*, 16(4):043109 (2009).

- **J. H. Bin**, A.L. Lei, X.Q. Yang, L.G. Huang, M.Y. Yu, W. Yu, and K.A. Tanaka, Quasi-monoenergetic proton beam generation from a double-layer solid target using an intense circularly polarized laser. *Laser and Particle Beams*, 27(3):485-490 (2009).

- **J. H. Bin**, A.L. Lei, and W. Yu, Influence of initial plasma temperature on energetic proton generation from laser-plasma interaction. *Chinese Journal of Lasers*, 36(6):1416-1419 (2009).

Conference proceedings

2013

- N. Humble, K. Allinger, **J.H. Bin**, G. A. Drexler, A. Friedl, P. Hilz, D. Kiefer, W. Ma, S. Reinhardt, T. E. Schmid, O. Zlobinskaya, J. Schreiber, and J. J. Wilkens, Single shot cell irradiations with laser-driven protons. *AIP Conference Proceedings*, 1546:84 (2013).

- **J. H. Bin**, W. J. Ma, K. Allinger, H. Y. Wang, D. Kiefer, S. Reinhardt, P. Hilz, K. Khrennikov, S. Karsch, X. Q. Yan, F. Krausz, T. Tajima, D. Habs, and J. Schreiber, Divergence of laser-driven ion beams from nanometer thick foils. *Proc. SPIE 8779*, 87791H (2013).

2012

- T. Schmid, K. Allinger, **J.H. Bin**, G. Dollinger, G. Drexler, N. Humble, S. Reinhardt, O. Zlobinskaya, J. Schreiber, J.J. Wilkens, Relative biological effectiveness of single-shot irradiation with laser-driven nanosecond proton bunches. *International Journal of Radiation Oncology Biology Physics*, 84:S684 (2012).

2011

- P. G. Thirolf, D. Habs, M. Gross, K. Allinger, **J.H. Bin**, A. Henig, D. Kiefer, W. Ma, J. Schreiber, Fission-Fusion: A new reaction mechanism for nuclear astrophysics based on laser-ion acceleration. *AIP Conference Proceedings*, 1377:88 (2011).

- P. G. Thirolf, D. Habs, M. Gross, K. Allinger, **J.H. Bin**, A. Henig, D. Kiefer, W. Ma, J. Schreiber, Laser ion acceleration: status and perspectives for fusion. *EPJ Web of Conferences*, 17:11001 (2011).

2010

- D. Habs, D. Kiefer, A. Henig, R. Hoerlein, J. Schreiber, K. Allinger, **J.H. Bin**, P. G. Thirolf, C. Lang, T. Yamazaki and K. Homma, Proposed studies of radiation damping in laser interaction with an ultra-thin, coherently reflecting electron sheet, regarded as a macro-particle. *AIP Conference Proceedings*, 1228:287 (2010).

Acknowledgements

At this point, I would like to take the opportunity to thank all my colleagues, collaborators and all my friends that supported me during my PhD time and helped me to successfully complete this thesis.

First of all, I would like to thank my supervisor **Prof. Dr. Jörg Schreiber** for giving me the opportunity be part of his group and guiding me into this interesting field of laser driven ion acceleration. I am indebted to him for countless hours of fruitful discussions and ideas. I also want to thank him for his encouragement and patience on me, giving me as much freedom as I wanted and always supporting me in every possible way. He is a great supervisor.

Equally, I would like to express my thanks to **Prof. Dr. Dietrich Habs** for giving me the opportunity to work in this outstanding environment. I admire his enthusiasm and visionary thoughts.

I would like to thank **Prof. Dr. Matt Zepf** for agreeing to be my second referee of my PhD thesis. Discussion with him and his support helped me a lot. I am very honored to have him on my committee.

I would like to thank **Prof. Dr. Jürgen Meyer-ter-Vehn** for inviting me to the Astra Gemini experiment and his interest into my work.

I owe gratitude to **Prof. Dr. Ferenc Krausz** for giving me the opportunity to work in his excellent group in MPQ. I also want to thank **Prof. Dr. Manuel Hegelich** for inviting me to this group at the beginning. I am greatly indebted to **Prof. Dr. Toshiba Tajima** for sharing many brilliant ideas with me, a young student.

I want to thank **Prof. Dr. Katia Parodi**, **Prof. Dr. Otmar Biebel**, **Prof. Dr. Hartmut Ruhl**, **Prof. Dr. Stefan Karsch**, and **Prof. Dr. Jochen Weller**, who were kindly willing to be in my defense committee.

Special thanks go to all my colleagues. I am very grateful to **Dr. Andreas Henig**, **Dr. Rainer Hörlein** and **Dr. Daniel Kiefer** who introduced me to the exciting experimental world at the beginning. **Klaus Allinger** and I spent many long hours in the lab to perform the ion acceleration experiments in MPQ. I would like to thank him for the

Curriculum Vitae

Personal Data

Name:	Jianhui Bin
Date of birth:	21.01.1984
Place of birth:	Hunan
Citizenship:	Chinese

Contact Information

Address:	Am Coulombwall 1
	85748 Garching b. München
	Germany
Phone:	+49(0)89 289 54024
E-mail:	Jianhui.Bin@physik.uni-muenchen.de

Education

12/2009– present	**Max-Planck-Institut für Quantenoptik and Ludwig–Maximilians–Universität München, Germany** PhD candidate Dissertation: "Laser-Driven Ion Acceleration From Carbon Nano-Targets with Ti:Sa Laser Systems" Supervisors: Prof. Jörg Schreiber and Prof. Dietrich Habs

09/2006–07/2009	**State Key Laboratory of High Field Laser Physics, Shanghai Institute of Optics and Fine Mechanics, China**
	Master of Engineering in Optical Engineering
	Thesis: "Energetic ion generation in relativistic laser-plasma interaction"
	Supervisor: Prof. Anle Lei
09/2002–07/2006	**Tianjin University, China**
	Bachelor of Engineering in Electronic Science and Technology (for optoelectronic technology)